INTERSTELLAR MATTER

EVOLUTION OF VERY SMALL DUST PARTICLES IN MOLECULAR CLOUD OBSERVED WITH ISOCAM

Alain Abergel[1], Jean Philippe Bernard[2], François Boulanger[1], Anthony Jones[1], Marc-Antoine Miville-Deschênes[1], Laurent Verstraete[1]

[1] Institut d'Astrophysique Spatiale, Université Paris-Sud, Bât. 121, 91405 Orsay Cedex, France
[2] Centre d'Etude Spatiale des Rayonnements, Toulouse, France

ABSTRACT

In the mid-infrared, the sensitivity of ISO is such that observations of interstellar regions with limited excitation have been performed. The observed emission is due to very small particles (< 10 nm) transiently heated each time they absorb a UV photon. The exact nature of these particles and of their evolution in the life cycle of the interstellar matter still need to be elucidated. The ISO archive, containing both broad-band images and spectra at high and low spectral resolution, is a unique tool to achieve this goal. We present an analysis which combines high angular resolution specctro-imaging observations of ISOCAM with high spectral resolution data of the SWS. Systematic evolution of the very small particles are found at the illuminated edges of molecular clouds.

Key words: ISOCAM, SWS, Molecular clouds, Dust, PAHs

1. INTRODUCTION

In the mid-infrared, the ISO archive contains both broad-band images and spectra at high and low spectral resolution. This combination has provided observations of the interstellar medium (ISM) spanning an incredibly high dynamic of physical conditions ($G_0 = 1$–10^6, where G_0 is the average UV interstellar radiation field, Habing 1968).

The sensitivity of ISOCAM is such that spectro-imaging observations have been conducted in regions where the radiation field is limited ($G_0 = 1$–10^3). The observed emission (~ 5–$18\ \mu$m) is due to very small particles (< 10 nm) transiently heated each time they absorb a UV photon. Moreover, the angular resolution allows detailed analyses of the surfaces of nearby molecular clouds, where the physical conditions (excitation and density) can change drastically on small angular scales (a few arcsecs for nearby objects). We present a selection of spectro-imaging ISOCAM observations which, analysed in relation with SWS spectra at high resolution, show a systematic evolution of the very small particles at the illuminated surfaces of molecular clouds.

2. BROAD-BAND OBSERVATIONS

On Figs 1 and 2 are presented some illustrative maps of the two reflection nebulae NGC 2023 and NGC 2068 from ISOCAM observations taken with the $5 - 8.5\ \mu$m and $12 - 18\ \mu$m filters (LW2 and LW3, respectively). These two nebulae are located in the Orion B complex (distance ~ 400 pc) and illuminated by the B 1.5V star HD 37903 and the HD 38563-A and HD 38563-B pair of stars (B2 III), respectively. These stars have formed low density cavities of photo-dissociated matter inside or at the edge of dense molecular material. At a distance of $1'$ from these stars (typical distance between the stars and the illuminated surfaces of the molecular material), G_0 is around 10^3.

Striking variations of the infrared colour are visible on Figs. 1 and 2. The $5-8.5\ \mu$m$/12-18\ \mu$m ratio is around 2 near the illuminating stars, for lines of sight crossing the low density regions. This ratio sharply drops around 1 at the edge of the bright nebulae, at a position which is believed to coincide to the illuminated surface of dense molecular material (Abergel et al. 2002). The emission decreases in the molecular region because the intensity of the incident radiation decreases due to the extinction. The same tendency is observed for most of illuminated surfaces (by B or O stars and with $G_0 \sim 10^3$) of nearby dense structures observed with ISOCAM. On Fig. 3 is presented a selection of brightness profiles across different illuminated interfaces (we have included NGC 2071, also in Orion B, and the western edge of the main complex of ρ Ophiuchi, illuminated by the B5 star HD 290861 and the B2V star HD147889, respectively).

3. SPECTROCOSPIC INTERPRETATION

On Fig. 4 is presented examples of spectra taken with the CVF of ISOCAM ($\lambda/\Delta\lambda \sim 40$) in the northern part of NGC 2023 for two selected pixels with low and high values of the $5 - 8.5\ \mu$m$/12-18\ \mu$m ratio (0.6 and 1.7, respectively). The emission spectrum is dominated by the broad bands (width $\sim$0.2-0.4 μm) at 6.2, 7.7, 8.6, 11.3 and 12.7 μm detected almost everywhere in the ISM (e.g. Boulanger et al. 1998a, Mattila et al. 1996, Uchida et al. 2000, Chan et al. 2001, Hony et al. 2001, Peeters et al. 2002). These bands are centered at wavelengths characteristic of C-C and C-H bonds in aromatic hydrocarbons, and are generally dubbed as Aromatic Infrared Bands (AIBs). On the spectra of Fig. 4 (and many others in the ISO database), the AIBs appear on top of a continuum increasing towards long wavelengths.

The spatial variations of the $5 - 8.5\ \mu$m$/12 - 18\ \mu$m ratio are strongly correlated to variations of the intensity of the aromatic features (especially at $7.7\ \mu$m) relative to the continuum emission (see Abergel et al. 2002 for a detailed analysis of the

Proceedings of the Symposium *"Exploiting the ISO Data Archive - Infrared Astronomy in the Internet Age"*, 24–27 June 2002, Sigüenza, Spain (C. Gry, S. B. Peschke, J. Matagne et al. eds., ESA SP-511)

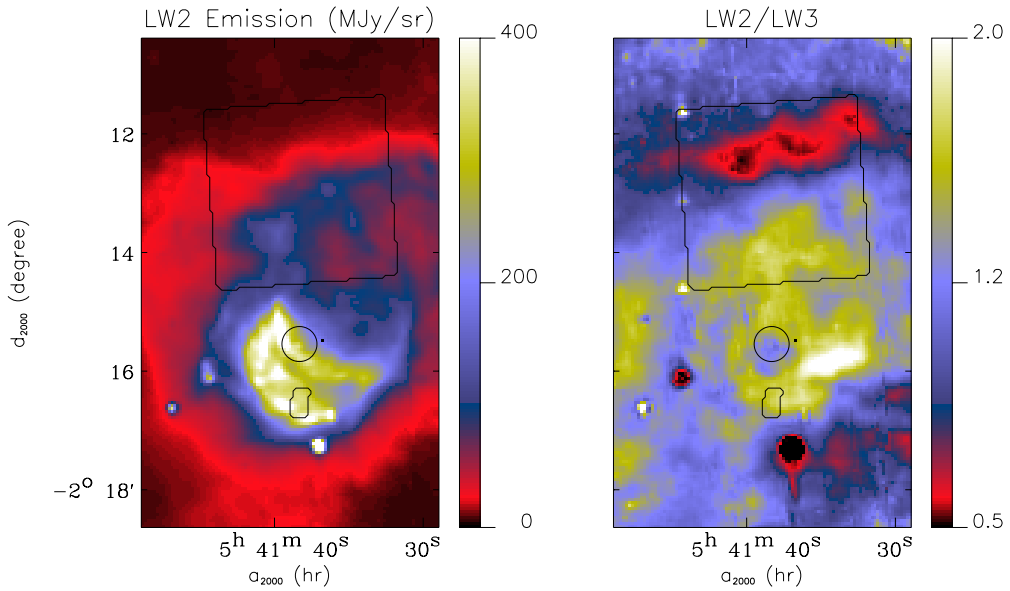

Figure 1. Left : ISOCAM map around NGC 2023 (Abergel et al. 2002) in the $5-8.5\ \mu m$ *filter (LW2). Right: Map of the* $5-8.5\ \mu m$ */* $12-18\ \mu m$ *ratio. The circle is centered at the position of the B 1.5V illuminating star HD 37903. The square and the rectangle show the field covered by the CVF observations and the slit of the SWS observation presented in Fig. 5(Verstraete et al. 2001), respectively.*

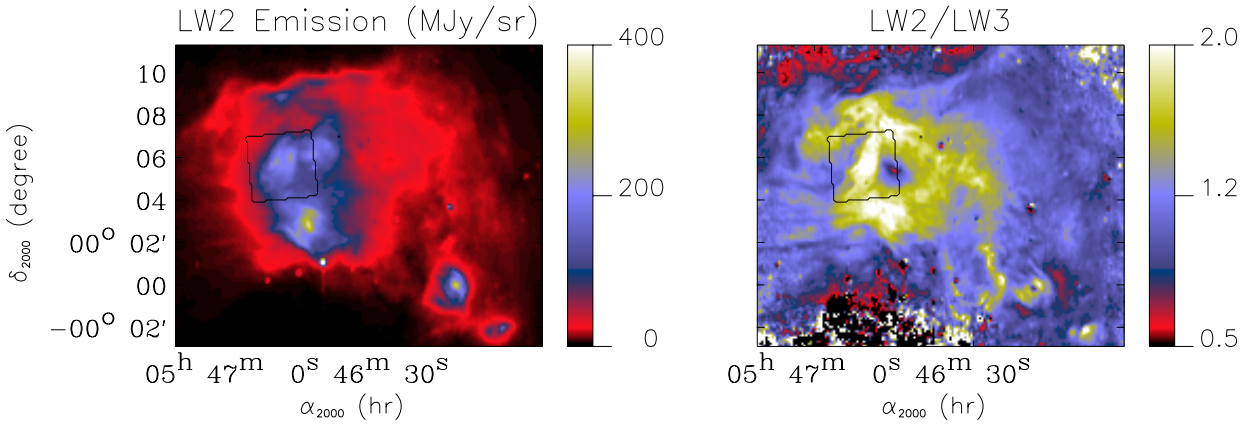

Figure 2. The same as Fig. 1 for NGC 2068.

emission spectrum within the broad-band filters). We have obtained the same conclusion for other CVF observations at the edge of reflection nebulae (Abergel et al., in prep.). The contribution of the continuum relative to the AIBs appears systematically higher at the illuminated surfaces of dense structures than in the lower density regions facing these dense strctures.

However the spectral resolution of the CVF is limited, so the spectroscopic decomposition of the spectra is not unique, which can lead to different spectroscopic interpretations. The SWS spectra have been obtained only for excited objects ($G_0 \sim 10^3 - 10^6$), but their high spectral resolution ($\lambda/\Delta\lambda = 200 - 2000$) allows detailed analyses of the shape of the AIBs and of the underlying continuum (e.g. Verstraete et al. 2001, Hony et al. 2001, Peeters et al. 2002). These data can be used to define spectroscopic templates for "optimal" adjustments of the CVF spectra.

Peeters et al. (2002) have classified the SWS spectra of a lot of sources based on the variations of the 6.2, 7.7 and 8.6 μm bands. Following Boulanger et al. (1998b), the bands are decomposed into Lorentzian profiles. The 6.2 μm band is asymmetric (two Lorentzians) and shifts from ∼6.2 to ∼6.3 μm. The 7.7 μm complex is made at least of two main sub-bands peaking at ∼7.6 μm and ∼7.8 μm, respectively. The relative intensity of these two sub-bands strongly vary. The 8.6 μm band is symmetric, and for some sources can be slightly shifted at longer wavelengths. The classes derived from these features are linked with each other, and the observed spectra depend on the type of objects. A comparable analysis has been performed by Hony et al. (2001) at longer wavelengths. The 11.3 and 12.7 μm

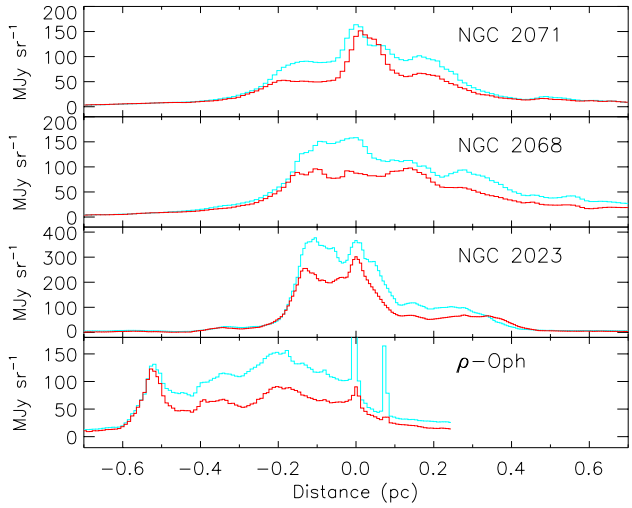

Figure 3. Brightness profiles (5-8.5 μm: Blue line, 12-18 μm: Red line) across NGC 2071, NGC 2068, NGC 2023 and the edge of ρ Ophiuchi. The illuminating stars are at the position 0 pc. The $5-8.5\ \mu m\ /\ 12-18\ \mu m$ ratio is $\sim 1.5-2$ near the central star, and sharply decreases around 1 at the edge of the bright nebulae.

bands are asymmetric (two Lorentzians). The relative intensity 11.3/12.7 strongly decreases from evolved stars to H $_{II}$ regions, but it seems that the global shape and the peak position does not present any significant tendency. The SWS spectra also contain several weaker bands, and also very broad features (width $\sim$0.5-1 μm) centered at $\sim$7 and $\sim$10 μm together with a continuum increasing towards long wavelengths.

On Fig. 5 we present a typical SWS spectrum (from Verstraete et al. 2001). For its decomposition, we have used Lorentzian profiles for the AIBs and the very broad bands, and Gaussian profiles for the rotational lines of H_2. The lower panel of the figure shows the SWS spectrum convolved by the CVF spectral response. We see that the sub-bands contained within the 7.7 and 11.3 μm bands cannot be analysed with the same details in the convolved and the full resolution spectra. However, the 7.6 μm and 7.8 μm sub-bands can be measured on the convolved spectrum once their central position is fixed (see the adjusted profile on the bottom panel of Fig. 5). Moreover, the amplitude of the adjusted continuum is slightly higher in the convolved spectrum than in the full resolution spectrum, due to a decrease of the adjusted amplitudes of the broad bands. An example of fits to the CVF spectra using the spectral template of the SWS spectrum convolved by the CVF spectral response is presented in Fig 4.

4. INTERPRETATION AND CONCLUSION

The SWS spectrum of Fig. 5 and the CVF spectrum in the lower panel of Fig. 4 correspond to lines of sight with comparable infrared colours (Fig. 1). We see that, after convolution of the SWS spectrum with the CVF spectral response (lower panel of Fig. 5), the shapes of the SWS and CVF spectra are almost identical. Such comparison strongly validates the flux calibration and the data processing pipelines of both instruments.

The adjusted spectra of Fig. 4 show that the increase of the intensity of the continuum emission relative to the intensity of the AIBs (especially at 7.7 μm) is correlated to a strong increase of the ratio of the two sub-band intensities 7.8 /7.6 (factor $\sim 2-5$). Comparable results are found for other illuminated interfaces observed with the CVF of ISOCAM (Abergel et al., in prep.). Other tendencies are also systematically observed in the CVF spectra with lower amplitudes, such as variations of the width of the 6.2 μm band, and of the intensity of the 8.6 μm band.

Peeters et al. 2002 uses the ratio 7.8 / 7.6 to define two main classes of objects. Class A$'$ (low ratio: the 7.7 μm is dominated by the 7.6 μm sub-band) corresponds essentially to H $_{II}$ regions, reflection nebulae, Post–AGBs, Herbig AeBe stars embedded in their molecular cloud and extragalactic sources, and class B$'$ (high ratio: the 7.7 μm is dominated by the 7.8 μm sub-band) to Planetary Nebulae, Post-AGBs and isolated Herbig AeBe stars.

The CVF spectra show that, for lines of sight crossing low density regions facing the illuminated surfaces of molecular clouds, the intensity of the continuum relative to the intensity of the AIBs is low, and the 7.7 μm complex is dominated by the 7.6 μm sub-band. For lines of sight crossing the illuminated surfaces of molecular clouds, the intensity of the continuum relative to the intensity of the AIBs is high, and the 7.7 μm complex is dominated by the 7.8 μm sub-band. Therefore we propose that the variations of the 7.8 / 7.6 ratio, at the origin of the A$'$ and B$'$ classes of Peeters et al. 2002, are due to density variations.

The variations of the spectra are likely due to evolution of the very small emitting particles from shielded molecular material to photo-dissociated and photo-ionised matter, or abundance variations (detailed discussion in Abergel et al. 2002). The main difficulty in reaching any definitive conclusion is that the exact nature of these very small particles is still unknown. As discussed by Peeters et al. (2002), the 7.6 μm sub-band can be actually explained by PAHs, but not the 7.8 μm one. Jones & d'Hendecourt (2000) have recently suggested that nanodiamonds could be the carriers of the AIBs. It is interesting to note that type IaA bulk diamonds, which contain nitrogen impurities, always present a strong band at 7.8 μm (e.g. Davies 1977). The continuum, which appears correlated to the 7.8 μm band, could be due to the bulk properties observed in particles which are on average larger than the particles responsible for the aromatic emission bands. The exact nature of these particles still needs to be elucidated. The ISO archive (combined with laboratory spectroscopic measurements) is a unique tool to achieve this goal.

ACKNOWLEDGEMENTS

We thank Christine Joblin and Pierre Boissel for many fruitful discussions, and the whole ISOCAM consortium for the works performed during this last decade.

REFERENCES

Abergel A., et al, 2002, A&A 389, 239

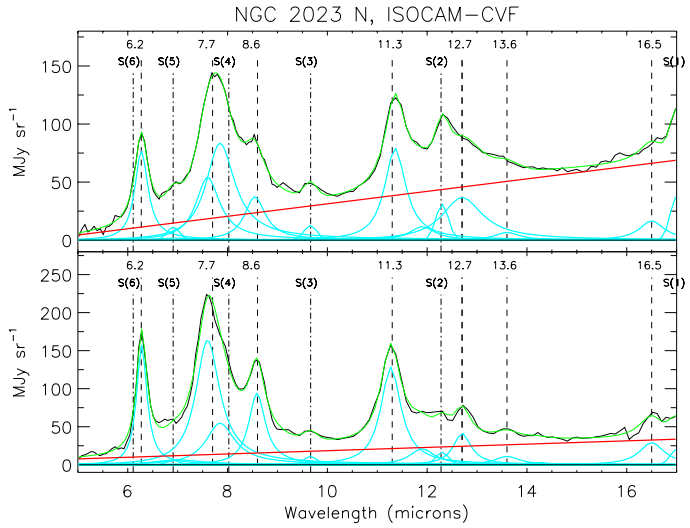

Figure 4. Some illustrative CVF spectra in NGC 2023 (from Abergel et al. 2002), for pixels with $5-8.5\ \mu m\ /\ 12-18\ \mu m$ *= 0.6 and 1.7 (upper and lower panels, respectively).*

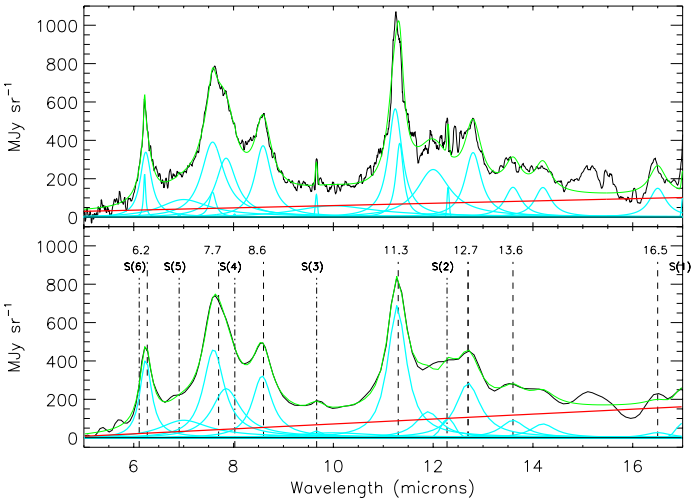

Figure 5. Upper Panel: SWS spectrum of NGC 2023 (from Verstraete et al. 2001). Lower panel: The same convolved by the spectral response of the CVF.

Boulanger F., et al., 1998a, in Star Formation with ISO, eds. J. L. Yun and R. Liseau, ASP, San Francisco, p. 15
Boulanger F., et al, 1998b, A&A 339, 194
Chan K.-W., et al., 2001, ApJ 546, 273
Davies G., 1977, in: Chemistry and Physics of Carbon, Marcel Dekker Inc., New York 13, p. 1
Habing H.J., 1968, Bull. Astr. Netherlands, 19, 421
Hony S., et al., 2001, A&A 370, 1030
Jones A., & d'Hendecourt L., 2000, A&A 335, 1191
Mattila K., et al., 1996, A&A, 315, L353
Peeters E., et al., 2002, A&A 390, 1089
Uchida K.I., et al. 2000, ApJ 530, 817
Verstraete L., et al., 2001, A&A 372, 981

USING ISOCAM DATA TO STUDY DIFFUSE INTERSTELLAR DUST EMISSION.

Marc-Antoine Miville-Deschênes[1], François Boulanger[2], Gilles Joncas[3], and Edith Falgarone[4]

[1]Canadian Institute for Theoretical Astrophysics (CITA), Toronto, Canada
[2]Institut d'Astrophysique Spatial (IAS), Orsay, France
[3]Département de Physique, Université Laval, Québec, Canada
[4]Laboratoire de radioastronomie - LERMA, Ecole Normale Supérieure, Paris, France

ABSTRACT

ISOCAM brought striking images of star forming regions but, thanks to its high sensitivity, it also allowed the observation of diffuse interstellar regions. Such observations allow the study of the life cycle of dust even in the diffuse ISM, and particularly through the transition from atomic to molecular gas. In this contribution we report on spectacular variations of small dust grains abundance in cirrus-like clouds observed with ISOCAM. In the four regions observed, we note a systematic disappearance of the small dust grains in regions where CO emission starts to appear. We suggest that the variations of the small dust grain abundance are related to the amplitude of the gas turbulent motions that modify the dust size distribution through grain-grain collisions. These observations raise interesting questions about the thermal and chemical balance of the gas in the first steps of the molecular gas formation in the diffuse interstellar medium.

Key words: interstellar medium; infrared cirrus; dust; turbulence

1. INTRODUCTION

We know that interstellar dust plays an important role in the physics of the interstellar medium. For instance, dust grains heat the gas via the photo-electric effect and provide the surfaces necessary to the formation of H_2. These processes are sensitive to the size distribution, the structure and composition of dust grains and, especially, to the abundance of the smallest particles. The IRAS images of nearby molecular complexes and bright cirrus clouds ($A_V > 1$) have revealed remarkably that the abundance ratio between small and large dust grains widely vary from cloud to cloud and within clouds. The gain in brightness sensitivity and angular resolution provided since then by dedicated observations carried out with ISOCAM, the camera on board the Infrared Space Observatory (ISO), now allows us to carry on these IRAS investigations and in particular to extend them to the range of column densities ($N_{\rm H} \sim 5 \times 10^{20}$ cm^{-2}) where the transition from atomic to molecular gas takes place.

ISOCAM has provided mostly images plus some low resolution spectra ($\lambda/\Delta\lambda \sim 50$) of the mid-IR interstellar emission over a wide range of environments including the diffuse Galactic emission and cirrus clouds. Fig. 1 resumes all the fields that were observed by ISOCAM. The yellow symbols in this figure represent the ISOGAL project fields. ISOCAM has shown that the emission in the 3-15 μm range is invariably associated with emission bands considered to be characteristic of aromatic hydrocarbon particles. To be heated to temperatures of a few 100 K by single stellar photons these particles have to be smaller than a few thousands carbon atoms. The exact nature, structure and origin of the emitting particles are still a matter of debate. The abundance variations revealed by IRAS images show that small dust grains in interstellar space do not come from evolved stars but are rather produced within the interstellar medium possibly as a result of grain shattering in grain-grain collisions. It is the motivation of this work to shed further light on the evolution of small dust grains within the diffuse interstellar medium in relation to gas physical conditions.

2. URSA MAJOR

In this contribution we present mid-IR imaging observations of four high Galactic latitude cirrus obtained with the ISO camera ISOCAM at 6" angular resolution. The observations were done with two filters LW2 (5-8.5 μm) and LW3 (12-18 μm), that measure respectively the aromatic carbon bands and the underlying continuum emission from small dust particles. The comparison of these observations with 21 cm, CO and IRAS data allows us to measure the mid-IR emissivity per hydrogen which, in such clouds transparent to stellar light, is related to the abundance and the optical properties of small dust particles independently of any modeling of the penetration of the dust heating radiation. Here we report that the mid-infrared emissivity from CO emitting regions appears systematically lower that its value for HI gas. These observations are in accordance with a depletion of small dust grains associated with the early stages of molecules formation. As most of the reactive surface available for chemistry reactions and photo-electric heating are on small grains, the disappearance of small grains could play an important role in the chemical and thermal evolution of interstellar gas.

The first diffuse interstellar region we have studied was the Ursa Major cirrus. Here we present the main results of this analysis; the details being described in Miville-Deschênes et al. (2002). We have observed three 0.05 square degree fields in the Ursa Major Galactic cirrus with ISOCAM in the LW2 and LW3 filters. These observations of a weakly illuminated and

Proceedings of the Symposium *"Exploiting the ISO Data Archive - Infrared Astronomy in the Internet Age"*, 24–27 June 2002, Sigüenza, Spain (C. Gry, S. B. Peschke, J. Matagne et al. eds., ESA SP-511)

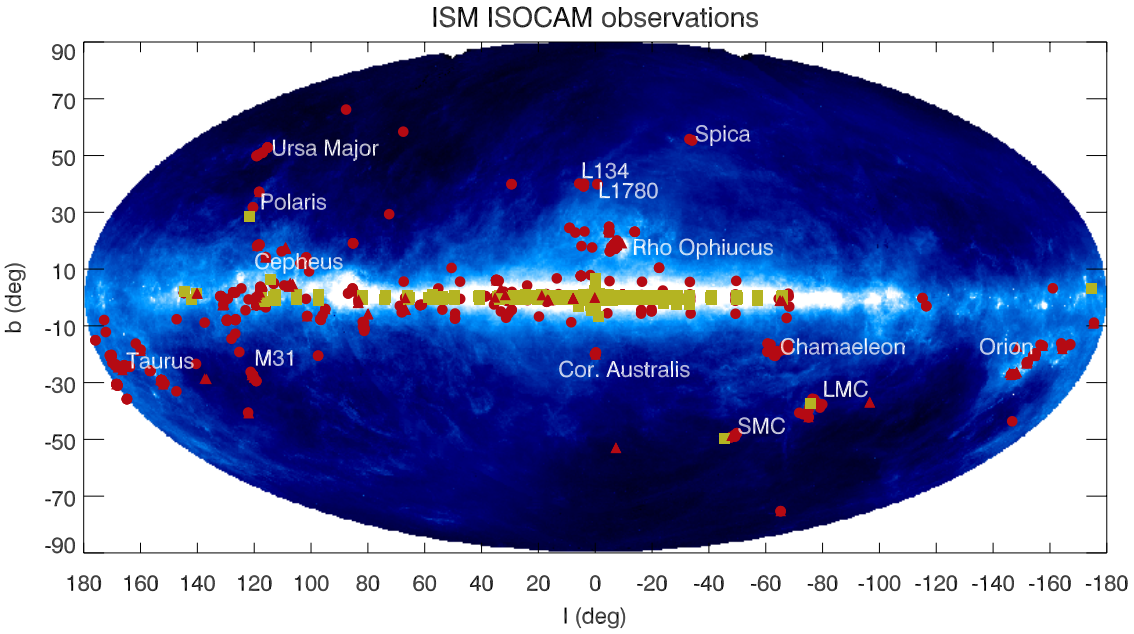

Figure 1. All-sky representation of the Interstellar Medium related observations made by ISOCAM. Star forming regions were extensively mapped by ISOCAM but, with its sensitivity more than 10 times better than IRAS, ISOCAM was also well suited to study the emission of small dust grains in diffuse cirrus clouds.

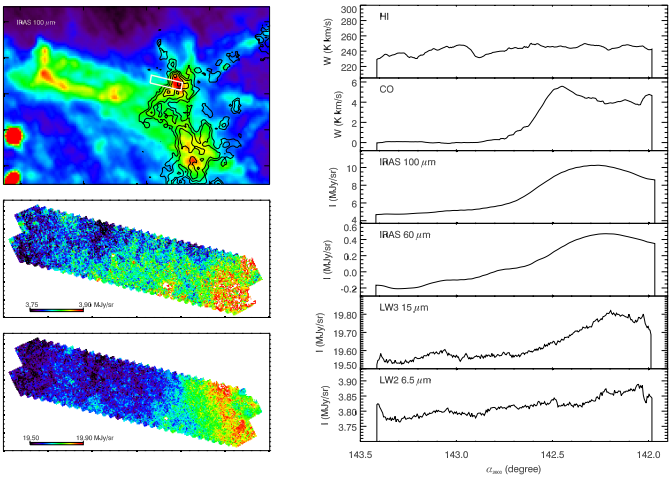

Figure 2. **Left:** *IRAS 100 μm (top) emission of the Ursa Major cirrus (contours are the ^{13}CO integrated emission of Pound & Goodman (1997)) and 6.5 (middle) and 15.0 (bottom) μm ISOCAM observations of the HI-H_2 interface.* **Right:** *Average emission of various tracers as a function of right ascension through the HI-H_2 interface. The mid-infrared emission through the interface is significantly flatter than the 100 μm emission indicating a decrease of the small dust grain abundance with respect to the big grains by a factor 3 in the molecular region.*

diffuse atomic cloud revealed striking variations of the properties of small dust particles, responsible for the emission in the 4-18 μm range. We interpret these variations as changes in their abundance, size distribution and/or optical properties. First, the combination of ISOCAM images and 21 cm interferometric data allows us to highlight a rotating filament with a small dust particles abundance ~ 5 times higher than its surroundings. Second, an unexpected variation of the mid-infrared color was found, at an interface between a fully atomic region and a denser part of the cloud where molecular hydrogen is formed and survives (see Fig 2). This color variation suggests that the amplitude of the continuum near 15 μm relative to the aromatic bands rises inside the molecular regions. This may be the result of a modification of the dust size distribution or of the structure of the emitting particles. The comparison of the ISOCAM observations with the IRAS data suggests a spectacular decrease of the small dust grain abundance in the CO region, suggestive of grain coagulation.

We consider these observations as a manifestation of interstellar turbulence impact on the dust size distribution. As dust grains are coupled to the gas motions, turbulent motions of great amplitude may produce grain-grain collision strong enough to fragment big grains and to enhance the abundance of small grains. On the other hand, when turbulent motions are of small amplitude, grain-grain collisions may lead to the disappearance of small grains through coagulation. Therefore, in the atomic part of the Ursa Major cirrus, the strong velocity gradient observed could be at the origin of grain shattering in energetic grain-grain collisions. Inversely, at the HI-H_2 interface the velocity field is less active and, in this case, the disappearance of small grains could be due to coagulation on larger grains.

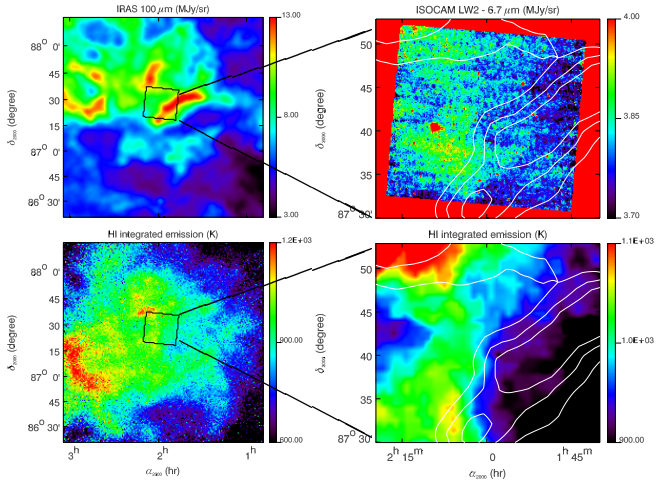

Figure 3. The Polaris flare. **Left:** *IRAS 100 μm (top) and 21 cm integrated emission (bottom) images of the Polaris cirrus cloud. The 21 cm observations were obtained at the Dominion Radio Astrophysical Observatory (DRAO) in Penticton.* **Right:** *A smaller region has been observed with ISOCAM at 6.5 μm (top). An enlargement of the same region seen at 21 cm is also shown (bottom). On these last two images, the IRAS 100 μm emission is shown as contours.*

3. NEW RESULTS ON INFRARED CIRRUS

The ISOCAM database contains several observations of high-latitude interstellar regions (see Fig. 1) that can be used to study the evolution of dust in the diffuse interstellar medium. In this section, I will present ISOCAM observations of three other diffuse clouds that confirm the presence of significant small-scale variations of the small dust grain properties, in accordance with a very fast evolution of these grains in the early stages of molecular gas formation.

3.1. POLARIS

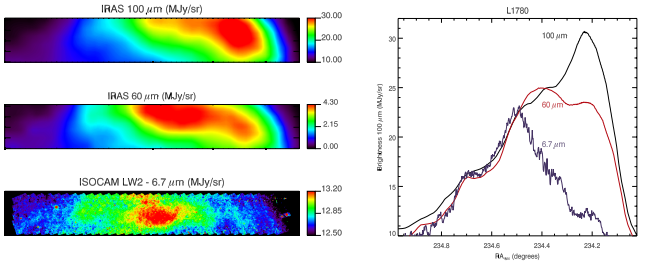

Figure 4. The L1780 cloud. **(Left:)** *IRAS 100 (top) and 60 (bottom) μm, and ISOCAM 6.5 μm (bottom) of a cut across the L1780 cloud. The 6.5 and 60 μm were multiplied by standard factors to be compared to the 100 μm emission.* **(Right:)** *Average emission of the three tracers as a function of right ascension. There is a spectacular decrease of the 6.5 / 100 μm ratio inside the L1780 filament. This is in accordance with a decrease of the smallest dust grain abundance, spatially correlated with the apparition of CO emission.*

Fig. 3 presents a region of the Polaris flare observed at 100 μm (IRAS), 21 cm (DRAO) and in the mid-infrared (ISOCAM). This region of the Polaris flare shows very different structure at IRAS 100 μm and in the 21 cm integrated emission map. In particular, the brightest filament observed at 100 μm is not seen at all at 21 cm, indicating that this diffuse filamentary structure is mainly composed of molecular gas. What is most interesting here is that this filament does not show any evidence of mid-infrared emission attributed to PAH-like particles (ISOCAM observations - see Fig. 3 top-right). In fact, in the restricted region observed with ISOCAM, there is a very clear spatial correlation between the integrated 21 cm and the mid-infrared emissions, indicating that most of the mid-infrared emission comes from the atomic gas and that the abundance of small dust grains in the molecular gas is considerably decreased.

3.2. L1780

Based on IRAS observations Laureijs et al. (1991) showed that the central part of the L1780 cloud, which has a moderate opacity ($A_v < 4$), is characterized by a low 60/100 μm ratio. This has been interpreted as the sign of a low dust temperature (T$\sim$ 15 K) and a change in the Very Small Grains (VSG) properties. The mid-infrared observations of the L1780 cloud done with ISOCAM show that the decrease of the 6.5/100 μm ratio in the central part of the filament is even more spectacular (see Fig. 4). These observations are a strong indication that the mid-infrared emitters (pah-like particles) are rapidly coagulating on bigger grains in the denser part of the cloud, where CO emission is detected. This scenario is in accordance with the hypothesis of Laureijs et al. (1991) who state that the change in the VSGs optical properties may be due to the formation of dirty-ice mantle.

3.3. TAURUS

Non star-forming regions with low 60/100 μm ratio values (often referred as **cold** infrared emission) are generally associated with CO emission. A tight correlation between these two quantities has been remarkably shown in the Taurus complex by Abergel et al. (1994). We extend this analysis with mid-infrared ISOCAM observations of a particular filament in this complex (see Fig. 5). Like in the three other regions observed in this study, the Taurus filament observed with ISOCAM has very low 6.5 μm emission associated with a low 60/100 μm and CO emission. Again, these observations are in accordance with a spectacular decrease of the abundance of the mid-infrared emitters in molecular gas. Like in the L1780 filament, the optical opacity is moderate in this Taurus filament. Extinction may contribute to the decrease of the mid-infrared emission at the center of the filament but can't account for it all.

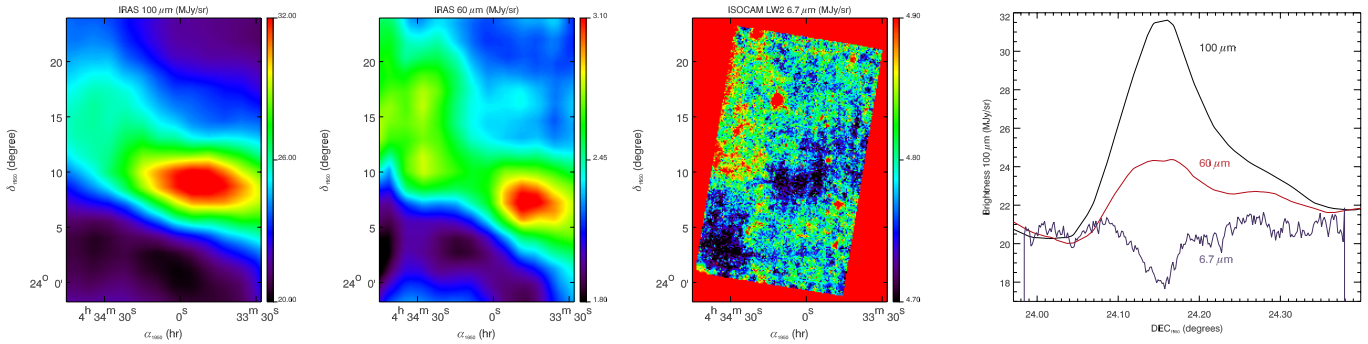

Figure 5. The Taurus filament. IRAS 100 μm, IRAS 60 μm and ISOCAM 6.5 μm observations of a filament in Taurus. On the right, we show a cut across the filament (average emission of the three tracers as a function of declination).

4. DISCUSSION

From the observations of the last two decades, two states of interstellar dust have been identified. In general, the atomic gas has fairly uniform dust properties with a constant dust size distribution and a dust temperature of ∼17.5 K. Moreover, several far-infrared and sub-mm observations have shown the presence of colder dust in molecular clouds. These observations indicate that, in such region, small dust grains are coagulating on bigger ones, creating fractal agregates with a higher emissivity which lowers the dust temperature. But intermediate steps between these two states and the exact physical processes responsible for this evolution have not been identified yet. We believe that the characterization of dust properties in low brightness regions is important to study this evolution process.

Thanks to ISOCAM's high sensitivity and to the data processing techniques that allow us to reach it (Miville-Deschênes et al., 2000) we are now able to study the properties of very small grains even in low brightness atomic and molecular gas away from heating sources. The ISOCAM observations of low brightness regions presented in this contribution show small-scale variations of the small grains properties, in accordance with a fast disappearance of the small dust grains in regions where CO starts to emit. We may see here the first step of dust coagulation that may lead to the presence of cold dust observed in more condensed regions. We suggest that the dust size distribution evolution observed here is linked to interstellar turbulence that could control the shattering, fragmentation and coagulation of grains in such environments.

The fast coagulation of small dust grains in low brightness regions raises interesting questions regarding the dust-gas relation in the interstellar medium. As most of the reactive surface for the photo-electric effect and for the formation of molecules is on small grains, the strong variations of small dust grains abundance reported in this contribution suggest significant spatial variations of the chemical and thermal balance in the diffuse ISM. In particular, the rapid disappearance of small dust grains in molecular regions raises the question of the formation rate of H_2 in such environment. In addition, if small dust grains coagulate that rapidly, we can wonder if there are any of them in condensed regions. It also raises the question of the origin of small dust grains at the surface of molecular clouds and in PDRs.

Several observations of diffuse interstellar regions are available is the ISO archive and several are still unexploited. This database can be used to study the life cycle of small dust grains in the interstellar medium. In particular, the comparison of ISOCAM data to other infrared and radio (HI, CO) observations should help to understand the link between small dust grains and the gas kinematics, thermodynamics and chemistry. Finally, the ISOCAM database is of obvious interest for the planning of future observations with SIRTF, Herschel and NGST.

REFERENCES

Abergel, A., Boulanger, F., Mizuno, A., Fukui, Y., 1994, ApJ, 423, L59

Laureijs, R. J., Clark, F. O., Prusti, T., 1991, ApJ, 372, 185

Miville-Deschênes, M.-A., Boulanger, F., Joncas, G., Falgarone, E., 2002, A&A, 381, 209

Miville-Deschênes, M.-A., Boulanger, F., Abergel, A., Bernard, J.-P., 2000, A&AS, 146, 519

Pound, M. W., Goodman, A. A., 1997, ApJ, 482, 334

MID-IR INTERSTELLAR EXTINCTION TOWARDS THE ISOGAL FIELD FC–01863+00035

Biwei W. Jiang[1], Alain Omont[2], Shashikiran Ganesh[3], Guy Simon[4], and Frédéric Schuller[2]

[1]Department of Astronomy, Beijing Normal University, P.R.China
[2]Institut d'Astrophysique de Paris, CNRS, Paris, France
[3]Physical Research Laboratory, Ahmedabad 380009, India
[4]Observatoire de Paris, Paris, France

ABSTRACT

The extinction law in the ISOCAM LW2(5.0–8.5μm, $\lambda_{\rm ref} = 6.7\mu$m) and LW3(12–18$\mu$m, $\lambda_{\rm ref} = 14.3\mu$m) bands is derived to the ISOGAL field FC–01863+00035 in the Galactic plane. Based on the ISOGAL and DENIS database, we derived the relative extinctions at 7 and 15μm are E(Ks–[7])/E(J–Ks)=0.35 and E(Ks–[15])/E(J–Ks)=0.39. The absolute extinction values in these two bands depend on the extinction values in the near-infrared adopted, e.g. $\rm A_7 = 0.031 A_V$ and $\rm A_{15} = 0.025 A_V$ with the van de Hulst-Glass near infrared extinction values. In addition, the extinction structure along this line of sight is compared with the spiral arms implied from the molecular clouds.

Key words: extinction: mid-infrared

1. INTRODUCTION

The extinction law in near-infrared has been investigated in some details. Draine (1989) described the observed extinction for $0.7< \lambda < 7\mu$m by a simple power law, $\rm A_\lambda \propto \lambda^{-1.75}$. But the exponents have been determined by different people with different results. For example, Landini et al.(1984) obtained an exponent of –1.85, which is very close to the result of Martin & Whittet (1990), –1.84. Rieke & Lebofsky (1985) found a different exponent, i.e. –1.62 which implied greater extinction at infrared wavelengths, and Rieke et al.(1989) made a slight adjustment to smaller extinction.

In the mid-infrared, the extinction law is rather controversial. Draine (1989) proposed in the 7–30μm region the extinction was dominated by the 9.7μm and 18μm silicate features, which resulted in two valleys at about 7 and 15μm in the extinction curve, with the minimum at 7μm. Hennebelle et al. (2001) obtained a consistent result on the extinction ratio between 7 and 15μm from the infrared dark clouds. Though Mathis (1990) considered also the silicate influence, he gave a higher extinction at 7μm than Draine (1989). Lutz et al.(1996) and Lutz (1999) studied the mid-infrared extinction law from the hydrogen recombination lines and found no minimum at 7μm.

ISOGAL is an ISOCAM survey at 7 and 15μm, at a spatial resolution in pixel-field-of-view of 6″ and sensitivity of about 10mJy, of about 15 deg^2, towards the Galactic plane mostly interior to $|l| < 30^\circ$ (Omont et al. 2002). About 200 fields observed are well spread in the inner bulge and in the Galactic disk. In combination with the DENIS data (Epchtein et al. 1997), the ISOGAL survey provides the potential to study the Galactic structure and extinction in highly obscured regions in the mid-infrared.

FC–01863+00035 is one of the disk fields within the ISOGAL survey with $l = -18.63^\circ \pm 0.18$ and $b = 0.35^\circ \pm 0.15$ and the filters LW2 (5.0–8.5μm, $\lambda_{\rm ref} = 6.7\mu$m) and LW3 (12–18$\mu$m, $\lambda_{\rm ref} = 14.3\mu$m). In this field more than 500 sources are extracted in the LW2 band and about 400 sources in the LW3 band. It was also observed in the DENIS survey in I, J and Ks bands by a 1-m telescope at ESO, La Silla. By cross-identifying with the DENIS catalog, 351 LW2 sources are well associated with the DENIS J and Ks sources; 198 LW3 sources are well associated with the DENIS J and Ks sources.

2. THE EXTINCTION AT 7μM AND 15μM

We derived the extinction law at 7μm and 15μm, which are approximations to (though a little bit longer than) the real reference wavelengths of LW2 and LW3 bands, based on two assumptions.

First, the ratio of interstellar reddening E(Ks-[7])/E(J–Ks) = Constant and E(Ks–[15])/E(J–Ks)=Constant, which is widely accepted. [7] and [15] decode the magnitudes in LW2 and LW3 bands calibrated to a Vega model without mass loss (Schuller et al. 2002).

Second, most of the sources in this ISOGAL field have the same intrinsic colour indexes, $\rm (J–Ks)_0$, $\rm (Ks–[7])_0$ and $\rm (Ks–[15])_0$. The analysis of the ISOGAL field in Baade's Window FC+00000+00100 has found that most of the sources in the LW2 and LW3 bands are luminous RGB stars or AGB stars. Because the objects in this field are mildly reddened by interstellar extinction, the concentration of J–Ks and Ks–[7] is very evident. For the objects with Ks–[7] < 1.0, the average $\rm (J–Ks)_0$ is 1.08 with standard deviation of 0.17 mag and the average $\rm (Ks–[7])_0$ being 0.20 with standard deviation of 0.23 mag. According to the compilation of Wainscoat et al. (1992), the value of $\rm (J-K)_0$ of an M0 giant star is about 1.0 and of an M5 early AGB star is about 1.3. So there is only a small scattering in the intrinsic colours for most of the objects in the ISOGAL stars. However, in addition to the RGB stars and AGB stars with moderate mass loss, there are some YSOs and AGB stars with high mass loss which may be important members in mid-infrared. Due to the radiation from the circumstellar shells around them, their intrinsic infrared colours are redder than

Proceedings of the Symposium *"Exploiting the ISO Data Archive - Infrared Astronomy in the Internet Age"*, 24–27 June 2002, Sigüenza, Spain (C. Gry, S. B. Peschke, J. Matagne et al. eds., ESA SP-511)

RGB stars or AGB stars with moderate mass loss. From the ISOGAL photometric results in the Baade's Window (Glass et al. 1999) and the modelling (Ojha et al. 2002), it is known that the circumstellar dust of stars with [7]–[15]>0.4 affects (Ks–[7])$_0$ and (Ks–[15])$_0$. So such stars are excluded in determining the extinction law in the 7 and 15μm bands.

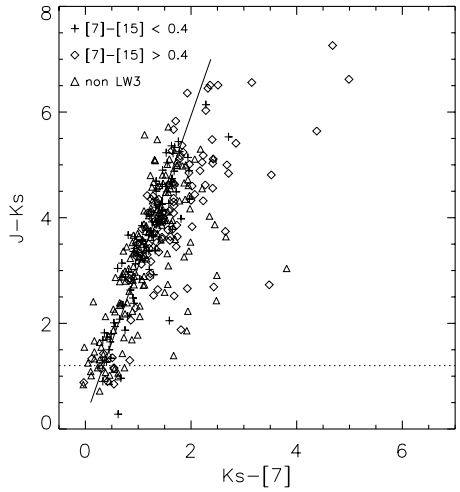

Figure 1. The J–Ks/Ks–[7] colour-colour diagram of the objects in the ISOGAL field FC–01863+00035 and the fit line to derive the extinction at 7μm. The objects with [7]–[15]>0.4 (diamonds in the figure) are excluded for the fitting, because they may be AGB stars or YSOs with thick circumstellar envelopes and have redder intrinsic colours than the major members in the field, i.e. RGB stars and AGB stars with moderate mass loss. The dot line indicates the assumed intrinsic colour (J–Ks)$_0$ = 1.2.

Provided (J–Ks)$_0$=1.2, the ratios E(Ks–[7])/E(J–Ks) and E(Ks–[15])/E(J–Ks) are derived by a robust fitting to the points in the Ks–[7]/J–Ks and Ks–[15]/Ks–[15] colour-colour diagrams shown in Figure 1 and Figure 2. The slope of the fitting line yields the relative colour excess being E(Ks–[7])/E(J–Ks)=0.35 and E(Ks–[15])/E(J–Ks)=0.39. In order to get the extinction at 7 and 15μm, we have to depend on the extinction values in the near-infrared. In Table 1, the results based on different groups of near-infrared extinction values are shown.

While the group of values from Rieke & Lebofsky (1989) are higher, the extinction values at 7μm and 15μm derived from the near-infrared extinction values preferred by Glass (1999) are just an update of those of van de Hulst(1946), and thus the two sets of values are quite close to each other, i.e. $A_7 \sim 0.030\mathrm{A}_V$ and $A_{15} \sim 0.025\mathrm{A}_V$ (cf Table 1.). The extinction ratio between the two bands is consistent with the result from Mathis (1990), which used similar extinction law in near infrared as Rieke & Lebofsky (1989), and estimated the infrared extinction from an extrapolation of the optical extinction law and near-infrared observational data, yielding $\mathrm{A}_7 \sim 0.020A_\mathrm{V}$ and $\mathrm{A}_{15} \sim 0.015A_\mathrm{V}$. The extinction values derived from the ISOGAL data is ∼0.01mag higher than those from Mathis

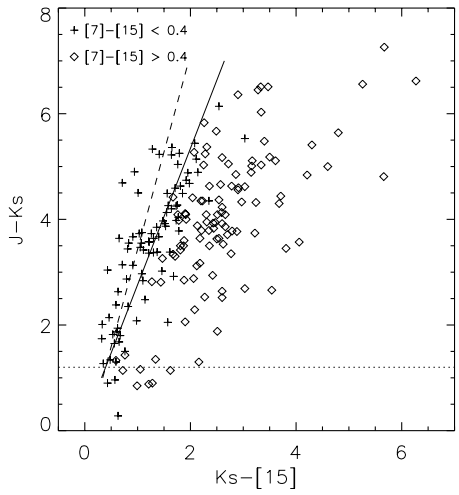

Figure 2. The J–Ks/Ks–[15] colour-colour diagram and the fit line to derive the extinction at 15μm. Again the objects with [7]–[15]>0.4 are excluded for the fitting. The result of Hennebelle et al.(2001) is drawn by a dash line, which implies higher extinction at 15μm.

(1990) in absolute values. Such a difference may arise from the uncertainty in the ISOGAL photometry or in the fitting procedure in Figure 1 and Figure 2. It is probably included as well within the uncertainty of the extrapolation by Mathis (1990); let us note that the values of Draine & Lee (1984) are similar to those of Mathis (1990) in the 7 μm range, but almost twice larger in the 15 μm range. The average on the wavelength range of the LW2 and LW3 broad bands yields also larger values than at 7 and 15μm, respectively, which are both close to a minimum of the extinction curve. This result is also consistent with the results derived by Lutz (1999) who used the hydrogen recombination lines and the near-infrared extinction law of Rieke & Lebofsky (1989) towards the Galactic centre, in that the extinction law lacks the deep minimum at 7μm, particularly if we use the same extinction values in the near-infrared as Lutz (1999). However, this result on the extinction values is not compatible with the result of Hennebelle et al. (2001) who derived the 7

Table 1. Extinction values at 7μm and 15μm based on different groups of extinction values in near-infrared. The first column used the values for J and Ks derived from van de Hulst(1946), the second column used the values for J and Ks derived from Glass(1999), and the third column used the values for J and Ks derived from Rieke & Lebofsky(1989).

Band	A_λ/A_V		
	vdH	ISG	R & L
J	0.245	0.256	0.281
Ks	0.087	0.089	0.112
7	0.032	0.031	0.053
15	0.026	0.025	0.046

to 15μm opacity ratio equal to $\sim$0.7 based on an analysis of infrared dark clouds from the ISOGAL survey. In Figure 2, the 15 μm value deduced from this ratio is shown by a dashed line derived from the extinction values at J, Ks and 7μ taken from column 2 of Table 1. It is evident that their result implies more extinction at 15μm. Let us stress that our fitting is somewhat uncertain at 15 μm because of the possibility of residual effects of circumstellar reddening on Ks–[15] especially for the distant luminous sources with large extinction. Therefore, we consider that the 15μm value deduced from Hennebelle et al. (2001) (dashed line in Figure 2) is still compatible with the data of Figure 2, and that our data cannot provide a really accurate value of the extinction at 15μm. One has to keep in mind that the extinction law may diverse with the directions due to the inhomogeneous distribution of the interstellar matter in the Galactic plane.

3. EXTINCTION STRUCTURE ALONG THE LINE OF SIGHT

The extinction to individual objects can be calculated now from their observed colour indexes J–Ks or Ks–[7] by assuming a universal intrinsic colour $(J–Ks)_0$ and $(Ks–[7])_0$. As explained in previous section, a value of 1.2 for $(J–Ks)_0$ is reasonable for the objects with [7]–[15]<1.0. In the fitting procedure to derive the extinction at 7μm and 15μm, the intrinsic colours $(Ks–[7])_0$ and $(Ks–[15])_0$ are derived under the condition that $(J–Ks)_0$=1.2. The results are $(Ks–[7])_0$=0.34 and $(Ks–[15])_0$=0.39. By making use of this group of intrinsic colours, the extinction to sources, which were detected in both J and Ks bands and with [7]–[15]<1.0 if detected in LW2 and LW3 bands, is deduced from their J–Ks; the extinction to the sources, which were not detected in J band but detected in Ks and LW2 bands and with [7]–[15]< 0.4, is deduced from their Ks–[7].

The distribution of A_V is shown in Figure 3, where values of A_V from J–Ks or Ks–[7] are distinguished by the dash or dot lines, while the summation of the two types is represented by the solid line. The structure of extinction along this line of sight is not uniform. There are a few bins of A_V where the objects are more concentrated, i.e. for A_V being about 12–24, maybe 28–32 and perhaps weak one at 0–2, and >40. The wide peak around 12–24 (indeed including a small spike between 20 and 22) is the strongest and very clear.

We think the uneven distribution of A_V reflects the inhomogeneities in the distribution of the interstellar medium and the peaks in Figure 3 may correspond to the spiral arms. In order to see if the peaks of A_V coincide with the positions of the spiral arms, we estimated the extinction values to the arms from the emission in the radio lines of CO and HI. The kinematical distance to the interstellar clouds can be inferred from their radial velocities. Through the line of sight of this field at the direction l=–18.63°and b=0.35° lie sequentially the near sides of inner spiral arms, Sagittarius ($\sim$1 kpc), Centaurus ($\sim$4 kpc) and Norma ($\sim$6 kpc), the bulge and the far side of spiral arm Norma to a distance of about 13 kpc ($R_\odot$ = 8.5kpc). Based on the CO data presented by Dame et al. (2001) and the HI data by

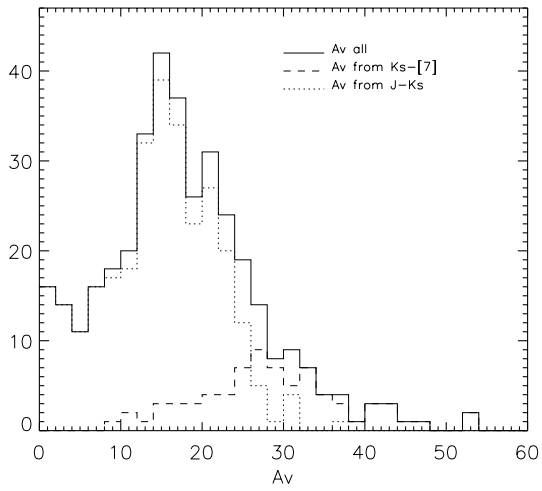

Figure 3. Distribution of the interstellar extinction A_V, which are derived either from J–Ks (dot line) or from Ks–[7] (dash line) when no data in J band are available (sources with [7]–[15] > 0.4 are excluded), and from the addition of these two types (solid line).

Bloemen et al. (1990), we estimated A_V in Table 2 by adopting the conversion factor $2.5 \times 10^{20} \mathrm{cm}^{-2} (\mathrm{K\ km\ s}^{-1})^{-1}$ from the CO brightness temperature to H_2 column density and the factor $10^{21} \mathrm{molecules\ cm}^{-2}\ \mathrm{mag}^{-1}$ from H_2 column density to A_V. This estimation, in particular of the HI column density, suffers some uncertainty from integrating the velocity or unclear contours of the paper that could be about 20%. In addition, there is an ambiguity for the CO emission at -70, -80 km/s which could be attributed either to the near side or to the far side of Norma. In Table 2, the upper part displays the A_V values deduced from the molecular lines (CO and HI) in different velocity coverage which means different distance ranges. The lower part summarises the A_V values from the molecular lines and shows the result from this work.

The comparison of the extinction of ISOGAL sources with the extinction values from CO and HI data (Table 2), shows how these sources are located with respect to the spiral arms. The first possible vague peak at $A_V = 2.0$ in Figure 3 could correspond to the first arm Sagittarius that is about 1kpc away. The big peak at 12-24 may be attributed to the near side of Centaurus, and the vague peak at 28-32 could perhaps reflect the near side of Norma. The appreciable number of stars with very large values of the extinction ($A_V \gtrsim 34$) could correspond to additional extinction beyond the near side of Norma. However, since there is little evidence for much gas there, it is more probable that they are behind patches of larger extinction within the Centaurus or near Norma arms. Similarly, stars with $A_V \sim$ 5–10 could lay, between Centaurus and near Norma, behind regions with smaller extinction than average in the Centaurus arm.

Table 2. Estimations of interstellar extinction A_V in different distance ranges

	Nearby	Centaurus	Norma	Bulge & beyond
Distance	0 – 3kpc	3 – 6kpc	6 – 8kpc	>8kpc
V_{LSR}(km/s)	>0	-0 – -60	-60 – -100	-110 – -150
H_2(via CO)	1.1	17.9	6.9	4.7
HI	0.9	3.0	3.0	2.4
		Accumulated extinction		
Distance	0 – 3kpc	0 – 6kpc	0 – 8kpc	0 – >8kpc
H_2+HI	2.0	22.9	32.8	39.9
ISOGAL	0 – 2	12 – 24	28 – 32	∼40

4. SUMMARY

The infrared law at mid-infrared wavelengths is derived based on the ISOGAL data in LW2 and LW3 bands in combination with the DENIS data in IJKs bands toward an ISOGAL field in the inner Galactic plane. The results are compared with previous investigations and there are both consistency and inconsistency. The extinction value at 7μm is $\sim 0.030 A_V$ with small uncertainty, and the extinction value at 15μm is less certain due to the influence of the circumstellar dust shells.

The extinction structure along this line of sight coincides with the concentrations of interstellar medium in the spiral arms inferred from the radio molecular lines CO and HI.

ACKNOWLEDGEMENTS

Jiang would like to express her gratitude to the LOC of the conference for supporting her local expenses, and to NKBRSF G19990754.

REFERENCES

Bloemen, J., Deul, E., Thaddeus, P. 1990, A&A 233, 437
Dame, T., Hartmann, D., Thaddeus, P. 2001, ApJ 547, 792
Draine, B.T., & Lee H. 1984, ApJ 285, 59
Drain, B.T. 1989, Proc 22nd ESLAB Symp. on IR Spectroscopy in Astron., Kaldeich B.H.(ed), ESA SP-290, p.93
Epchtein, N., De Batz, B., Capoani, L., et al. 1997, Messenger 87, 27
Glass, I. 1999, Handbook of Infrared Astronomy, Cambridge Uiversity Press
Glass, I., Ganesh, S., Alard, C., et al. 1999, MNRAS 308, 127
Hennebelle, P., Pérault, M., Teyssier D. et al. 2001, A&A 365, 598
Landini, M., Natta, A., Oliva, E., et al. 1984, A&A 134, 284
Lutz, D., Feuchtgruber, H., Genzel, R. et al. 1996, A&A 315, L269
Lutz, D. 1999, The Universe as seen by ISO, Cox P. & Kessler M. (eds), p.623
Martin, P., & Whittet, D. 1990, ApJ 357, 113
Mathis, J., 1990, ARA&A 28, 37
Ojha, D., Omont, A., Simon, G., et al. 2002, A&A, submitted
Omont, A., Ganesh, S., Alard C., et al. 1999, A&A 348, 755
Omont, A., Gilmore, G., Alard, C. et al. 2002, in preparation
Rieke, G., & Lebofsky, M. 1985, ApJ 288, 618
Rieke, G., Rieke, M., Paul A. 1989, ApJ 336, 752
Schuller, F., Ganesh, S., Messineo, M., et al. 2002, A&A, to be submitted
van de Hulst, H.C. 1946, Rech. Astron. Obs. Utrecht, 11, 1
Wainscoat, R., Cohen, M., Volk, K., et al. 1992, ApJSS 83, 146

AN ARCHIVE SURVEY OF CIRRUS STRUCTURES WITH ISOPHOT

Csaba Kiss[1,2], Péter Ábrahám[1], Ulrich Klaas[2], Dietrich Lemke[2], Philippe Héraudeau[2], and Carlos del Burgo[2]

[1] Konkoly Observatory, P.O. Box 67, H-1525 Budapest, Hungary
[2] Max-Planck-Institut für Astronomie, Königstuhl 17, D-69117, Heidelberg, Germany

ABSTRACT

ISO observations opened a new window to the studies of the infrared cirrus, providing measurements surpassing IRAS in wavelength coverage, spatial resolution, number of photometric bands and spectroscopic capabilities. Although ISO was not designed for survey mode, many large areas were investigated and imaged, especially using the ISOPHOT-C cameras. These measurements provide an excellent data base to study the physical parameters, dust composition and spatial structure of the far-infrared cirrus emission in the Galaxy under various conditions.

Key words: ISM: structure – infrared: ISM – astronomical data bases: ISO Data Archive

1. INTRODUCTION

The discovery of the infrared cirrus emission of the Galaxy was one of the major results of the IRAS mission (Low et al. 1984). Its name is due to the resemblance to the cirrus clouds in the Earth's atmosphere. This emission dominates the far-infrared sky at $\lambda \geq 60\mu$m, even at high galactic latitudes. It was soon realized that it originates mainly from dust in irregularly shaped HI clouds of the Milky Way (Boulanger & Pérault 1988). A universal colour of $I_{60}/I_{100} \approx 0.21$ was derived and via this colour a cold component of the diffuse emission $\Delta I = I_{100} - 0.21 \times I_{60}$ was separated. Measurements with the DIRBE instrument on board the COBE satellite resulted in a cirrus temperature of $T_{cirrus} \approx 17.5$ K. An even colder dust component of $T_{cold} \approx 15$ K was found from these measurements, too (Lagache et al. 1998).

IRAS observations led to the development of the three-component dust model consisting of polycyclic aromatic hydrocarbon (PAH) molecules, very small grains and big grains (Puget & Léger 1989; Désert et al. 1990).

In the last decade several authors reported on the fractal structure of the interstellar clouds, either atomic (Green 1993) or molecular (Stutzki et al. 1998), based on radio measurements. A similar investigation was carried out for the dust emission by Gautier et al. 1992 analysing the power spectrum of IRAS 100 μm scans. They found that cirrus has a similar fractal structure as that of denser molecular clouds, and they determined a universal spectral index $\alpha = -3$ of the spatial power spectrum. Based on these results, (Helou & Beichman 1990) (hereafter H&B) derived a formula for estimating the cirrus confusion noise (the uncertainty in the point source flux photometry due to the variation of the cirrus background), which was then widely used in designing far-infrared space telescope measurements.

Despite major achievements in the study of the galactic cirrus, IRAS left a handful of open issues, which could be answered by the enhanced spatial resolution and extended spectral coverage of ISO.

2. SPECTRAL FEATURES OF THE CIRRUS EMISSION

2.1. PAH FEATURES IN THE DIFFUSE CIRRUS EMISSION

The family of so-called unidentified infrared radiation bands (UIR) in the 3.3–11.3 μm wavelength range has been observed for about 30 years (Gillett et al. 1973) in a number of galactic objects, such as planetary nebulae (PN), HII regions and reflection nebulae (RN), around early type stars as well as in some external galaxies. However, their true origin has not been clarified, there is a good evidence for the carriers being some sort of carbonaceous material: polycyclic aromatic hydrocarbons (PAH), very small grains consisting of hydrogenated amorphous carbon (HAC), quenched carbonaceous composites (QCC) or coal.

Although these bands are frequently observed in galactic objects, no observations were carried out before ISO searching for the counterparts of these emission lines in the diffuse galactic background emission (DGBE) where the intensity of the interstellar radiation field (ISRF) is 100–1000 times lower.

The observations made by the ISOPHOT low-resolution spectrometer PHT-S included 50 lines of sight close to the galatic plane, and resulted in the detection of emission features at 6.2, 7.7, 8.6 and 11.3 μm with absolute intensities of $\sim$1/10 of that observed in reflection nebulae and planetary nebulae (Mattila et al. 1996). Similar intensity ratios and band widths indicate a common carrier of the UIR bands in the DGBE and in RN or PN. The absence of any detectable continuum emission at 10 μm implies, that the UIR bands do not originate from grains at equilibrium temperatures and therefore are most probably emitted by PAH molecules.

Proceedings of the Symposium *"Exploiting the ISO Data Archive - Infrared Astronomy in the Internet Age"*, 24–27 June 2002, Sigüenza, Spain (C. Gry, S. B. Peschke, J. Matagne et al. eds., ESA SP-511)

2.2. Far-infrared properties of small scale cirrus structures

IRAS detected many point-sources which were - because of their spectral nature - called "100 μm-only sources", having a clear detection only at the longest wavelength band. These sources were generally assumed to be 'cirrus-knots', i.e. low density enhancements of the diffuse background. Due to its limited wavelength coverage IRAS was not able to further unravel the nature of these sources. The first investigation of a 100μm-only source was performed by Laureijs et al. 2000, with the target PSC 21358+7020 in Cepheus. The observations were made in 9 filterbands in the 60–200 μm range using the ISOPHOT-C cameras.

This analysis showed that the spectral energy distribution (SED) of this source is very much cirrus-like for $\lambda \geq 100\,\mu$m with a dust temperature of $T_d = 16.8 \pm 0.5$ K or $T_d = 20.0 \pm 0.5$ K assuming a modified black-body SED with $\beta = 2$ and $\beta = 1$ emissivity law, respectively. A significant excess emission was observed for $\lambda < 100\,\mu$m, indicating the presence and high abundance of very small grains. ISO was also able to resolve the source PSC 21358+7020 as a cloudlet, which is a strong density enhancement in the diffuse cloud region with $n_H \geq 10^3\,cm^{-3}$. This result suggests that a fraction of the 100 μm cirrus point-source detections by IRAS could be cloudlets that are diffuse/-translucent but also moderately dense.

2.3. Far-infrared colours of dust in high latitude regions

ISOPHOT 60–200 μm observations of some high latitude clouds covering a range of dust column densities provided a well-defined relationship for the emission between 150 and 200μm. This implies that the FIR emission of large grains is a unique function of the dust column density. A region-to-region variation was found in the relative strength of the emission caused by small dust particles and big grains, indicating a variation in the abundance of small grains (del Burgo, this volume).

3. SPATIAL STRUCTURE OF THE CIRRUS EMISSION

3.1. Confusion noise in the far-infrared

Due to its fractal-like structure, the far-infrared cirrus emission contributes significantly to the uncertainty in the determination of a point-source flux, because of the variation of the sky brightness between target and reference positions, the so-called *confusion noise*. At far-infrared wavelengths the confusion noise is a very important limitation for the achievable sensitivity. Unlike in the case of e.g. the photon noise, the signal-to-noise ratio cannot be improved by longer integration times, since the confusion noise is also a signal: the signal of the background fluctuations. Based on partly theoretical considerations and the results obtained by Gautier et al. 1992, Helou & Beichman 1990 derived a formula for the confusion noise for diffraction limited telescopes:

$$\frac{N_{H\&B}}{1\,\mathrm{mJy}} = 0.3\left(\frac{\lambda}{100\,\mu\mathrm{m}}\right)^{2.5}\left(\frac{D_t}{1\,\mathrm{m}}\right)^{-2.5}\left(\frac{\langle B_\lambda\rangle}{1\,\mathrm{MJysr^{-1}}}\right)^{2.5} \quad (1)$$

where $N_{H\&B}$ is the confusion noise estimate, λ is the measurement wavelength, D_t is the diameter of the telescope primary mirror and $\langle B_\lambda\rangle$ is the average surface brightness of the field. This formula has been widely used in designing far-infrared space telescope measurements, however it has never been verified for $\lambda > 100\,\mu$m. It should be mentioned, that the formula depends on the measurement wavelength in two ways: (1) via the resolution parameter λ/D_t and (2) via the dependence of the surface brightness on λ, i.e. the SED of the emitting medium.

In order to study the spatial structure and confusion noise properties of the cirrus emission in detail, we set up a database consisting of 175 large P22 raster maps (Laureijs et al. 2002), obtained in four filter bands (90, 100, 170 and 200 μm) with the C100 and C200 cameras of ISOPHOT. The details of this study can be found in Kiss et al. 2001.

We calculated the second order structure function $S(\theta)$ for each map

$$S(\theta) = \left\langle \left| B(x) - \frac{B(x-\theta) + B(x+\theta)}{2} \right|^2 \right\rangle_x \quad (2)$$

where B is the sky brightness, x is the location of the target, θ is the separation between the target and reference sky positions, and the average is taken in spatial coordinates over the whole map. The zodiacal light contribution was removed from the maps using the COBE/DIRBE zodiacal light model, converted to the ISOPHOT filter bands Héraudeau et al. 2001. The maps were colour corrected according to a spectral energy distribution (SED) of a modified black body with ν^2 emissivity law, and a temperature of 20 K.

The noise due to sky brightness fluctuations (structure noise), N_{str}, is defined as:

$$N_{str}(\theta) = \sqrt{S(\theta)} \times \Omega \quad (3)$$

where Ω is the solid angle of the measuring aperture. The measured N_{str} is the resultant of the sky brightness fluctuations (confusion noise) and instrument noise contribution (Herbstmeier et al. 1998):

$$N_{str}^2 \leq N^2 + 2 \cdot N_{inst}^2 \quad (4)$$

where N_{str} is the measured structure noise, N is the confusion noise and N_{inst} is the instrument noise.

After a careful determination of the instrument noise (Kiss et al. 2001) confusion noise values for all the maps of the database were derived. In order to test the applicability of the H&B formula, the brightness dependence of the confusion noise was analysed for each filter individually.

Following the logic of the H&B formula, a power-law relationship between the average surface brightness of the fields and the strength of the confusion noise was assumed, but also a constant term was allowed for:

$$\frac{N(\theta_{min})}{1\,\mathrm{mJy}} = C_0 + C_1 \times \left(\frac{\langle B\rangle}{1\,\mathrm{MJysr^{-1}}}\right)^{\eta} \quad (5)$$

where C_0, C_1 and η are parameters to be determined. Fitted parameters can be found in (Kiss et al. 2001).

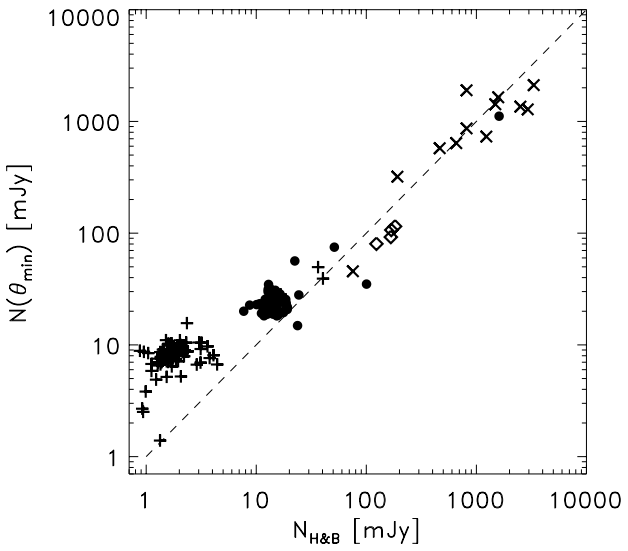

Figure 1. Confusion noise at the resolution limit $\theta_{\min}$ determined by Kiss et al. 2001 as compared to the prediction by Helou & Beichman 1990. The symbols are: plus signs: 90 μm; diamonds: 100 μm; black dots: 170 μm; crosses: 200 μm

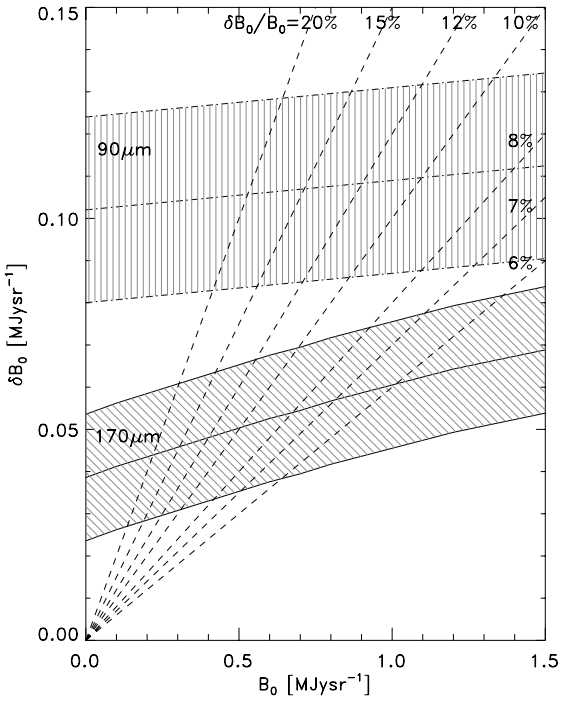

Figure 2. CFIRB fluctuation amplitudes versus the assumed absolute CFIRB level. The hatched regions represent the formal errors of the fits in Eq. 5 for 90 and 170 μm. A set of dashed lines marks $\delta B_0/B_0$ = 6, 7, 8, 10, 12, 15 and 20%.

In Fig. 1 we compare our results with the predictions of the H&B formula (Eq. 1). In the surface brightness range where the cirrus emission dominates (5–30 $\mathrm{MJysr^{-1}}$) the H&B formula predicts confusion noise values within a factor of 2 of our results. The scatter cannot be attributed to measurement uncertainties, it probably reflects the physical differences among the fields. For the brightest fields the H&B formula seems to systematically overestimate the measured confusion noise values. Such regions, however, contain molecular clouds, therefore they may have different spatial structure from a cirrus region and should be described by a different power law (see next subsection). The figure also shows a large discrepancy at low $\mathrm{N}(\theta_{\min})$ confusion noise values corresponding to low surface brightness, which could be well treated by the introduction of an offset.

The deviations in the faint range are most probably caused by fluctuations due to the Cosmic Far-Infrared Background (CFIRB). Therefore the analysis of the surface brightness dependence of the confusion noise provides a new way in detecting extragalactic background fluctuations. Our results at 90 and 170 μm fulfil the three main criteria of an extragalactic background detection (Hauser & Dwek 2001): (1) it has a well-detected positive value; (2) it cannot be attributed to any instrumental effect, to any source in the Solar System or in the Galaxy, so it is most probably of extragalactic origin; (3) it provides the same constant value for each field (within the uncertainties), indicating isotropy.

When fitting $\mathrm{C_0}$ and $\mathrm{C_1}$, the surface brightness still contains the contribution of the extragalactic background. For a correct determination of the CFIRB fluctuation amplitudes, the CFIRB absolute surface brightness must be separated. Since this value is not precisely known, especially for longer wavelengths, we did not correct for it, but rather performed a simultaneous determination of the fluctuation amplitude and the assumed absolute CFIRB level (see Fig. 2). Theoretical models (Bond et al. 1986) predict the fluctuation-to-absolute level ratio, which are 10% and 7% for the ISOPHOT 90 and 170 μm filter measurements, respectively. The resulting fluctuation amplitudes are 7 ± 2 mJy and 15 ± 4 mJy at 90 and 170 μm, respectively. We obtained a CFIRB surface brightness of $\mathrm{B_0 = 0.8\pm0.2\,MJysr^{-1}}$ ($\nu\mathrm{I}_\nu = 14\pm3\,\mathrm{nWm^{-2}sr^{-1}}$) at 170 μm and an upper limit of $1.1\,\mathrm{MJysr^{-1}}$ ($\nu\mathrm{I}_\nu = 37\,\mathrm{nWm^{-2}sr^{-1}}$) at 90 μm. These results are in very good agreement with other measurements (Lagache & Puget 2000) and with theoretical predictions (Pei et al. 1999).

3.2. Small-scale spatial structure of the galactic cirrus emission

At wavelengths beyond 90 μm the most significant component superimposed on the CFIRB is the cirrus emission. The correct determination of the CFIRB requires a precise removal of this foreground component (Guiderdoni et al. 1997).

CFIRB fluctuations are expected to show the following properties [see e.g. Hauser & Dwek 2001]: (1) the spatial distribution corresponds to a flat power spectrum, (2) they are isotropic and (3) they have a positive constant value. In contrast, the fluctuations due to galactic cirrus emission scale up with ab-

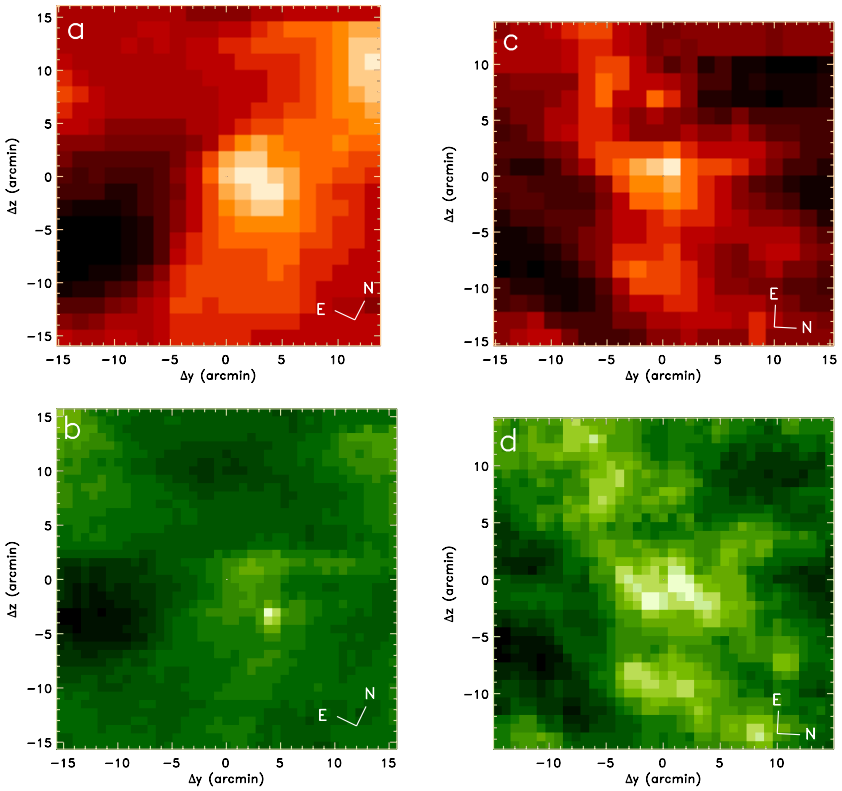

Figure 3. 100 and 200 μm range images of two sample fields in the satellite coordinate system (Laureijs et al. 2002). The orientation of the celestial coordinate system is indicated. (a) Cham–II, 200 μm (b) Cham–II, 100 μm (c) NPC 1, 200 μm (d) NPC 1, 90 μm. The central galactic coordinates of the Cham–II and NPC 1 fields are $l = 303\overset{\circ}{.}5$, $b = -14\overset{\circ}{.}2$ and $l = 121\overset{\circ}{.}6$, $b = 24\overset{\circ}{.}2$, respectively. While the FIR emission in NPC 1 arises from the same cirrus structure at both wavelengths, there seems to be an additional component of cold condensations in Cham II, as discussed in Sect. 3.2.

solute brightness (Eq. 5) and can be described by a multifractal structure, yielding a steep Fourier power spectrum. It is usually described by one main parameter, the spectral index α: $\mathrm{P} = \mathrm{P}_0 \times (\mathrm{f}/\mathrm{f}_0)^{\alpha}$, where P is the Fourier power, f is the absolute value of the two-dimensional spatial frequency and P_0 is the Fourier power at the spatial frequency f_0 (Gautier et al. 1992). Since cirrus fluctuations are different from CFIRB fluctuations in at least two features (spatial frequency– and brightness dependence), it is possible to separate them from each other in two independent ways:

(1) The decomposition by means of the brightness dependence at a fixed spatial frequency was performed by Kiss et al. 2001, and resulted in a new determination of the CFIRB fluctuation amplitudes at 90 and 170 μm, as presented in the previous subsection.

(2) The decomposition using the Fourier power spectrum was introduced by Guiderdoni et al. 1997.

For faint fields, where CFIRB fluctuations are expected to be dominant in the highest spatial frequency range, the knowledge of the cirrus spectral index is mandatory for decomposition.

Lagache & Puget 2000 derived CFIRB fluctuation amplitudes at 170 μm applying the spectral index of $\alpha \approx -3$ obtained by Gautier et al. 1992 for the cirrus decomposition.

Herbstmeier et al. 1998 analysed a few fields observed by ISOPHOT in the 90–180 μm wavelength range. They found a variation of spectral indices in the range of $-0.5 \geq \alpha \geq -3.6$, depending on wavelength, brightness and sky position. However, this sample was too small (four fields, two of them measured only at one wavelength) for general conclusions, but their results clearly indicated that the $\alpha = -3$ cirrus spectral index may not be universal.

We extended the analysis by Herbstmeier et al. 1998 and selected 20 FIR maps from the ISO archive, covering 13 separate sky regions. All maps were obtained in the PHT22 staring raster observing mode (Laureijs et al. 2002). Maps containing strong point sources or obvious spatial structures were excluded, but the selected ones had to show a clear sign of cirrus emission in the power spectrum. This requires a minimum average surface brightness of $\langle \mathrm{B} \rangle \approx 3\,\mathrm{MJysr}^{-1}$. Such fields are slightly brighter than the faintest fields in the 90–200 μm wavelength range after the subtraction of the Zodiacal Light. This investigation is described in detail in Kiss et al. 2002.

As presented in Fig. 4a, b and c, the spectral indices show a clear dependence on the average surface brightness and on the average neutral hydrogen column density of the field. The median values are $\overline{\alpha}_{C1} = -3.15 \pm 0.48$ and $\overline{\alpha}_{C2} = -3.87 \pm 1.06$ for the C100 and C200 detectors, respectively, which are not too different from the supposed universal value of $\alpha = -3$.

It was possible to extrapolate an α_{C2} value for the faintest fields of the far-infrared sky, by robust-fitting the data points of the α_{C2}–log($\langle \mathrm{B}_{C2} \rangle$) plot in Fig. 4b. This resulted in $\alpha_{C2} = -2.3 \pm 0.6$ for the faintest cirrus fields ($\langle B \rangle \approx 2\,\mathrm{MJysr}^{-1}$). Such a value reduces CFIRB fluctuations derived by means of the Fourier power decomposition by 5 to 20% in the 170-200 μm wavelength range.

In Fig. 4d we plot the ratio of the spectral indices α_{C2}/α_{C1} determined for fields with both a C200 and a C100 map. Un-

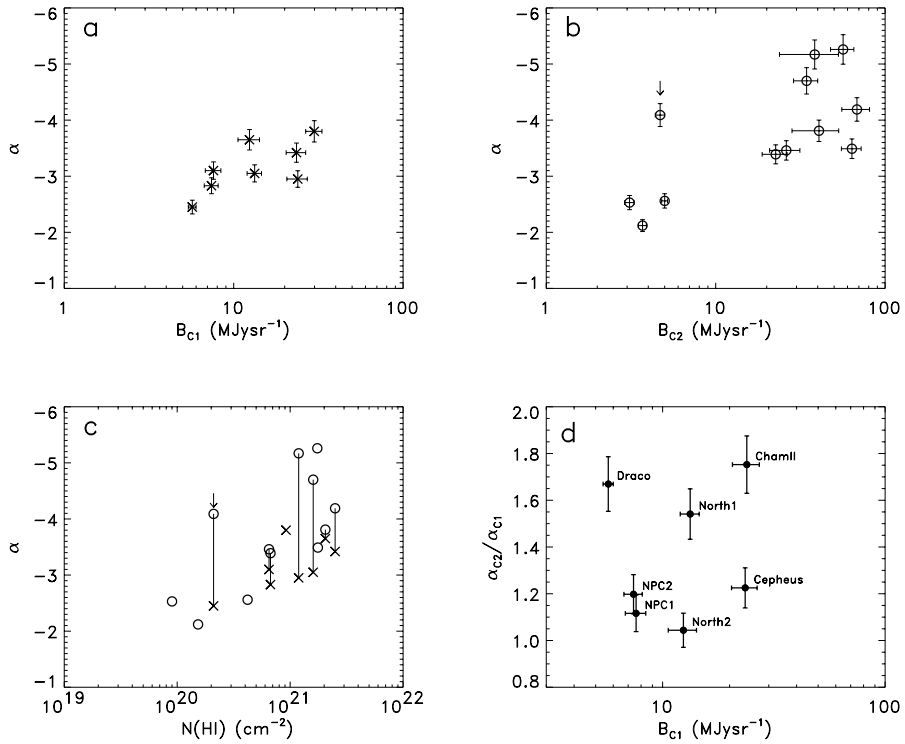

Figure 4. Main results of the power spectrum analysis of 20 ISOPHOT maps. (a) Dependence of spectral index on the 100 μm range median surface brightness B_{C1} (maps observed with the 90 and 100 μm filters). (b) Dependence of spectral index on the 200 μm range median surface brightness B_{C2} (maps observed with the 170, 180 and 200 μm filters). (c) Dependence of spectral index on the average neutral hydrogen column density. Solid lines connect the data points of the same field observed at two wavelengths. Crosses denote 100 μm range measurements, circles 200 μm ones. (d) Ratio of the spectral indices of sky regions measured at both a long wavelength (170–200 μm, α_{C2}) and a short wavelength (90–100 μm, α_{C1}) versus B_{C1}. The regions are labelled by the names as given by the observer.

der the assumption that the FIR radiation at 100 and 200 μm is emitted by the same structures, the ratio α_{C2}/α_{C1} should be ≈ 1. It is obvious, that α_{C2}/α_{C1} varies in the range 1.0–1.8. Since the determination of the spectral index is quite accurate, this deviation cannot be explained by measurement uncertainties.

If the FIR emission of a certain cloud can be well described by one single dust temperature, then the emission measured at two separate wavelengths (e.g. 100 and 200 μm) should be strongly correlated, showing the same spatial structure, and therefore the same power spectrum. On the other hand, the presence of another component with different colour temperature can lead to an excess intensity at one wavelength. This may imply also a different spatial structure of the emission, and therefore different power spectra at the two wavelengths.

We tested the uniqueness of the colour temperatures for fields with measurements at two wavelengths. The colour temperature is represented by the flux ratio of the two wavelengths. In most cases the scatter plot showed a well correlated B_{C1} – B_{C2} emission and could be fitted by one straight line, corresponding to one single dust temperature. Using this relation we derived an excess surface brightness ΔB map, by subtracting the scaled up B_{C1} emission from B_{C2}.

$$\Delta B = B_{C2} - [A_1 \times B_{C1} + A_0] \quad (6)$$

where A_1 and A_0 are the slope and the interception of the linear fit, respectively.

However, there are fields with more than one characteristic colour temperature present in a field. The most conspicuous example is the Cham II field (Fig. 3a and b). In this case, after removing the cirrus contribution according to the procedure of Eq. 6, the excess surface brightness image ΔB still shows the steep index of the original map. The steep ΔB power spectrum can be associated with a bright extended source and, indeed, the region contains dark cloud cores, namely DCld 303.3-14 and DCld 303.5-14.4. A flattening of the ΔB power spectrum at low spatial frequencies provides information on the scale length of these cores. The characteristic sizes derived from the power spectrum agrees well with the typical cold core extent of $\sim 10'$ found by (Tóth et al. 2000) in Chamaeleon, with temperatures of ≤ 15 K.

The correlation of the spectral indices with surface brightness and with neutral hydrogen column density is obvious for faint fields, while a scatter in α is observed for bright and high HI column density fields, as presented in Figs. 4b and c. These fields also show strong molecular (^{12}CO) emission. This large scatter can be observed for N(HI) $\geq 10^{21}$ cm^{-2} (Fig. 4c), which is approximately the column density of the atomic-to-molecular phase transition in the galactic cirrus (de Vries & van Dishoek 1988; Meyerdierks et al. 1990). In these clouds the ratio of molecular hydrogen column density to atomic hydrogen column density may vary in the range of N(H_2)/N(HI) $\approx$ 0.2–5.0 (Magnani et al. 1985). Therefore, clouds showing the same N(HI) may have different total hydrogen masses. This diverse molecular content – and therefore diverse final structure – is a plausible explanation of the observed scatter in the spectral indices.

4. PROSPECTS FOR FAR-INFRARED CIRRUS STUDIES USING THE ISO DATA ARCHIVE

Results based on observations with the ISOPHOT instrument were presented which contributed significantly to a better understanding of the properties of the galactic cirrus emission. However, there are still some issues which can be tackled using the ISO Data Archive, especially when large statistical samples are needed.

As discussed in Sect. 3.1 the analysis of 175 FIR maps provided the so far most accurate confusion noise estimate for ISOPHOT measurements. This estimate is strictly speaking valid only for a certain measurement configuration with the ISOPHOT-C cameras, and should be extended to all measurement modes of the PHT-C cameras and also PHT-P in combination with the FIR filters. According to theoretical considerations the confusion noise depends on the spectral index of the power spectrum. Introduction of the spectral index dependence could further improve the confusion noise estimate (Kiss et al., 2002 in prep.).

The spatial frequency scales available by analysing e.g. PHT22 raster maps are limited to $\sim$0.04 arcmin^{-1}, corresponding to the maximum size of ISOPHOT images. This scale can be extended via the ISOPHOT Serendipity Slews (Bogun et al. 1996). Using these slews spatial frequencies of $\sim$0.01 arcmin^{-1} could be reached, which would provide information on the global behaviour of cirrus structures of a specific sky region (Kiss et al., 2002 in prep.).

ISOPHOT maps obtained at the longest wavelengths may be cross-correlated with visual extinction maps. By this analysis the possible changes in the emissivity properties of big grains may be identified (Ábrahám et al., 2002 in prep.).

ACKNOWLEDGEMENTS

The ISOPHOT Data Center at MPIA is supported by the Max-Planck-Gesellschaft and Deutsches Zentrum für Luft- und Raumfahrt e.V. (DLR) with funds of Bundesministerium für Bildung und Forschung, grant no. 50 QI 0201. This research was partly supported by the ESA PRODEX programme (No. 14594/00/NL/SFe) and by the Hungarian Research Fund (OTKA, No. T037508). P. Á. acknowlegdes the support of the Bolyai Fellowship.

REFERENCES

Bogun, S., Lemke, D., Klaas, U., et al., 1996, A&A 315, 71
Bond, J.R., Carr, B.J., Hogan, C.J., 1986, ApJ 428, 306
Boulanger, F., Pérault, M., 1988, ApJ 330, 964
Désert, F.X., Boulanger, F., Puget, J.L., 1990, A&A 237, 215
Gautier III, T.N., Boulanger, F., Pérault, M., Puget J.L., 1992, AJ 103, 1313
Gillett, F.C., Forrest, W.J., Merill, K.M., 1973, ApJ 183, 87
Green, D.A., 1993, MNRAS 262, 327
Guiderdoni, B., Bouchet, F.R., Puget, J.L., Lagache, G., Hivon, E., 1997, Nature 390, 257
Hauser, M.G., Dwek, E., 2001, ARA&A 39, 249
Helou, G., Beichman, C.A., 1990, The confusion limits to the sensitivity of submilimeter telescopes, in: From Ground-Based to Space-Borne Sub-mm Astronomy, Proc. of the 29th Liège International Astrophysical Coll., ESA Publ., p. 117. (H&B)
Héraudeau Ph., Ábrahám P., Klaas U., Kiss Cs., 2002, ESA SP-481., in press
Herbstmeier, U., Ábrahám, P., Lemke, D., et al., 1998, A&A 332, 739
Kiss, Cs., Ábrahám, P., Klaas, U., Juvela, M., Lemke, D., 2001, A&A 379, 1611
Kiss, Cs., Ábrahám, P., Klaas, U., Lemke, D., Héraudeau, Ph., del Burgo, C., Herbstmeier, U., 2002, A&A, submitted
Lagache, G., Abergel, A., Boulanger, F., Puget, J.-L., 1998, A&A 333, 709
Lagache, G., Puget, J.-L., 2000, A&A 355, 17
Laureijs, R.J., Herbstmeier, U., Ábrahám, P., Klaas, U., Lemke, D., 2000, in: ISO Beyond Point Sources: Studies of Extended Infrared Emission, (eds.) Laureijs, R.J., et al., ESA SP-455, p. 131
Laureijs, R.J., Klaas, U., Richards, P.J., Schulz, B., Ábrahám, P., 2002, The ISO Handbook Vol. IV.: PHT – The Imaging Photo-Polarimeter, SAI–99–069/Dc, Version 2.0
Lemke, D., Klaas, U., Abolins, J., et al., 1996, A&A 315, L64
Low, F., Beintema, D.A., Gautier, F.N., et al., 1984, ApJ 278, L19
Magnani, L., Blitz, L., Mundy, L., 1985, ApJ 295, 402
Mattila, K., Lemke, D., Haikala, L.K., et al., 1996, A&A 315, L353
Meyerdierks, H., Brouillet, N., Mebold, U., 1990, A&A 230, 172
Pei, Y.C., Fall, M.S., Hauser, M.G., 1999, ApJ 522, 604
Puget, J.L., Léger, A., 1989, ARA&A 27, 161
Stutzki, J., Bensch, F., Heithatusen A., Ossenkopf, V., Zielinsky, M., 1998, A&A 336, 697
Tóth, L.V., Hotzel, S., Krause, O., et al., 2000, A&A 364, 769
de Vries, C.P., van Dishoek E.F., 1988, A&A 203, L23

FAR-INFRARED COLOURS OF HIGH-LATITUDE DUST REGIONS

Carlos del Burgo[1], **René J. Laureijs**[2,3], **Péter Ábrahám**[4], **and Csaba Kiss**[4]

[1]Max-Planck-Institut für Astronomie, Königstuhl 17, D-69117 Heidelberg, Germany
[2]ISO Data Centre, European Space Agency, Villafranca del Castillo, PO Box 50727, 28080 Madrid, Spain
[3]European Space & Technology Centre (ESTEC), Keplerlaan 1, Postbus 299, 2200 AG Noordwijk, The Netherlands
[4]Konkoly Observatory of the Hungarian Academy of Sciences, P.O. Box 67, H-1525 Budapest, Hungary

ABSTRACT

We present ISOPHOT observations in the 60-200 μm wavelength range of a sample of high-latitude interstellar regions. A well-defined 150-200 μm emission relationship is followed by all regions, indicating the far-infrared emission of the large grains is a unique function of the dust column density. We find that the 200 μm emission per $A_{\rm V}$ does not drop with temperature suggesting a relative increase in emissivity of the large grains at lower temperatures. The emission of the small dust particles shows significant variations from region to region, especially at low surface brightness level. These variations cannot be accounted completely by temperature changes and the results suggest variations in the relative abundance of smaller grains.

Key words: ISM: clouds, dust, extinction – Infrared: ISM

1. INTRODUCTION

The mid- and far-infrared (FIR) emission of interstellar dust is usually interpreted in terms of a 3-component dust model (PAHs, very small grains and big grains) deduced from IRAS observations (e.g. Desert et al. 1990). Infrared colour variations measured in interstellar cirrus and molecular clouds have proven to be powerful indicators of not only variations due to radiative transfer (Laureijs et al. 1987), but also of variations in the relative abundances between different dust components emitting in the infrared (Boulanger et al. 1990, Lagache et al. 1998).

The submillimetre balloon experiment PRONAOS observed regions where the IRAS 60 μm component appears to be absent (Bernard et al. 1999; Stepnik et al. 2001). PRONAOS showed that the temperature of the large dust grains in those regions is too low (12 K assuming a ν^{-2} emissivity law) for particles with properties derived from the diffuse interstellar medium (DISM) indicating that the dust grains are significantly different from those in the DISM. It is concluded that the grains have changed their properties probably due to adsorption/coagulation of small dust grains onto large grains.

Here we present the infrared colours of eight high-latitude dust regions in the 60 to 200 μm wavelength range observed with ISOPHOT (Lemke et al. 1996) on board of ISO (Kessler et al. 1996). While the short wavelength part ($\lambda \leq 100$ μm) covers emission from both dust components, the longer wavelength emission is only due to the large grains. To estimate the dust column density independently of the infrared emission we have obtained extinction maps from star counts of the Digital Sky Survey (DSS) plates. The unified data set of the FIR and extinction data provide information on several aspects of the infrared signature of dust grains: (1) the variation of the temperature of the large dust grains inside the dust regions and among the regions in the sample, and (2) the behaviour of the emission of the small dust grains with respect to the large grain emission.

2. PRESENTATION OF THE SAMPLE

The observations mainly belong to a dedicated ISOPHOT observing programme of R. Laureijs and collaborators. All regions are situated at Galactic latitudes $|b| > 15^\circ$ and are parts of cloud complexes of peak column densities corresponding to diffuse ($A_V \sim 0.1$) to moderately dense ($A_V \sim 2.5$) ISM. The regions do not contain dominant internal heating sources.

Table 1 lists the ISOPHOT observations. The table contains the region's name deduced from the galactic coordinates, the ISO identification number ($\rm ISO_{id}$) as given in the ISO Data Archive[1], the reference wavelengths of the ISOPHOT filter bands ($\lambda_{\rm ref}$), the size of the area sampled, and the name of the cloud associated to the region.

3. DATA PROCESSING

The regions were mapped with ISOPHOT using the Astronomical Observation Template PHT22 in raster mapping mode with array detectors C100 (3×3 pixels; $46''$ pixel^{-1}) and C200 (2×2 pixels; $92''$ pixel^{-1}). For more details, see the ISOPHOT Handbook (Laureijs et al. 2002).

Data were processed using the ISOPHOT Interactive Analysis software PIA V9.1 (Gabriel et al. 1997). C100 maps were created with the same spatial resolution and grid as those for C200: 1) convolution of the original C100 image with the theoretical C200's beam profile, and 2) resampling according to the pixel size and grid of C200 image. As an example Fig. 1 shows the maps at 90, 120 and 200 μm for the region G187.4-16.7. These maps are representative of the data quality.

In addition, extinction maps for the sample of dust regions were obtained following the method described in Dick-

[1] available at the URL: "http://www.iso.vilspa.esa.es/ida/"

Proceedings of the Symposium *"Exploiting the ISO Data Archive - Infrared Astronomy in the Internet Age"*, 24–27 June 2002, Sigüenza, Spain (C. Gry, S. B. Peschke, J. Matagne et al. eds., ESA SP-511)

Table 1. ISOPHOT observations.

Region	$\alpha_{\rm J2000}$ [hh mm ss]	$\delta_{\rm J2000}$ [dd mm ss]	$ISO_{\rm id}$	$\lambda_{\rm ref}$ [μm]	Area [arcmin^2]	Remark
G6.5+36.5	15 56 0.7	-2 44 21.2	10101301	60, 90	185.2	part of L183E
			10101302	150, 200	206.9	
G89.0-41.2	23 08 35.2	14 46 3.4	21600513	60, 90	51.7	part of MBM55
			21600514	150, 200	206.9	
G90.7+38.0	16 50 53.3	60 55 37.2	27701702	60, 100	112.9	part of Draco
			27701701	150, 200	183.4	
G111.2+19.6	21 02 16.8	76 51 45.1	11101606	150, 200	249.2	part of L1228
G187.4-16.7	5 02 24.3	13 40 58.8	82901030	60, 90	174.6	part of L1563
			82901031	120, 200	253.9	
G297.3-15.7	11 08 6.5	-77 28 53.5	26101501	150	1469.4	part of Chamaeleon
			26101401	200	1469.4	
G301.2-16.5	12 16 22.5	-79 17 8.9	60601026	60, 90	99.3	part of Chamaeleon
			60601027	120, 150, 200	115.2	
G301.7-16.6	12 25 23.8	-79 22 47.6	60600924	60, 90	169.9	part of Chamaeleon
			60600925	120, 150, 200	115.2	

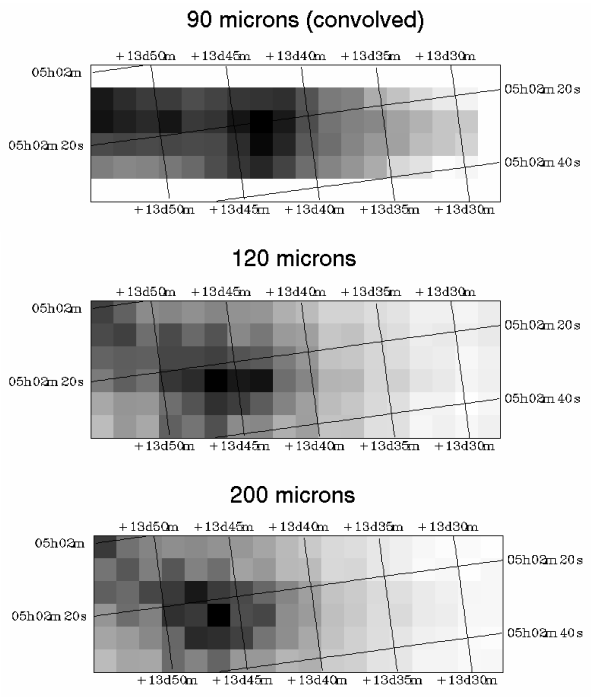

Figure 1. From top to bottom: Surface brightness (I_ν) maps of G187.4–16.7 at 90 (convolved image), 120 and 200 μm. I_ν ranges 19–24, 23–57 and 31–99 MJy sr^{-1} at 90, 120 and 200 μm, respectively. ZL was not subtracted.

man (1978). From the USNO A2.0 catalogue [2], we extracted coordinates and B (blue) magnitudes for stars in the areas of the 200 μm maps of each dust region. The limiting magnitude was chosen to be B = 20^m, which is the completeness limit. Reference zones were selected in the vicinity of the ISOPHOT maps, where no obvious extinction feature was visible in the DSS [3] image. When comparing FIR and extinction data, 200μm maps were smoothed to the 3′ resolution of the extinction maps.

In order to determine absolute surface brightness, we subtracted the zodiacal light (ZL). We made a prediction of the zodiacal sky brightness for each ISOPHOT observation using the COBE/DIRBE Sky and Zodi Atlas (Kelsall et al. 1998). We also determined DIRBE surface brightnesses corresponding to the local sky background (LSB) of the regions from the DIRBE Zodiacal light Subtracted Misssion Averaged (ZSMA) maps. For a complete description of our methods see del Burgo et al. (2002, in preparation).

4. RESULTS AND ANALYSIS

4.1. FIR COLOURS

The emission for each 200 μm position is correlated with the corresponding emission in the other filterbands. Fig. 2 shows, as an example, the emission correlation for G89.0-41.2. Any colour variation will result in a deviation from linearity in the correlation. In the remainder of this paper, the surface brightness emission I_ν (in frequency units MJy sr^{-1}) in the 60, 90, 150 and 200 μm ISOPHOT bands is written as I_{60}, I_{90}, I_{150} and I_{200}, respectively.

For each region, covering a certain 200 μm emission range, the I_{150}-I_{200} correlation is linear within the scatter and no significant change in the slope is observed. We verified the linearity by fitting a second order polynomial to the correlation I_{150} versus I_{200}. The coefficient related to the quadratic term turned to be in all cases insignificant, less than 1 σ. Hereafter we refer to the *unimodal* case if the correlation is linear.

For wavelengths shorter than 150 μm, correlations for regions like G89.0-41.2 and G301.2-16.5 are also unimodal. However, G187.4-16.7 and G301.7-16.6 exhibit a colour variation which is significantly better modeled by two linear ramps (case *bimodal*) with a wavelength-dependent turn-over point. These two regions share the same 200 μm dynamical range and present

[2] available at the URL: “http://www.nofs.navy.mil”

[3] available at the URL: “http://archive.eso.org/dss/dss”

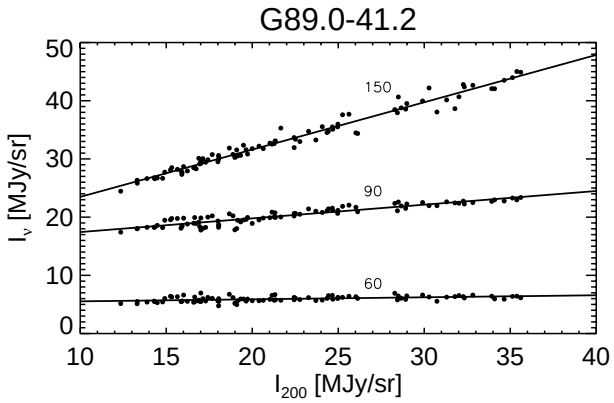

Figure 2. I_ν versus I_{200} of G89.0-41.2 for wavelengths $\lambda_{\rm ref}$ = 60, 90 and 150 μm. Emission maps were smoothed to the resolution of the 200 μm scan. For a better view, maps were also shifted -10 MJy sr^{-1} at λ= 90 and 150 μm.

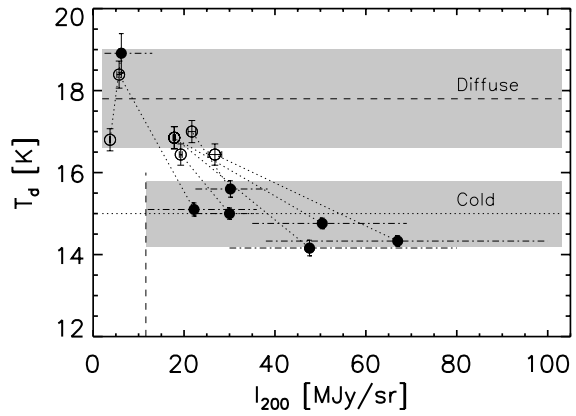

Figure 3. Temperatures of the large-dust-grains versus mean 200 μm emission corresponding to the dust regions (closed circles) and to the LSB (open circles) surrounding these regions. Dotted lines link the two temperatures for each region. Dot-dashed lines indicates the 200 μm emission range for each region. Mean temperatures for the cold (dotted line) and diffuse components (dashed line) and respective dispersions (shadowed boxes) obtained from FIRAS and DIRBE (Lagache et al. 1998) are also shown. The vertical axis indicates the minimum 200 μm emission for existing a cold component derived from results of Lagache et al. (1998).

a similar change in the slope of 120-150μm correlation. The significant flattening observed in the correlations indicates a decrease in the emission towards zones of high 200 μm surface brightness. G111.2+19.6 and G297.3-15.7 cannot be classified due to a lack of short wavelength measurements.

The slopes for *unimodal* and *bimodal* cases of the different correlations are determined from a least squares linear fitting. For G297.3-15.7 we constrained the 200μm emission range up to 100 MJy sr^{-1}. See the regression fits of our example in Fig. 2.

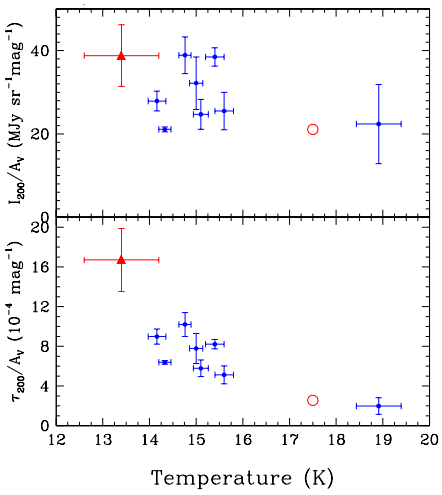

Figure 4. Top: The 200 μm surface brightness normalised to $A_{\rm V}$ as a function of dust temperature. Bottom: The derived opacity τ_{200} as a function of $T_{\rm d}$. The dots at 17.5 K mark the values for the DISM. The dot in the top-left correspond to a PRONAOS mesurement of Polaris cloud (Bernard et al. 1999).

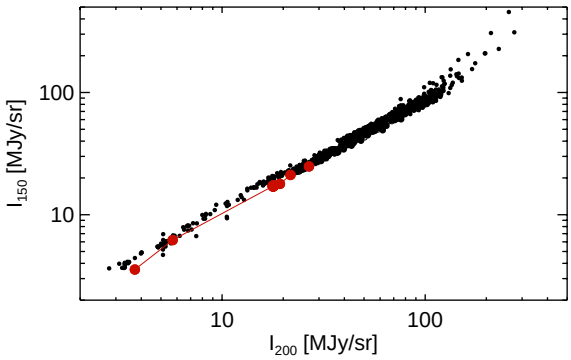

Figure 5. Surface brightness at 150 μm versus surface brightness at 200 μm in logarithmic scale for all regions. Large symbols (connected by a solid line) correspond to the LSBs.

4.2. Colour temperature from $I_{150} - I_{200}$

We computed a temperature, $T_{\rm d}$, from the colour-corrected slope of correlation $I_{150} - I_{200}$ for each region. We assumed each SED is well-represented by a modified black body $F_\nu \propto \nu^\beta B_\nu(T_{\rm d})$, where $B_\nu(T_{\rm d})$ is the Planck function, ν is the frequency, and β (=2) is the power in the dust emissivity. $T_{\rm d}$ versus $< I_{200} >$ are shown in Fig.3. We also derived temperatures for surrounding LSBs from the predicted DIRBE surface brightnesses at 150 and 200 μm.

4.3. Extinction and FIR emission

For each region, we performed a pixel-to-pixel correlation between the extinction map and the emission at 200 μm. The extinction data were transformed from $A_{\rm B}$ to $A_{\rm V}$ assuming a standard extinction law with $R_V = 3.1$ (Mathis, 1990). We

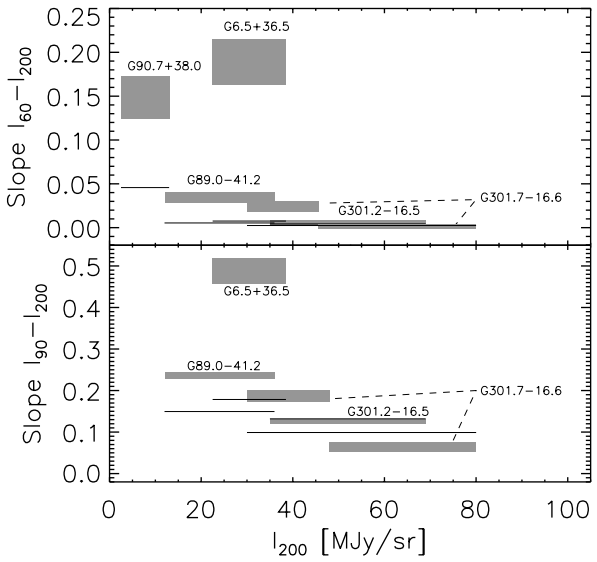

Figure 6. Color corrected slopes from correlations I_{60}-I_{200} and I_{90}-I_{200} (rectangles) and predictions from the correlation I_{150}-I_{200} (solid lines). The width and height of the rectangles correspond to the 200μm emission range and the error of the slopes, respectively. Note that predicted and observed values share a common I_{200} range.

determined the slope of the I_{200} versus $A_{\rm V}$ correlation by applying a least squares fitting procedure. The resulting slopes I_{200}/A_V versus temperatures are plotted in the upper panel of Fig. 4. Most striking is the fact that the 200 μm emission per $A_{\rm V}$ does not drop with decreasing temperature.

4.4. Properties of the large dust grains

The temperatures T_d show a gradual variation as a function of mean 200 μm surface brightness of the region (see Fig. 3). The smooth change in temperature is directly inferred when plotting the 150-200 μm correlations for all the regions, which follow a unique relationship (see Fig. 5). The systematic variation among the regions in the sample excludes the possibility that the emission of a region (above a constant background) comes from a superposition of unrelated diffuse clouds. Consequently, mean temperature in a region depends systematically on the dust column density above the background.

For each region, we computed the FIR grain opacity at 200 μm (τ_{200}) normalized to $A_{\rm V}$ from T_d and $I_{200}/A_{\rm V}$. We find that the values of $\tau_{200}/A_{\rm V}$ are within a range of $(5-10)\times 10^{-4}$ mag^{-1}.

In Fig. 4 we investigate the ratios $I_{200}/A_{\rm V}$ and $\tau_{200}/A_{\rm V}$ as a function of T_d. The calculation of τ_{200} depends on T_d, but the quantity τ_{200} should not be. The ratio $I_{200}/A_{\rm V}$ is independent of the measurement of T_d. There is no indication that the 200 μm emission drops with decreasing temperature which would be the expected trend for cooler grains. On the contrary, the ratios are systematically higher than the ratio derived for the DISM. The resulting normalized opacities exhibit a *systematic increase* with decreasing temperature. We infer that the emitting grains systematically change properties as a function of temperature.

4.5. Colour variations of the small dust grains

For the emission shortward of 150 μm the correlation diagrams show both *unimodal* as well as *bimodal* behaviour. We have plotted the slope of correlation $I_\lambda - I_{200}$ at 60 and 90 μm versus I_{200} (see Fig. 6). We included the predicted emission from the large grain component by extrapolating the modified blackbody curves fitted at 150 and 200 μm down to 60 and 90 μm.

In some cases we note an FIR excess at 60 and 90 μm confirming the presence of an additional emission component due to small grains. At high 200 μm brightness level the 60 μm and 90 μm emission show a clear flattening wrt the 200 μm emission suggesting that above a certain I_{200} the small grain emission disappears. Regions that are situated on a high 200 μm surface brightness pedestal are very likely embedded in an envelope with small grain emission.

ACKNOWLEDGEMENTS

CdB acknowledges the support by the EC TMR Network POE. PÁ thanks the support of the Hungarian Research Fund (Grant no. T037508) and of the Bolyai Fellowship.

REFERENCES

Bernard J-.P., et al., 1999, A&A 347, 640
Boulanger F., et al., 1990, ApJ 364, 136
Desert F.-X., Boulanger F. & Puget J. L., 1990, A&A 237, 215
Dickman R. L. 1978, AJ, 83, 363
Gabriel C., et al., 1997, in *Proc. of the ADASS VI Conference* (eds.: G. Hunt, H.E. Payne), 108
Kelsall T., et al., 1998, ApJ 508, 44
Kessler M.F., et al., 1996, A&A 315, L27
Lagache G., et al., 1998, A&A 333, 709
Laureijs, R. J., et al., 2002, The ISO Handbook Vol. IV (PHT), ESASP 1262
Laureijs,R. J., et al., 1987, A&A, 184, 269
Lemke D., et al., 1996, A&A 315, L64
Mathis J.S. 1990, AAR&A 168, 271
Stepnik et al. 2001, ESASP 460, 269

GAS TO DUST INTERACTION STUDIES WITH THE ISO DATA BASE

Emilie Habart[1], Laurent Verstraete[2], François Boulanger[2], Guillaume Pineau des Forêts[2], and Alain Abergel[2]

[1]Osservatorio di Arcetri, Largo E. Fermi 5, Firenze, Italia
[2]Institut d'Astrophysique Spatiale, Université Paris-Sud, Bât. 121, 91405 Ors ay Cedex, France

ABSTRACT

Several processes couple dust to the chemical and thermodynamical evolution of the interstellar gas. The ISO data allows us for the first time to conduct a detailed study of this interplay over a wide range of gas density and radiation field strength. Detailed confrontation between ISO observations of both gas and dust emission from the nearest photon-dominated regions (PDRs) of the ISM with model predictions allows us to constrain important processes coupling gas to dust such as the photoelectric heating on dust grains (Habart et al. 2001), or the formation of H_2 on grain surfaces (Habart et al. 2002a).

An important issue raises by ISO concerning our understanding of the local microphysics of the ISM is the high gas temperature (T_{gas} ∼300-700 K) observed towards several PDRs. In this context, our description of the main physical and chemical processes involving PDRs has to be reconsidered. For dense PDRs ($n_H \gtrsim 10^4$ cm^{-3}) exposed to moderate radiation field ($100 \leq \chi \leq 10^3$), a high H_2 formation rate ($R_f \geq 10^{-16}$ cm^3 s^{-1} at $T_{gas} \geq 350$ K) seems to be required to explain the observed H_2 excitation.

Key words: ISO – ISM: clouds - ISM: dust, extinction - atomic processes - molecular processes - radiative transfer

1. INTRODUCTION

In the interstellar medium (ISM), the interplay between gas and dust is essentially of three types: thermal, chemical and dynamical. First, in the space penetrated by stellar radiation, the photoelectric effect on dust grains are the main heating source for the gas. Second, chemical reactions on dust surfaces are an essential part of interstellar chemistry. Formation of molecular hydrogen takes place on the surface of dust grains and initiates all the gas chemistry. Finally, small dust particles charged may in some environments be the main coupling agent between interstellar matter and the magnetic field.

The ISO instruments with their high spectral as well as spatial resolution and their large spectral range (2-200 μm which encompasses the gas cooling lines and the dust emission) are very well suited to study both dust and gas in nearby interstellar molecular clouds. Spectroscopic and imaging observations obtained with ISO of numerous photon-dominated regions of the ISM have provided new perspectives on the structure and physical conditions of the interstellar matter. Indeed, PDRs, where stellar radiation (UV, 6-13.6 eV) plays a dominant role in determining the chemical and thermal state of the gas (for a recent review see Hollenbach & Tielens 1999), are privileged objects to study the physical and chemical processes of the interstellar medium. Then, ISO data allows us for the first time to study the interplay between gas and dust at small scales and towards a large range of physical conditions.

Detailed comparison between ISO observations, in conjunction with ground-based NIR imaging, and PDR theoretical model calculations allows us to address a number of important outstanding questions, like: (i) the structure of the interstellar matter (Abergel et al. 1999; Habart et al. 2002b), (ii) the dominant heating and cooling processes (Draine & Bertoldi 1999; Weingartner & Draine 1999; Liseau et al. 1999; Habart et al. 2001; Vastel et al. 2001) and, (iii) the H_2 formation process (Bertoldi 1997; Habart et al. 2002b). PDR studies of both gas and dust emission, which provides complementary informations, permits us to develop diagnostics of physical conditions and processes of the ISM.

In this paper, we first summary recent results derived from ISO spectroscopic observations of several PDRs (Sect. 2). Then, we confront these results to model predictions and discuss the main processes involving H_2 (Sect. 3). In particular, we investigate the impact of the H_2 formation efficiency on the H_2 lines emission (Sect. 4). The ratio between H_2 rotational and rovibrational lines emission is proposed as a diagnostic of the H_2 formation rate. Finally, we discuss the new perspective opened by ISO on the H_2 formation process and, how the ISO data base can be used in conjunction with new and future instruments to study the interplay between gas and dust (Sect. 5).

2. H_2 AS A THERMAL PROBE

A significant contribution of ISO to our understanding of PDRs is due to its ability to observe with the Short Wavelength Spectrometer (SWS, Kessler 1996) a series of pure rotational transition lines of molecular hydrogen over a wide range of excitation conditions and gas density. Before ISO, only the 0-0 S(1) and S(2) lines had been detected towards the Orion Bar (Parmar et al. 1991).

The (v, J) excited states of H_2 can be populated by inelastic collisions with gas phase species, UV pumping and by the formation process on dust grains. For the physical conditions prevailing in bright PDRs ($n_H \geq 10^4$ cm^{-3}, $T_{gas} \sim$ a few 100 K), collisions are expected to maintain the lowest rotational levels of H_2 (v=0, $J \leq$5) in thermal equilibrium (Le Bourlot et al.

Proceedings of the Symposium *"Exploiting the ISO Data Archive - Infrared Astronomy in the Internet Age"*, 24–27 June 2002, Sigüenza, Spain (C. Gry, S. B. Peschke, J. Matagne et al. eds., ESA SP-511)

Table 1. Gas temperatures derived from ISO-SWS observations of H_2 rotational lines towards several PDRs

Object	χ^1 (Draine	n_H (cm^{-3})	T_{gas} (K)	R_{op}	ref.
S140cut	9	10^3	<320	-	1
Ced201	12	1.2 10^4	330	-	2-3
OphW	235	10^4	350	1	4
S140	235	10^4	500	3	5-6
IC63	650	10^5	650	-	3-7
NGC 2023 (60S)	3 10^3	5 10^4	333	1	8-9
Orion Bar	2.4 10^4	5 10^4	400	3	10-11

[1] Scaling factor which represents the strength of the interstellar standard radiation field of Draine (1978).
References. (1) Li et al. (2002); (2) Kemper et al. (1999); (3) Thi et al. (1999); (4) Habart et al. (2002a); (5) Timmermann et al. (1996); (6) Draine & Bertoldi (1999); (7) Jansen et al. (1994); Jansen et al. (1995); (8) Moutou et al. (1999); (9) Draine & Bertoldi (2000); (10) Habart (2001) and references therein.

1999). Therefore ISO measurements of H_2 lines emission from low rotationally excited levels provide a good indicator of the gas temperature in the H_2 emission zone.

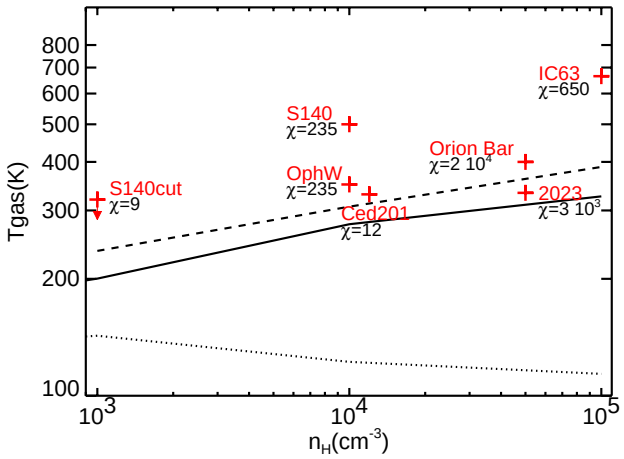

Figure 1. Gas temperature in the H_2 excitation zone, as a function of gas density, predicted by standard PDR models characterized by different incident radiation field : χ=10 (dotted line), χ=1000 (solide line), and $\chi = 10^5$ (dashed line). The gas temperature derived from ISO-SWS observations of H_2 pure rotational lines towards several PDRs have been superposed (crosses). Their gas density have been taken from the literature (see Table 1).

The gas temperature and the ortho-to-para ratio, R_{op}, derived towards several PDRs - which sample well the range of radiation field intensity covered by the SWS observations - are reported in Table 1. At the low excitation end, we have the peripheral region of the molecular cloud L1204/S140 (S140cut, Li et al. 2002 and the cool PDR Ced 201 (Kemper et al. 1999). Then, we have dense PDRs exposed to moderate incident radiation field, the Ophiuchi west interface (OphW, Habart et al. 2002a), the S140 PDR (S140, Timmermann et al. 1996; Spaans & van Dishoeck 1997; Draine & Bertoldi 1999) and IC63 (Jansen et al. 1994; Jansen et al. 1995; Thi et al. 1999). We also have the reflection nebula NGC 2023 where we focus on the filament at 60" south of the central star (Moutou et al. 1999). Finally, at the high excitation end, we have the Orion Bar taken at the position of the peak of the fluorescent H_2 emission (van Der Werf et al. 1996). Over this range of PDRs physical conditions, ISO has shown unequivocal presence of gas temperatures in the 300-700 K range in a portion of the PDR where the H_2 fraction is appreciable (see Table 1). These data provide a new test of PDR model, which still contain many unknowns. In the next section, we compare PDR model predictions to the observations.

3. PDR MODEL PREDICTIONS

We use an updated version of the PDR model described in Le Bourlot et al. (1993). In this stationary model, a PDR is represented by a semi-infinite plane-parallel slab with an incident radiation field on the interface. The incident radiation field is characterized in term of χ, a scaling factor which represents the strength of the radiation field at λ = 1000 Å in units of 1.6 10^{-3} erg/s/cm^2 (Habing 1968). The input parameters are (i) χ, the scaling factor for the radiation field, and (ii) n_H the gas density. With these inputs the model solves the chemical and thermal balances starting from the slab edge at each A_v-step in the cloud. The H_2 abundance results from a balance between the formation of H_2 on dust grains and the photodissociation of H_2 by FUV flux, which is attenuated by dust extinction and self-shielding in the H_2 lines. The adopted H_2 formation rate, R_f (cm^3 s^{-1}), is a semi-empirical rate coefficient:

$$R_f = \gamma \times \left(\frac{T_{gas}}{100K}\right)^{0.5} \times S(T_{gas}) \quad (1)$$

with γ a numerical factor in cm^3 s^{-1}, T_{gas} the gas temperature and S the sticking coefficient of H_2 onto grains equal to 1/(1+ T_{gas} / 400 K + (T_{gas} / 400 K)^2) (Burke & Hollenbach 1983; Bertoldi 1997). The standard value derived by Jura (1975) from observations of interstellar diffuse cloud - $R_f^0 = 3\ 10^{-17}$ cm^3 s^{-1} at $T_{gas} \sim$ 70K - corresponds to $\gamma = 4.3\ 10^{-17}$ cm^{-3} s^{-1}. We assume an equipartition of the H_2 formation energy between the transitional, rovibrational and vibrational degrees of freedom is adopted (for more details see Habart et al. 2002a).

In Fig. 1, we compare the gas temperature observed in the H_2 emission zone towards the SWS PDRs sample (see Table 1) to the gas temperature predicted by standard isochoric PDR models. The gas temperatures observed are for most of PDRs higher than expected. Moreover, for several of these PDRs, standard models underestimate the intensity in the H_2 rotational lines by up to an order of magnitude. Other authors reached the same problem (see Bertoldi 1997; Draine & Bertoldi 1999; Thi et al. 1999; Kemper et al. 1999; Li et al. 2002). These discrepancies may be due in part to our underlying assumptions of planar geometry and uniform density. However, detailed studies taking into account a more realistic geometry and

the gas density distribution show the same problem ,i.e. Habart et al. (2002a). Then, to explain this disagreement reconsideration of our description of the local physical and chemical processes are required.

To remedy these discrepancies, several suggestions have been made:

1. first, the higher gas temperature may be due to an enhancement of the heating rate. In most PDRs, the main heating process is the photoelectric heating on small dust grains. Our present theoretical description of this mechanism (Bakes & Tielens 1994; Weingartner & Draine 2001) is consistent with recent ISO observations (Habart et al. 2001). On the contrary, variations of abundance and size distribution of small dust grains, which have been observed in the ISM (Boulanger et al. 1988; Boulanger et al. 1990; Bernard et al. 1993) and could have important impact on the gas heating rate (Habart et al. 2001), may be an explanation. Draine & Bertoldi (2000) have in particular shown that increased photoelectric heating rates based on an enhanced dust-to-gas ratio in the PDR due to gas-grain drift can reproduce H_2 observations in the reflection nebula NGC 2023.
2. Secondly, the H_2 formation process on dust grains can be invoked. The value of H_2 formation rate, R_f, which plays an important role in PDRs because it controls the location of the H^0/H_2 transition, is particularly uncertain in excited regions of the ISM. A larger H_2 formation rate at high gas temperatures, moving the H^0/H_2 transition zone closer to the warm edge, could explain the present ISO results (Bertoldi 1997; Habart et al. 2002a).
3. Finally, non-equilibrium processes, not taken into account in current stationary PDR models, which could affect the thermo-chemical structure of the gas (Spaans 1995; Joulain et al. 1998; Falgarone et al. 2000) can be invoked. ISO-SWS observations towards PDRs (as ρ Oph-W, NGC 2023 or NGC 7023: Habart et al. 2002a; Moutou et al. 1999; Fuente et al. 2000,) have provided evidence of non equilibrium ortho-to-para H_2 ratio.

In this study, we investigate the impact of the H_2 formation rate R_f on the H_2 excitation.

4. H_2 FORMATION RATE

The ratio between the H_2 low pure rotational (v=0, $J \leq$5 mainly populated by collisions) and rovibrational ($v \geq$1 mainly populated by UV pumping) lines emission is a function of both gas temperature and UV flux in the H_2 emission zone. It is therefore expected to be strongly dependent on the H_2 formation rate, which controls the location of the H^0/H_2 transition region. In this work, we then propose to use the $I_{H_2\ rotational}$/-$I_{H_2\ rovibrational}$ ratio, essentially independent on the geometry and the total column density, as a diagnostic of R_f.

In Fig. 2, we show the 0-0 S(3)/1-0 S(1) H_2 line emission ratio integrated over the PDRs predicted by the model for different χ and n_H as a function of the H_2 formation rate. For the range of χ and n_H explored, the gas temperature profile is not much affected by the enhancement of R_f because the dominant heating and cooling mechanisms (photoelectric heating and fine structure line emission of O^0 and C^+) not evolve H_2. As expected, the increase of R_f results in stronger low rotational (higher T_{gas}) and stronger rovibrational (higher UV flux) line emission. Moreover, as we can in Fig. 2, the contribution of collisional excitation relative to UV pumping increases with R_f. For high n_H ($\geq$ 5 10^4 cm^{-3}) and χ ($\geq$ 10^4) and high R_f ($\geq 10 \times R_f^0$), UV pumping contribution becomes in revenge more important. Finally, we note that for PDRs with n_H/χ >100, for which the H^0/H_2 transition zone is mainly governed by the H_2 self-shielding process, increasing R_f has low effect, because H_2 forms even with a low R_f in the warm zone.

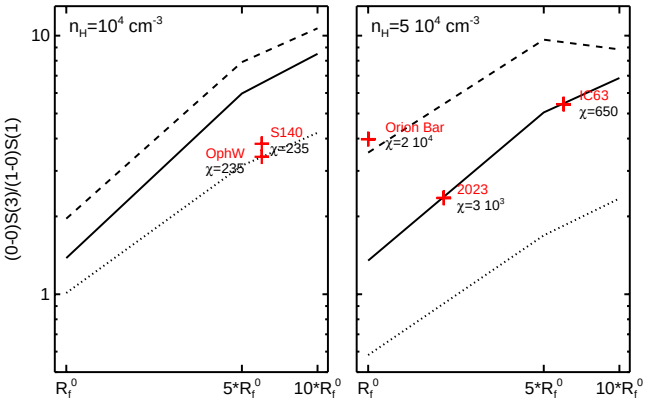

Figure 2. Ratio of the 0-0 S(3)/1-0 S(1) H_2 line emission predicted by models characterised by different incident radiation field - χ=300 (dotted lines), χ=10^3 (solid lines) and χ=10^4 (dashed lines) - for two different gas density as a function of the H_2 formation rate. R_f^0 corresponds to the reference value derived by Jura (1975).

We confront these predictions to H_2 line emission ratio observed towards some PDRs listed in Table 1. The emission in the 0-0 S(3) and 1-0 S(1) H_2 line has been respectively taken from SWS and ground based observations. The data has been corrected for dust attenuation using the extinction curve of Draine (1989) and visual extinction taken from the literature. For dense PDRs excited by moderate χ, *i.e.* OphW, S140 and IC63, we find that a higher H_2 formation rate (6 times the rate derived by Jura 1975) is required to reproduce the H_2 lines emission ratio observed. At the high excitation end, *i.e.* NGC 2023 and the Orion Bar, we find in revenge that, a lower R_f matches the observations. These respective R_f values, which account for the relative contribution of collisional to UV pumping, reproduce also the observed intensities of the both 0-0 S(3) and 1-0 S(1) H_2 lines taken into account the PDR inclination (see Habart et al. 2002c). Furthermore, note that for the low excited S140 peripherical PDR (S140cut), increasing R_f improves considerably the comparison with observations, al-

though the models still fall short by a factor of few (Li et al. 2002).

5. DISCUSSION, PERSPECTIVES

The H_2 formation values found here in warm excited regions of the ISM rules out a formation process where two hydrogen atoms physisorbed on the surface of a big grain recombine to form H_2. Such a mechanism is efficient only in regions moderately irradiated (χ <100) where the equilibrium temperature of big grains drops below ∼20 K (Pirronello et al. 1997; Pirronello et al. 1999; Katz et al. 1999). In the case of our photon-dominated regions, the high temperature of big grains ($\leq$35 K) favors thermal evaporation and maintains the physisorption rate of hydrogen at a low value. This suggests that formation of H_2 on big grains (at least in PDRs) involves chemically attached H-atoms. In this second process, H_2 could form by (i) a prompt reaction of free H atoms from the gas phase with chemisorbed H atoms (Duley 1996; Parneix & Brechignac 1998) or through (ii) the recombination of a physisorbed H with a chemisorbed H atom (Habart 2001; Habart et al. 2002c; Cazaux & Tielens 2002). Considering the fact that small carbonaceous grains make a dominant contribution to the total grain surface and have numerous chemically bonded hydrogen atoms, it is plausible that they play a dominant role in H_2 formation by chemisorption.

It must be emphasized that these results are reached assuming two main points. First, variations of abundance and/or size distribution of small dust grains which can have important impact on the thermal gas evolution - via the photoelectric effect - have not been considered. However, the increase of the photoelectric rate results in stronger low H_2 rotational lines emission, while the high H_2 rotational ($J > 5$) and rovibrational lines emission are not affected and remain underestimated (see Habart et al. 2002a). Nevertheless, in the case of H_2 forms on small carbonaceous grains, increasing their abundance would alter the thermochemical properties of the PDR by increasing the H_2 formation rate and by increasing the grain photoelectric heating rate and could be an alternative explanation. Second, we have placed ourselves in the case of a static, equilibrium PDR. In reality, motions due to the propagation of the photodissociation front and/or the presence of turbulent velocity fields may exist and could affect the H_2 line emissions (Stoerzer & Hollenbach 1998). Nevertheless, for most of the PDRs studied here advection velocities might be less than 1 km/s. Moreover, in the case of the ρ Oph-W PDR, we find based on qualitative arguments that advection could not account for the observed H_2 lines intensities (Habart et al. 2002a). However, out-of-equilibrium modelling is warranted to estimate quantitatively the effect of advection. In addition, observations at high spatial and spectral resolution should be used to trace the velocity field of advection motions. The conjunction between the ISO data and the future Herschel-HIFI observations will in particular improve our understanding on the non-equilibrium processes in PDRs.

ISO camera observations of small carbonaceous grains and H_2 emission combined with ground based observations of H_2 fluorescent emission, at high angular resolution, gives us access to study the respective behaviour of the emission of these two species, which is another important aspect to address the question of the formation of H_2 on small grains. Furthermore, combining ISO data with new FUSE observations allow us the possibility to probe the H_2 formation efficiency from the diffuse ISM to star formation regions. Using these different observational constraints, we are currently studying the dependence of the H_2 formation efficiencies on the physical conditions and grain characteristics and, confront it to H_2 formation mechanisms (Habart et al. 2002c).

The new perspective opened by ISO on the H_2 formation process will be investigated with future instruments. Shortly, SIRTF will give us access to map of both small and big grains emission at high angular resolution and to H_2 rotational lines observations towards hundreds of new targets. Further studies of both dust and H_2 emission observed by SIRTF will enable us to determine the dependence of H_2 formation with dust grains properties. In the longer term, a mid-infrared spectrometer on the NGST (MIRI, 5-29μm) will observe gas and dust emission with several order-of-magnitude improvement in sensitivity which would expand this kind of approach to the study of various astrophysical environments.

Finally, it must be emphasized that the dust to gas interactions studies towards PDRs which permit us to quantify the efficiency of the processes coupling gas to dust, give on the other hand the possibility to probe the physical conditions and to study the evolution of dust grains properties. We have in particular shown that the ratio between the H_2 fluorescent and aromatic dust emission permits to constrain the local gas density and/or the intensity of the ambient UV radiation field independently on the geometry and of the total column density of the object studied (Habart et al. 2002b). Then, combining ISOCAM with near-IR ground base data (NTT, VLT) will permit us to probe the physical conditions of the interstellar matter in numerous regions.

REFERENCES

Abergel, A, Andre, P, Bacmann, A, Bernard, J. P, Bontemps, S, Boulanger, F, Coulais, A, Desert, F. X, Falgarone, E, Kaas, A. A, Huldtgren, M, Miville-Deschenes, M. A, Nordh, L, Olofsson, G, Perault, M, & Puget, J. L. Spatial distribution of dust from cirrus to dense clouds. In *The Universe as seen by ISO*, page 615, 1999.

Bakes, E. L. O & Tielens, A. G. G. M. 1994, ApJ, 427:822.

Bernard, J. P, Boulanger, F, & Puget, J. L. 1993, A&A, 277:609.

Bertoldi, F., 1997, Iso: A novel look at the photodissociated surfaces of molecular clouds (invited paper). In *First ISO Workshop on Analytical Spectroscopy*, page 67

Boulanger, F, Beichman, C, Desert, F. X, Helou, G, Perault, M, & Ryter, C. 1988, ApJ, 332:328.

Boulanger, F, Falgarone, E, Puget, J. L, & Helou, G. 1990, ApJ, 364:136.

Burke, J. R & Hollenbach, D. J. 1983, ApJ, 265:223.
Cazaux, S & Tielens, A. G. G. M. 2002, ApJ, 575:L29.
Draine, B. T & Bertoldi, F. Heating the gas in photodissociation regions. In Cox, P & Kessler, M, editors, *The Universe as seen by ISO*, page 553, 1999.
Draine, B & Bertoldi, F. Theoretical models of photodissociation fronts. In *H2 in Space*, page 131, 2000.
Draine, B. T., 1978, ApJS, 36:595
Draine, B. T. Interstellar extinction in the infrared. In *Infrared Spectroscopy in Astronomy*, page 93, 1989.
Duley, W. W. 1996, MNRAS, 279:591.
Falgarone, E, Verstraete, L, Hily-Blant, P, & Pineau Des Forêts, G. Hot chemistry in the cold diffuse medium: spectral signatures in the h2 rotational lines. In *Molecular Hydrogen in Space, Cambridge University Press*, page 225, 2000.
Fuente, A, Martin Pintado, J, & Rodriguez Fernacute. 2000, A&A, 354:1053.
Habart, E, Verstraete, L, Boulanger, F, Pineau Des Forêts, G, Le Peintre, F, & Bernard, J. P. 2001, A&A, 373:702.
Habart, E, Abergel, A, Boulanger, F, & Verstraete, L. 2002b, *in preparation*.
Habart, E, Boulanger, F, Verstraete, L, Abergel, A, Falgarone, E, & Pineau des Forêts, G. 2002a, *accepted to A&A*.
Habart, E, Boulanger, F, Verstraete, L, Pineau des Forêts, G, & Walmsley, M. 2002c, *in preparation*.
Habart, E. 2001, *Ph.D thesis, "Couplage entre le gaz et les grains dans le milieu interstellaire"*. University of Paris 7.
Habing, H. J. 1968, *Bull.Astron.Inst.Netherlands*, 19:421.
Hollenbach, D. J & Tielens, A. G. G. M. 1999, Rev. in Modern Physics, 71:173.
Jansen, D. J, van Dishoeck, E. F, & Black, J. H. 1994, A&A, 282:605.
Jansen, D. J., van Dishoeck, E. F., Black, J. H., Spaans, M., & Sosin, C. 1995, A&A, 302:223.
Joulain, K., Falgarone, E., Des Forêts, G. P., & Flower, D. 1998, A&A, 340:241.
Jura, M. 1975, ApJ, 197:575.
Katz, N, Furman, I, Biham, O, Pirronello, V, & Vidali, G. 1999, ApJ, 522:305.
Kemper, C, Spaans, M, Jansen, D. J, Hogerheijde, M. R, van Dishoeck, E. F, & Tielens, A. G. G. M. 1999, ApJ, 515:649.
Kessler, M. F, Steinz, J. A, Anderegg, M. E, Clavel, J, Drechsel, G, Estaria, P, Faelker, J, Riedinger, J. R, Robson, A, Taylor, B. G, & Ximenez De Ferran, S. 1996, A&A, 315:L27.
Le Bourlot, J, Pineau des Forêts, G, Roueff, E, & Flower, D. R. 1993, A&A, 267:L233.
Le Bourlot, J, Pineau des Forêts, G, & Flower, D. R. 1999, MNRAS, 305:L802.
Li, W, Evans, N. J. I, Jaffe, D. T, van Dishoeck, E. F, & Thi, W. F. 2002, ApJ, 568:242.
Liseau, R, White, G. J, Larsson, B, Sidher, S, Olofsson, G, Kaas, A, Nordh, L, Caux, E, Lorenzetti, D, Molinari, S, Nisini, B, & Sibille, F. 1999, A&A, 344:L342.
Moutou, C, Verstraete, L, Sellgren, K, & Léger, A. The rich spectroscopy of reflection nebulae. In *The Universe as Seen by ISO*, page 727, 1999.
Parmar, P. S, Lacy, J. H, & Achtermann, J. M. 1991, ApJ, 372:L25.
Parneix, P & Brechignac, P. 1998, A&A, 334:363.
Pirronello, V, Liu, C, Shen, L, & Vidali, G. 1997, ApJ, 475:L69.
Pirronello, V, Liu, C, Roser, J. E, & Vidali, G. 1999, A&A, 344:681.
Spaans, M & van Dishoeck, E. F. 1997, A&A, 323:953.
Spaans, M. 1995, *Ph.D thesis*, 306:306.
Stoerzer, H & Hollenbach, D. 1998, ApJ, 495:853.
Thi, W. F, van Dishoeck, E. F, Black, J. H, Jansen, D. J, Evans, N. J, & Jaffe, D. T. Weak H_2 emission from diffuse and translucent clouds. In *The Universe as Seen by ISO*, page 529, 1999.
Timmermann, R, Bertoldi, F, Wright, C. M, Drapatz, S, Draine, B. T, Haser, L, & Sternberg, A. 1996, A&A, 315:L281.
van Der Werf, P. P, Stutzki, J, Sternberg, A, & Krabbe, A. 1996, A&A, 313:633.
Vastel, C, Spaans, M, Ceccarelli, C, Tielens, A. G. G. M, & Caux, E. 2001, A&A, 376:1064.
Weingartner, J. C & Draine, B. T. Grain dynamics in photodissociation regions. In *The Universe as Seen by ISO*, page 783, 1999.
Weingartner, J. C & Draine, B. T. 2001, ApJS, 134:263.

THE ISO LWS HIGH RESOLUTION SPECTRAL SURVEY TOWARDS SAGITTARIUS B2

Edward T. Polehampton[1,2], Bruce M. Swinyard[1], and Jean-Paul Baluteau[3]

[1]Rutherford Appleton Laboratory, Chilton, Didcot, Oxon, OX11 0QX, UK
[2]Astrophysics, University of Oxford, Keble Road, Oxford, OX1 3RH, UK
[3]Laboratoire d'Astrophysique de Marseille, CNRS & Université de Provence, BP 8, F-13376 Marseille Cedex 12, France

ABSTRACT

The giant molecular cloud complex, Sagittarius B2, was observed in many separate observations with the ISO Long Wavelength Spectrometer. The high resolution Fabry-Pérot mode, L03, was used to undertake a full and unbiased spectral survey over the wavelength range 47–197 μm as part of the Guaranteed Time program. In addition to this, many narrow Fabry-Pérot scans (L04) were carried out at specific wavelengths and several medium resolution grating measurements (L01) were undertaken with various different pointings. These provide an extensive dataset in the archive for this important bright source.

The large dataset of Fabry-Pérot measurements has been used to investigate and improve calibration procedures and files for the LWS L03 mode. During each Fabry-Pérot observation, the instrument settings were optimised for a single detector only (the 'prime' detector). Using improved calibration procedures, data from the other nine LWS detectors can now also be calibrated and used to improve the signal to noise and reliability of prime data.

These new data have allowed us to search for faint lines in the dataset and examine line shapes with much higher signal to noise. Results from this program so far include the modelling of atomic fine structure lines towards the source, observation of faint emission due to the HD $J = 1 \rightarrow 0$ rotational line leading to an estimate of the deuterium abundance, and observation of OH lines containing the three stable isotopes of oxygen.

Key words: ISO LWS – : L03 data, Sgr B2

1. INTRODUCTION

Several wide spectral surveys were carried out with the ISO Long Wavelength Spectrometer (LWS; Clegg et al. 1996) using its Fabry-Pérot (FP) mode, L03. These were very time consuming and so were conducted towards bright sources in order to obtain a high signal to noise in a reasonable integration time. Even so, only two sources were covered across the full LWS wavelength range; Sagittarius B2 (Sgr B2) and Jupiter.

During each L03 observation, the LWS FP and grating settings were optimised for the detector whose band-pass filter included the wavelength range of interest. This was designated as the 'prime' detector. However, all ten LWS detectors recorded data simultaneously in their own spectral ranges. The other nine detectors are known as 'non-prime' and often recorded useful data that can complement the prime data (see Gry et al. 2002 for more details). In datasets with wide wavelength coverage, the quantity of useful non-prime data can be quite significant. This paper describes some of the results that have been achieved using non-prime data from the Sgr B2 dataset. The techniques developed for these data can be applied to other long L03 observations in the archive.

Sgr B2 is a giant molecular cloud complex, located $\sim$120pc from the Galactic Centre. The complex consists of three main clusters of compact HII regions and dense molecular cores aligned in a north-south direction. These are surrounded by a diffuse envelope. Their far-infrared spectrum is dominated by thermal continuum from dust with a peak near 80 μm. Many absorption lines are seen in the spectrum due to both the Sgr B2 envelope and clouds located along the line of sight.

2. OBSERVATIONS

Sgr B2 was observed in an unbiased spectral survey using the LWS Fabry-Pérot (FP) mode, L03. The entire wavelength range from 47 to 197 μm was covered using 36 separate observations with a spectral resolution of 30–40 km s^{-1}. These observations were carried out with each FP mini-scan repeated between 3 and 6 times. The total integration time used in the survey amounted to approximately 53.6 hours. In addition to these L03 observations, Sgr B2 was observed in many narrow L04 scans (23 observations) and medium resolution grating measurements (16 observations). The L04 measurements were generally made with a larger number of repeated FP scans than the L03 observations.

The L04 and grating measurements were made at many different pointings across the source. However, all observations forming the L03 spectral survey were carried out with the same pointing and orientation of the source in the LWS beam. The LWS was pointed slightly offset from the Sgr B2 (Middle) source in order to exclude the northern component from the beam.

These data were reduced using a version of the LWS Interactive Analysis (LIA) software that was updated to allow both prime and non-prime data to be processed (see Polehampton et al. 2002a).

Two FPs were used in the design of the LWS in order to maintain high spectral resolving power across the full LWS wavelength range. However, this was achieved with a cost to transmission at short wavelengths as the short wavelength FP

Proceedings of the Symposium *"Exploiting the ISO Data Archive - Infrared Astronomy in the Internet Age"*, 24–27 June 2002, Sigüenza, Spain (C. Gry, S. B. Peschke, J. Matagne et al. eds., ESA SP-511)

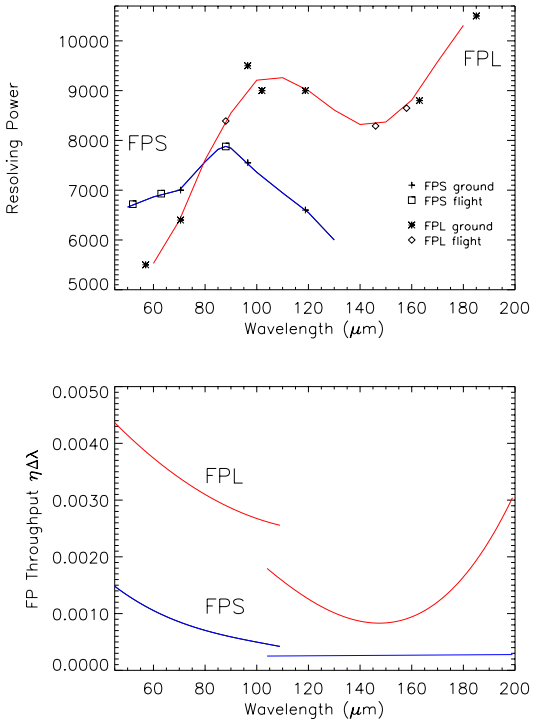

Figure 1. (a) Resolving power of FPS (blue) and FPL (red) from ground-based and in-flight measurements. (b) Total measured FP throughput for FPS and FPL, defined as the combination of FP efficiency and resolution element width.

(FPS) had a throughput approximately 3 times lower than the long wavelength FP (FPL). The nominal wavelength at which FPL replaced FPS was 70 μm. Fig. 1 shows the FP resolution (determined from ground and in-flight measurements) and the FP transmission (measured as FP throughput - a combination of transmission efficiency and response profile width).

During observations that used FPL, the short wavelength detectors were non-prime but still recorded data. In some cases the FP and grating responses were coincident at these wavelengths and the resulting data are useful. This has allowed the spectral region covered by FPS to be recovered from FPL data with a corresponding increase in signal to noise. In general the spectral resolution was lower in these non-prime data with values $\sim$ 50–60 km s^{-1}. Fig. 3 shows the range 47–60 μm with the prime data recorded using FPS in green and the non-prime FPL data in black. This spectral region was stitched together from 103 fragments of non-prime data and so is more trustworthy over narrow ranges than for wide spectral shape (several of the wide spectral features may not be real). Fig. 2 shows a particular example of the gain in signal to noise for the OH 53 μm line. The increase in signal to noise achievable by using non-prime data below 70 μm is generally a factor of 5–8.

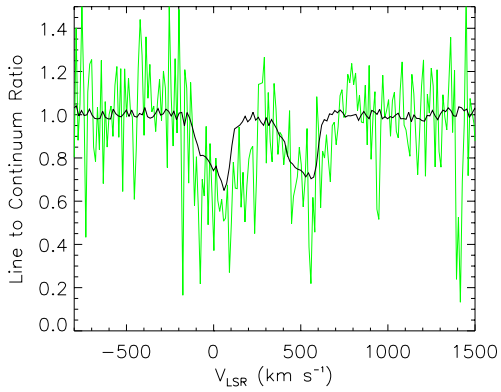

Figure 2. The OH lines at 53.26 μm from prime data (green) and after the co-addition of 4 independent non-prime observations. Both datasets were binned at 1/4 spectral resolution element.

3. RESULTS

The main lines that appear in the spectral range of the survey are low lying rotational transitions of simple molecules (e.g. OH, CH, H_2O, NH_3) and these generally show absorption due to the envelope of Sgr B2 and in some cases due to the line of sight clouds. There are also emission lines from forbidden spin-transitions of atoms and ions (e.g. OI, CII, NIII, OIII) and transitions due to the bending modes of chain molecules such as C_3 (see Cernicharo et al. 2000). Some of these lines have been previously observed towards Sgr B2 with lower spectral resolution using the KAO (e.g. OH; Storey et al. 1981) but most were observed for the first time with ISO. Many of the features were also observed in the L04 observations (see Goicoechea & Cernicharo 2002a). However, the L03 survey has many advantages over these narrow scans. The wide spectral coverage means that the continuum level around spectral features can be determined with much higher confidence, allowing weak line of sight features to be identified. The full wavelength coverage also gives the opportunity to check for all transitions of a particular species within the LWS range. Furthermore, it allows the discovery of new and unexpected features. In total $\sim$ 80 lines in the survey have been assigned to known transitions and there are many weaker features with no assignment.

The first results of the survey on NH_3 lines were recently reported by Ceccarelli et al. 2002. This species had the largest number of detected lines in the survey. In total there were 21 absorption lines identified across the LWS spectral range. The large number of detected lines allowed the properties of the absorbing region to be accurately constrained and it was found that the absorption occurred in a hot layer in front of the source.

Several examples of the results from the survey using non-prime data are described in the following sections.

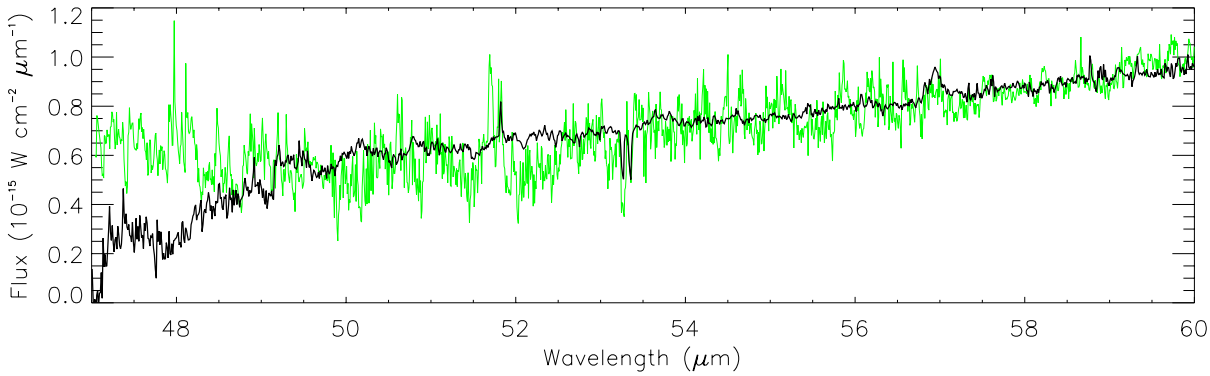

Figure 3. Prime data in the region 47–60 μm are shown in green with the recovered non-prime data from detector SW2 shown in black.

3.1. Atomic Oxygen

A good example of the improvement achievable by using non-prime data is the atomic oxygen line at 63 μm. This line occurs in absorption due to clouds along the line of sight to Sgr B2. It was observed in the L03 survey in both prime data using FPS and non-prime data using FPL. It was also covered in several L04 observations. In order to minimise instrumental errors in these observations, the continuum was fitted with a polynomial that was then divided into the data. This effectively bypassed the multiplicative calibration errors that are large for LWS FP data. The remaining uncertainty is due to the dark current, polynomial fit and random error in photocurrent. The final uncertainty is smallest in the L03 non-prime data due to the increase in signal to noise by using FPL, the wide coverage of continuum (allowing an accurate continuum fit) and the use of accurate dark values that included stray light. These were determined using an algorithm that examined instances of zero transmission in non-prime data (see Polehampton et al. 2002a).

The resulting improvement in the line shape allowed detailed modelling of the absorption due to the line of sight clouds. This was used to separate the various cloud layers and determine the OI/CO ratio in their cores. The results imply that $\sim$ 70% of oxygen is in atomic form and not locked into CO - the results are discussed in detail by Vastel et al. (2002).

3.2. Deuterium

The two lowest energy rotational transitions of the HD molecule occur within the LWS range. The improvements in data reduction and calibration developed for the Sgr B2 dataset allowed the $J = 1 \rightarrow 0$ transition at 112 μm to be detected in emission. This line appeared in two independent L03 observations, one of which was recorded on a non-prime detector. Co-addition of these increased the signal to noise sufficiently to detect the line with a confidence of more than 3σ. This is only the third time that this line has been detected in the ISM outside of the Solar System.

In order to determine the excitation of the molecule, the $J = 2 \rightarrow 1$ transition at 56 μm was examined. The region around this line was covered by a non-prime detector in three observations that used FPL. The line was not detected in the co-added data. However, the increase in signal to noise obtained by using the FPL data allowed a useful upper limit to be placed on emission at this wavelength. The equivalent prime data, recorded with FPS, gave an upper limit 6 times higher. Assuming LTE, an upper limit to the temperature in the emission region is $T_{\rm gas} > 80$ K, indicating that the emission originated in the warm envelope of Sgr B2. The corresponding column density of H_2 was estimated from dust observations, leading to a deuterium abundance in the Sgr B2 envelope of D/H=(0.2–11)$\times 10^{-6}$ (see Polehampton et al. 2002b).

3.3. OH

Many rotational transitions of OH occur across the LWS spectral range. The ground state lines appear in absorption due to both Sgr B2 itself and clouds along the line of sight. Higher rotational transitions of ^{16}OH are also observed but these only occur at the velocity of Sgr B2 itself (see Goicoechea & Cernicharo 2002b). The ground state rotational transition in the $^2\Pi_{3/2}$ ladder appears in the spectral survey in absorption for the three isopotomers, ^{16}OH, ^{17}OH and ^{18}OH. In the case of ^{17}OH this is the first detection of its rotational lines in the ISM (Polehampton et al. in prep.).

The increase in signal to noise obtained by co-adding non-prime data has allowed the line shapes to be accurately modelled. Comparison of the different isopotomers can then be used to determine the variation in oxygen isotope ratio in the line of sight clouds. Fig. 4 shows a fit to the ^{18}OH line that accounting for the line of sight clouds at velocities -100 to $+30$ km s^{-1}. These are generally associated with the galactic spiral arms between the Sun and Galactic Centre (see Greaves & Williams 1994).

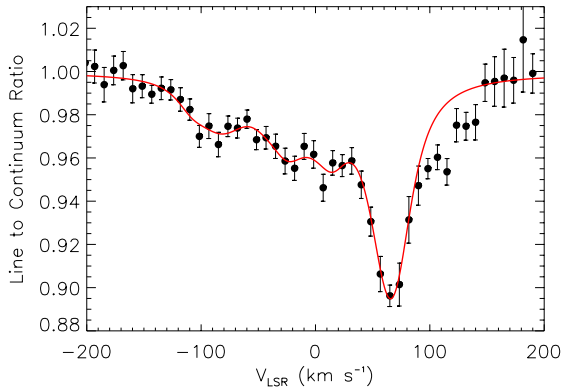

Figure 4. Co-added L03 data from the two Λ-doublet components of the ^{18}OH $J = 5/2 \leftarrow 3/2$ transition. The data were binned at 1/4 resolution element and the errors represent the combined statistical and systematic uncertainty in each bin. The best fit model accounting for absorbing clouds in the line of sight is shown.

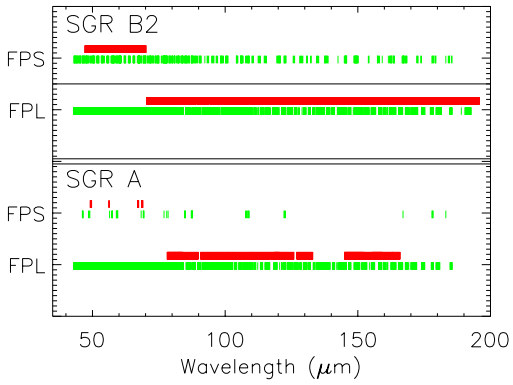

Figure 5. Wavelengths covered by useful prime (red) and non-prime data (green) for two L03 datasets. Full wavelength coverage was achieved in the prime data for Sgr B2 but Sgr A was not observed over the full wavelength range. These gaps can be filled using the non-prime data.

Table 1. Other long L03 datasets in the ISO archive

Orion	26 Observations
Sgr A	25 Observations
Jupiter	25 Observations
Saturn	22 Observations

4. APPLICATIONS TO OTHER DATASETS

Non-prime data are not only useful for increasing the signal to noise in the prime data but can also be used to extend the wavelength coverage, check uncertain features and improve the calibration. Several other objects were observed with the L03 mode but full coverage of the LWS wavelength range was not completed. In this case non-prime data can fill in some of the gaps in the spectrum. An algorithm has been developed to search L03 datasets for useful data. An example of the results are shown in Fig. 5. Prime data are shown in red. In the case of Sgr A, the full spectral range was not covered. However, useful non-prime data can significantly extend the wavelength range as shown in green. These data can be calibrated and reduced in the same way as prime data with the latest version of the LWS Interactive Analysis software (LIA 10). Table 1 shows several of the other long L03 datasets that exist in the ISO archive.

REFERENCES

Ceccarelli, C., Baluteau, J.-P., Walmsley, M., et al., 2002, A&A, 383, 603

Cernicharo, J., Goicoechea, J. R. & Caux, E., 2000, ApJ, 534, L199

Clegg, P. E., Ade, P. A. R., Armand, C., et al., 1996, A&A, 315, L38

Goicoechea, J. R. & Cernicharo, J., 2002a, this volume

Goicoechea, J. R. & Cernicharo, J., 2002b, ApJ, 576, L77

Greaves, J. S. & Williams, P. G., 1994, A&A, 290, 259

Gry, C., Swinyard, B., Harwood, A., et al., 2002, ISO Handbook Volume III (LWS), Version 2.0, ESA SAI-99-077/Dc

Storey, J. W. V., Watson, D. M. & Townes, C. H., 1981, ApJ, 244, L27

Polehampton, E. T., Swinyard, B. M., Sidher, S. D. & Baluteau, J.-P., 2002a, in The Calibration Legacy of the ISO Mission, ESA SP-481, in press

Polehampton, E. T., Baluteau, J.-P., Cecarrelli, C., Swinyard, B. M. & Caux, E., 2002b, A&A, 388, L44

Vastel, C., Polehampton, E. T., Baluteau, J.-P., et al., 2002, ApJ, in press, [astro-ph/0208193] (see also Vastel et al., this volume)

DIFFUSE GAS IN THE GALAXY: THE GALACTIC PLANE

Jean-Paul Baluteau[1], Fredéric Damour[1,2], Emmanuel Caux[3], Cécile Gry[4,1] and Cecilia Ceccarelli[5,6]

[1]LAM CNRS-UP, BP8, 13376 Marseille Cedex 12, France
[2]IRAM, Avenida Divina Pastora 7, Núcleo Central, 18012 Granada, Spain
[3]CESR CNRS-UPS, BP4346, 31028 Toulouse Cedex 04, France
[4]ISO Data Centre, European Space Agency, Villafranca del Castillo, PO Box 50727, 28080 Madrid, Spain
[5]Observatoire de Bordeaux, BP89, 33270 Floirac, France
[6]LAOG, BP53, 38041 Grenoble Cedex 09, France

ABSTRACT

Preliminary results are reported from an ISO Active Archive Phase Project dedicated to the study of diffuse gas in the Galaxy. We use LWS observations of galactic lines of sight devoid of any known energetic sources. The LWS observations cover the far-infrared dust continuum emission and the major cooling fine-structure lines of the diffuse interstellar medium, i.e. [OI] 63 and 145 μm, [CII] 158 μm and [NII] 122 μm. Results from a sample of 144 lines of sight in the galactic plane are presented. The four main cooling lines prove to be well correlated with the dust continuum emission over four orders of magnitude in the FIR emission. Preliminary interpretations of these results are given together with the main perspectives of the study.

Key words: ISM: diffuse emission - ISM: photodissociation regions - ISM: far-infrared interstellar lines

1. INTRODUCTION

This work is part of an ISO Active Archive Phase Project which will produce close to 500 homogeneously reduced spectra, as well as comprehensive flux tables. The products will be re-ingested in the ISO Data Archive as Expert Reduced Data (XRD) and will thus be directly usable.

An inspection of the list of all LWS (Long Wavelength Spectrometer, Clegg et al. 1996) observations obtained in the L01 mode during the ISO Operations Phase shows that there are about 500 observations of galactic lines of sight devoid of any known energetic source. The LWS observations cover a large part of the dust emission continuum in the far-infrared (47 to 196 μm) and the major cooling fine-structure lines of the diffuse interstellar medium, i.e. [OI] 63 and 145 μm, [CII] 158 μm and [NII] 122 μm. These observations thus represent an ideal opportunity to study simultaneously the gas and dust properties in the diffuse medium.

Previous observations, made at low spatial resolution (7° for FIRAS/COBE, Bennett et al. 1994 and Fixsen et al. 1999; and 15′ for BICE, Nakagawa et al. 1995 and Nakagawa et al. 1998), already provided indications for a clear correlation of the [CII] line flux with the FIR emission, with an apparent change of behaviour between the Galactic Centre region and the other parts of the Galactic Plane. These studies can be refined with the much smaller field of view of the LWS (about 80″; Gry et al. 2002, hereafter LWS Handbook). First results from a selection of 144 lines of sight in the Galactic Plane are presented here.

2. OBSERVATIONS AND DATA REDUCTION

A set of 144 galactic lines of sight (LoS), restricted to latitudes less than 10°, has been selected among the LWS L01 observations in the ISO Data Archive. The distribution of the lines of sight in both longitude and flux is illustrated in Fig. 1, plotting the 100 μm continuum emission versus longitude for all LoS in the sample. This set is divided in three sub-samples.

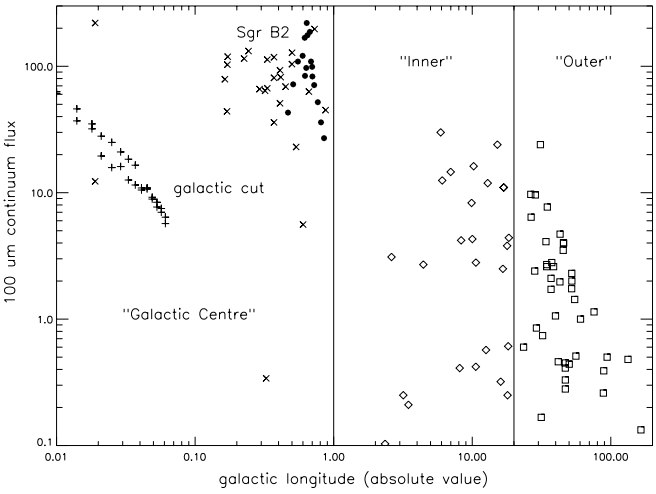

Figure 1. 100 μm continuum flux (in 10^{-18} W cm$^{-2}\mu$m^{-1}) versus galactic longitude for the 144 lines of sight of our sample. See text below for further precisions on the symbols.

The "Galactic Centre" sub-sample includes LoS located within 1° of the Galactic Centre: 32 LoS from a "galactic cut" are marked with "+" symbols, 17 LoS covering the diffuse part of the Sgr B2 region with filled circles and 28 others with "x" symbols. The "Inner Galaxy" sub-sample includes 26 LoS with $1° < |l| < 20°$ (diamond symbols) and the "Outer Galaxy" sub-sample 41 LoS with $|l| > 20°$ (open squares).

The LWS observations, extracted from the ISO Data Archive, have been processed and calibrated by the LWS pipeline version 10. Detailed description of the LWS instru-

Proceedings of the Symposium *"Exploiting the ISO Data Archive - Infrared Astronomy in the Internet Age"*, 24–27 June 2002, Sigüenza, Spain (C. Gry, S. B. Peschke, J. Matagne et al. eds., ESA SP-511)

ment and its wavelength and flux calibrations can be found in Swinyard et al. (1998) and in the LWS Handbook.

Futher analysis has been performed with the last version of the ISO Spectroscopy Analysis Package (ISAP version 2.1). This included removing remaining glitches, averaging the different scans, defringing, and measuring line fluxes and continuum emission.

3. DUST COLOR TEMPERATURE

To determine the dust color temperature, the continuum emission has been measured in each LoS at three wavelengths, namely 62.5, 100 and 160 μm. The resulting two continuum emission ratios are plotted in Fig. 2.

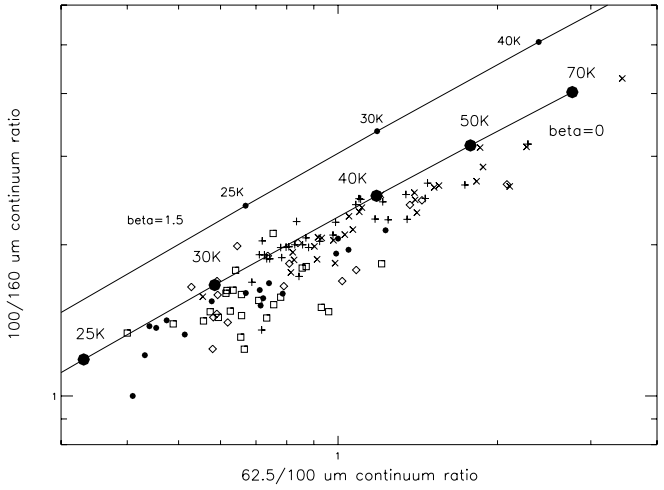

Figure 2. Plot of the 100/160 μm continuum ratio against the 62.5/100 μm continuum ratio for all lines of sight in our sample. Symbols are as in Fig. 1. Tracks giving grey body temperatures for β = 0 and 1.5 are indicated in the figure. The apparent unphysical shift of the data to the right of the beta = 0 track is probably due to the contribution to the 62.5μm flux of stochastically heated small dust grains.

Two theoretical lines are also plotted, showing the expected ratio for a unique temperature grey body with an emissivity varying as $\lambda^{-\beta}$. No extended source correction was performed because applying the correction factors given in the LWS Handbook does not change the plot significantly.

As expected the data points are in line, parallel to the theoretical tracks but they seem to be shifted to an unphysical negative value of the emissivity coefficient. However this can be attributed to the contribution of small, thermally fluctuating dust grains. Sodrosky et al. (1994) found that stochastically heated dust grains contribute significantly to the emission in the 60 μm IRAS band: The average value of this contribution is 40% in the inner Galaxy and 60% in the outer Galaxy. Conversely they do not contribute significantly to the 100 μm and 160 μm emission. This extra contribution to the 62.5 μm fluxes thus causes all points to be systematically shifted to the right in Fig. 2.

Because of this effect the color-color diagram does not allow to derive simultaneously and independently the temperature and the emissivity coefficient of the dust. Dust temperatures can be derived from the 100μm/160μm color ratio alone, by fixing the emissivity coefficient. This will be presented in a subsequent paper.

4. ATOMIC FINE STRUCTURE LINES

Fluxes in the main cooling lines, [OI] 63 and 145 μm, [CII] 158 μ m and [NII] 122 μm, have been measured and plotted versus the continuum emission at 100 μm in Fig. 3.

For the [OI] 145 μm line, two independent measures are available as the line is observed on two LWS detectors (LW3 and LW4). Unfortunately the fluxes derived on the two detectors differ by quite a large factor (generally a factor of 2 to 4). These differences evidence a problem in the line flux calibration which is presently under investigation. For the present paper we have used the measurements made on detector LW3.

Fig. 3 evidences a clear correlation between line intensities and continuum emission for the four lines. Nevertheless the relationships have different power law indexes and correlation coefficients.

Linear fits of the log-log relationships (LogY = A + B $\times$ LogX) have been derived for the whole data set. Table 1 provides A, B (power law index) and R (Person's coefficient) for the four observed lines.

Table 1. Linear fit coefficients for the relationships of the four observed cooling lines with 100μm continuum emission. B is the power law index and R is the Person's correlation coefficient.

Line	A	B	R
[OI] 63 μm	-0.83	0.80	0.955
[OI] 145 μm	-2.00	0.92	0.950
[CII] 158 μm	-0.35	0.76	0.970
[NII] 122 μm	-1.47	1.04	0.970

The present study confirms the good correlation of the [CII] line with the continuum emission. Fig. 3 shows that for the faintest lines of sight (100 μm continuum flux density less than about 2 10^{-17} W cm^{-2} μm) the slope of the correlation (or power law index) is around unity, confirming previous findings (Bennett et al. 1994, Caux & Gry 1997, Nakagawa et al. 1998). Nevertheless, there is a break in the correlation and for the largest continuum emission lines of sight (corresponding to the "Galactic Center" samples) the power law index is significantly lower than 1.

The implications of the correlations of the four major cooling lines with the dust continuum emission, and of the different behaviour of the three subsamples will be discussed in a subsequent paper. In fact, study of the correlations with the total

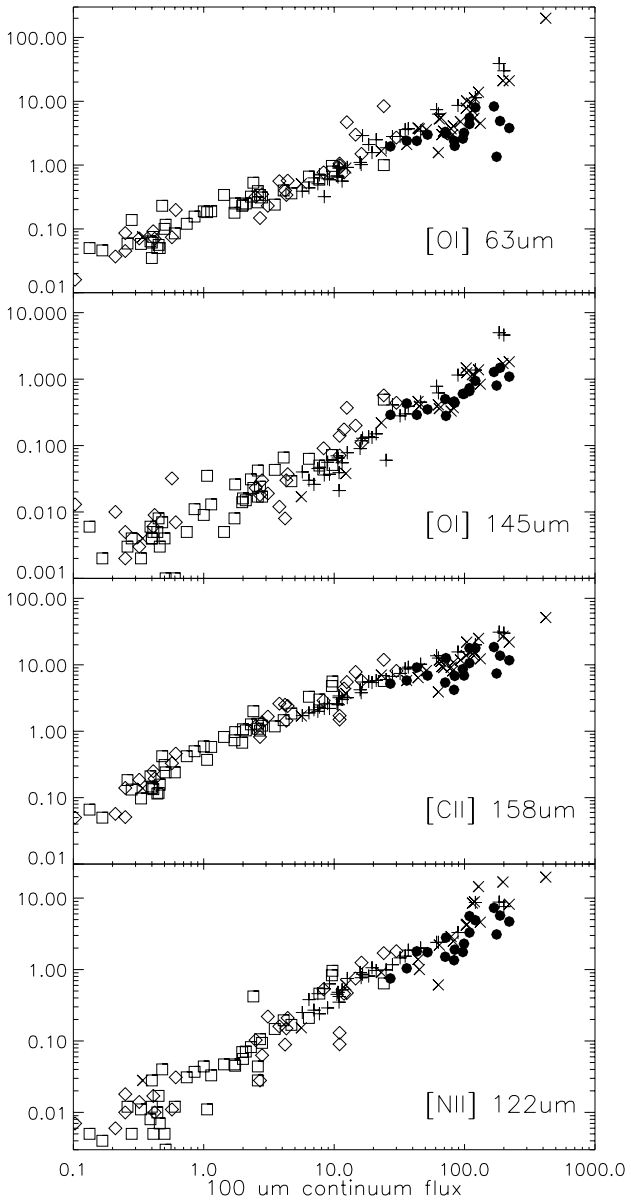

Figure 3. Fine-structure line intensities versus 100 μm continuum flux density (logarithmic scale) for the lines of sight of our sample. From top to bottom: [OI] 63 μm, [OI] 145 μm, [CII] 158 μm and [NII] 122 μm. Units are 10^{-18} $W cm^{-2}$ for line fluxes and 10^{-18} $W cm^{-2} \mu m^{-1}$ for the continuum emission. Symbols are as in Fig. 1.

FIR emission would be of more physical significance but requires that we first correct parts of the continuum emission for the contribution of stochastically heated small dust grains, as discussed in Section 3.

Fig. 4 shows the [OI] 145/63 μm line flux ratio plotted versus the continuum emission at 100 μm. The horizontal line at 0.07 indicates the upper limit for standard PDR model predictions, while the line at 0.1 corresponds to the expected ratio for a low density ionized medium. This figure suggests that in the largest FIR emission regions the [OI] 63 μm line is attenuated by a significant absorption from the cold atomic/molecular parts of the ISM. For the faintest FIR emission regions a significant fraction of the observed [OI] fluxes could be provided by the low density ionized medium along the line of sight.

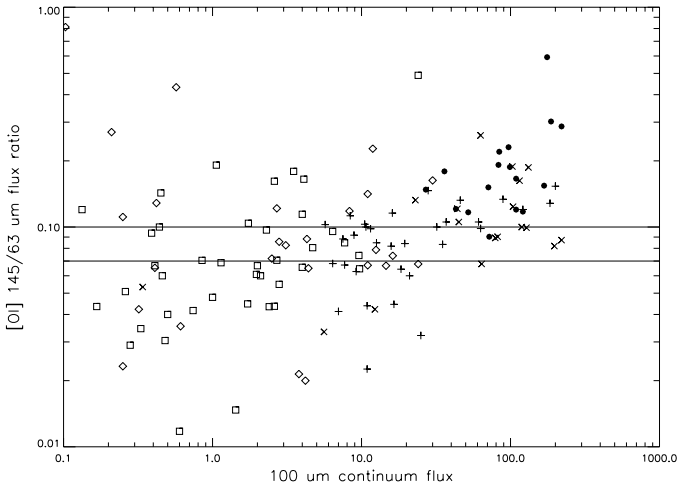

Figure 4. Plot of the [OI] 145/63 μm line flux ratio against the 100 μm continuum flux density for the lines of sight of our sample. Symbols are as in Fig. 1. The horizontal line at 0.07 indicates the upper limit for standard PDR model predictions, while the line at 0.1 corresponds to the expected ratio for a low density ionized medium.

5. CONCLUSIONS AND PERSPECTIVES

For the first time the analysis of four cooling lines together with the continuum emission of the interstellar medium is made possible, thanks to LWS observations. This provides a unique opportunity to disentangle the emission of the diffuse PDR regime from that of the diffuse ionized medium. We have presented preliminary results for a selection of galactic lines of sight. The next steps include reducing the whole sample of available lines of sight (about 500 LWS spectra for the diffuse medium), as well as investigating further the different contributions to the far infrared continuum emission and discussing its correlations with the fine structure line intensities. The interpretation of these data and the discussion of their astrophysical implications represent an ongoing project within the ISO Active Archive Phase.

REFERENCES

Bennett C.L., Fixsen D.J., Hinshaw G. et al., 1994, ApJ 434, 587
Caux E., Gry C., 1997, in: Proceedings of the ESA Symposium "The far infrared and submillimiter universe", ESA SP-401, 67
Clegg P.E., Ade P.A.R., Armand C. et al., 1996, A&A 315, L38
Fixsen D.J., Bennett C.L., Mather J.C., 1999, ApJ 526, 207
Gry C., Swinyard B.M., Harwood A. et al., 2002, The ISO Handbook Version 2.0 Vol. III: LWS, SAI/1999-077/Dc

Nakagawa T., Doi Y., Yui Y.Y. et al., 1995, ApJ 455, L35
Nakagawa T., Yui Y.Y., Doi Y. et al., 1998, ApJS 115, 259
Sodrosky T.J., Bennett C., Boggess N. et al., 1994, ApJ 428, 638
Swinyard B.M., Burgdorf M.J., Clegg P.E. et al., 1998, SPIE 3354, 888

THE ISO-LWS SPECTRUM OF SGR B2 REGION

Javier R. Goicoechea, José Cernicharo, and Juan Ramón Pardo

Instituto de Estructura de la Materia. Departamento Física Molecular, CSIC, Serrano 121, E–28006 Madrid, Spain.

ABSTRACT

In this contribution we present a brief summary of the detailed study we are carrying out of the far–IR spectrum of the Sgr B2 complex. This molecular cloud represents an interesting burst of massive star formation in the Galactic Center and may be representative of other active galactic nuclei. Our ∼50–190 μm Line Survey includes all the LWS–FP data base observations we are using in the analysis of the Sgr B2 M central condensation. We also present LWS–grating spectra covering a 9'×27' (∼25×70 pc) region around the central M source that completes our analysis of Sgr B2. The combination of both far–IR molecular spectroscopy and radiative transfer tools is giving us a more accurate picture of the warm gas in the outer layers of the complex. This warm gas is poorly traced by mm and submm observations.

Key words: infrared: ISM: lines and bands — ISM: individual (Sgr B2) — ISM: molecules — line: identification — molecular data — radiative transfer

1. INTRODUCTION

The Sagittarius B2 complex represents an interesting burst of massive star formation in the Galactic Center (GC) and may be representative of other active galactic nuclei. Large scale continuum maps from radio to far–IR wavelengths show that Sgr B2 is the brightest and among the most massive clouds of the GC. The Sgr B2 M source is the brightest far–IR condensation of the complex with a diameter of $\simeq 40''$ at 100 μm and has also the largest gas column density. Several studies have shown that the core is embedded in a extended and clumpy cloud of warm gas. However, the observed rich chemistry in the gas in front of Sgr B2 and its possible heating mechanisms are far from settled. Low velocity shocks have been invoked to explain the enhanced abundances of some species such as NH_2 or NH_3 (Flower et al. 1995) which are not observed in more quiescent regions. On the other hand, UV radiation can have an important effect on the gas in the outer layers. This radiation may be provided by evolved stars and by young massive stars in the envelope of Sgr B2 itself (Martín–Pintado et al. 1999). In addition, the emission of several ions with high excitation potential (such as [OIII] and [NIII]) is extended in the Sgr B2 region. Thus, a widespread ionized component producing photodissociated regions (PDRs) in the envelope is also possible.

Due to its high column density, $N(H_2) \simeq 10^{23-24}$ cm^{-2}, Sgr B2 is a very opaque source at optical but with high luminosities in far-IR, millimeter and radio wavelengths. Because of its physical and chemical complexity (clumped structure, extended envelope, hot cores, ultracompact HII regions, etc.) it is a unique object for spectroscopy studies and for the searching of new molecules. In this contribution we summarize the analysis of the region we are carrying out using the ISO-LWS spectra.

2. THE ISO-LWS FABRY–PÉROT SPECTRUM

The far–IR spectrum is characterized by forbidden emission lines of atoms and ions of the PDRs and HII regions of the complex and by molecular lines in absorption against the continuum emission of dust. These features come from the warm outer envelope of Sgr B2 and from the foreground gas along the line of sight ("spiral arms clouds"). Molecular features includes several **rotational lines** of Oxygen–bearing species such as H_2O, $H_2{}^{18}O$, OH, ^{18}OH, and H_3O^+; Nitrogen--bearing molecules such as NH, NH_2, and NH_3; and other diatomic species such as HF or CH. Low energy **bending modes** of non–polar carbon chain radicals such as C_3 have been also observed. Tetra–atomic carbon, C_4, have been tentatively detected for the first time in Sgr B2 and some C–rich evolved stars. The list of detected molecules still grows up (see contribution by Polehampton for HD and ^{17}OH detections) and several weak lines remain unidentified. Atomic and ionic features include **fine structure lines** of [OI], [OIII], [CII], etc.
Extended emission/absorption of some of these species have been also observed in the ISO-LWS grating raster maps at much lower resolution (∼1000 Km s^{-1}).

Many works have been done and others are under study in the analysis of the LWS-FP spectra (see Fig. 1) to fully characterize the outer layers of Sgr B2. Some studies include: H_2O and $H_2{}^{18}O$ (Cernicharo et al. 1997, 2002), [OI] (Baluteau et al. 1997, Lis et al. 2001), HF (Neufeld et al. 1997), C_3 and NH (Cernicharo, Goicoechea & Caux 2000), H_3O^+ (Goicoechea & Cernicharo 2001a), NH_2 (Goicoechea & Cernicharo 2001b), NH_3 (Ceccarelli et al. 2002), HD (Polehampton et al. 2002), OH and ^{18}OH (Goicoechea & Cernicharo 2002).

3. FAR-INFRARED OH FLUORESCENT EMISSION

In any of the PDR vs. Shock scenarios or in a combination of both, O–bearing species such as H_2O, OH, H_3O^+ and atomic

Proceedings of the Symposium *"Exploiting the ISO Data Archive - Infrared Astronomy in the Internet Age"*, 24–27 June 2002, Sigüenza, Spain (C. Gry, S. B. Peschke, J. Matagne et al. eds., ESA SP-511)

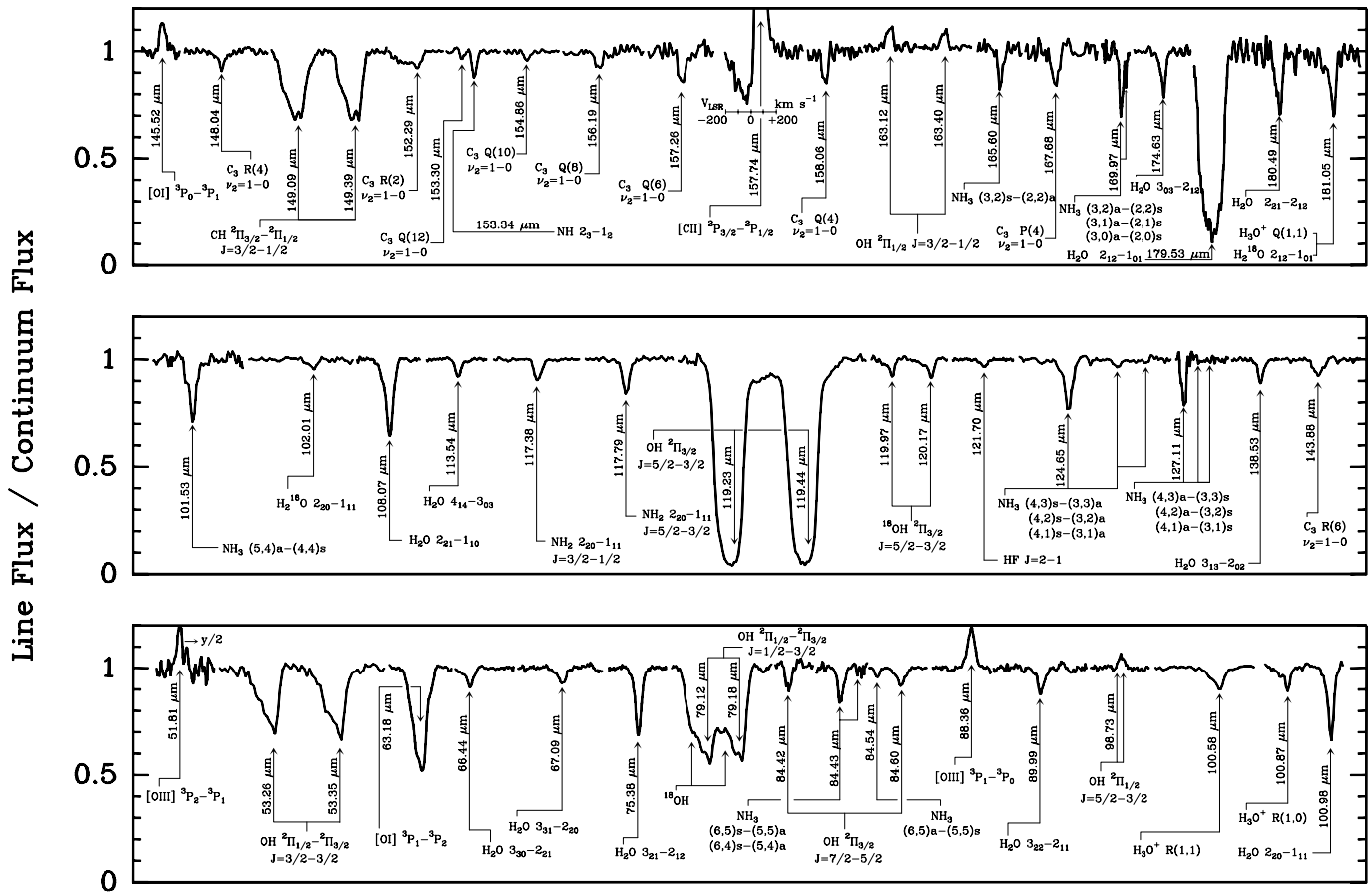

Figure 1. Far–IR spectrum of Sgr B2 with a spectral resolution of ∼35 km s^{-1} taken with the ISO-LWS Fabry-Pérot. This figure only shows the most representative lines we are working on (see references). Different pipeline products have been processed and compared from 1998 to 2002 (OLP 7.01 to OLP 10.1). Note the discontinuity of the spectrum after each line.

oxygen are decisive for the thermal balance of the dense molecular gas. In particular, the hydroxyl radical, OH, has been predicted to be abundant in both scenarios.

Most of the pure rotational lines of OH radical are in the far–IR coverage of the LWS spectrometer. We have detected several ^{16}OH and ^{18}OH Λ–doublets involving levels up to 420 K. All rotational doublets connecting the ^{16}OH $^2\Pi_{3/2}$ ground–state with the rotational levels of the $^2\Pi_{1/2}$ ladder (∼34, 53, 79 and 119 μm) are observed in absorption while the ^{16}OH $^2\Pi_{1/2}$ intra-ladder rotational transitions at ∼98 and ∼163 μm are observed in emission. According to the chemical models, the major contribution to the enhanced OH comes from regions where water vapor is being rapidly photodissociated and/or in shocked regions. The innermost regions of the Sgr B2 will be completely hidden in the mid and far-IR due to the large dust opacity. Almost all the observed OH absorption/emission will come from the external layers of the Sgr B2 cloud and from the cold dark clouds and diffuse gas in the line of sight. Before ISO, only the fundamental rotational Λ–doublet (∼119 μm) had been detected. Each line is so optically thick that absorbs completely the continuum avoiding any check with the models. Another problem arises as the lower excitation lines have negative velocity absorptions associated with the foreground gas in the line of sight and not related with Sgr B2 itself. The detection of several OH intra– and cross–ladder lines allows to separate both components and to constrain some important physical parameters.

3.1. Modeling the OH envelope

In order to estimate the OH abundance and the physical conditions leading to the observed OH line emission in the $V_{LSR} \simeq +50$ km s^{-1} component, we have modeled the first 20 OH rotational levels using a non–local radiative transfer code (Goicoechea & Cernicharo 2002). We have adopted a spherical geometry for a cloud consisting of two components with a total size of 42″: a uniform CORE with a diameter of 25″ and a SHELL of variable thickness and distance to the core (see Fig. 2). These observations put some constraints on the size and density of the shell. We found that the OH absorption/emission must arise in a shell around the M core not resolved by the LWS beam. The gas density in the shell is moderate, with upper limits of 10^4 cm^{-3} and temperatures of ≃300 K.

The OH abundance is high, (2–5)×10^{-6}. The LWS/FP data

suggest an OH/H_2O abundance ratio of 0.1–1. This is larger than the value predicted in shock models and in dense dark cores models for the same region.

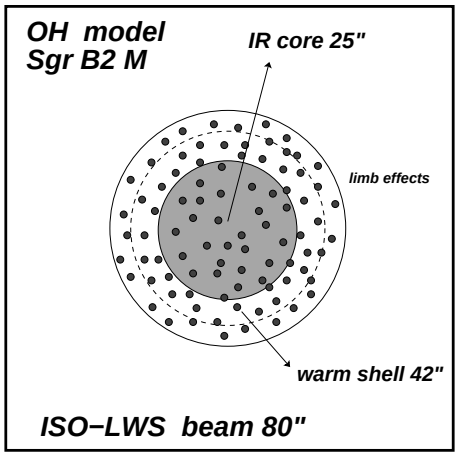

Figure 2. Sketch of the OH model for Sgr B2 M. The square box represents the ISO-LWS field of view for the Fabry–Pérot.

The large abundance found in Sgr B2 suggests that its external shells are illuminated by a strong UV field producing a PDR, although low velocity shocks, unresolved by the ISO data, may be also present. Many species formed during the evolution of the cold gas in Sgr B2 are being now reprocessed in these regions. This warm gas is poorly traced by millimeter and submillimeter observations, but it represents the strongest contribution to the absorption/emission features in the far–IR spectrum of Sgr B2. In addition to ^{16}OH and ^{18}OH, we have searched for several related species such as OH^+ or H_2O^+. No lines from these species have been found.

4. THE ISO-LWS GRATING MAPS

Extended emission/absorption of some of the species presented in Fig. 1 have been observed in the 9'×27' grating raster maps at much lower resolution (see Fig. 3).

From the molecular point of view, main detected features are related to ground state lines of light hydrides such as H_2O, OH or CH. These lines are observed in absorption against the continuum dust emission in almost all positions of the map. However, according to the grating resolution it is difficult to discriminate which components along the line of sight, or Sgr B2 itself, are producing the observed absorptions.

Nevertheless, the spectral resolution could be enough to detect other molecular features by the low energy bending modes of molecular carbon chains. Cernicharo et al. (2002) have reported the detection of a new infrared band (at 57.5 μm) in the ISM (Sgr B2 M and N) and in carbon–rich evolved stars that they tentatively assign to C_4. An alternative carrier might be C_4H.

On the other hand, the ionized gas of the region is clearly shown as several ionic lines are detected in several positions.

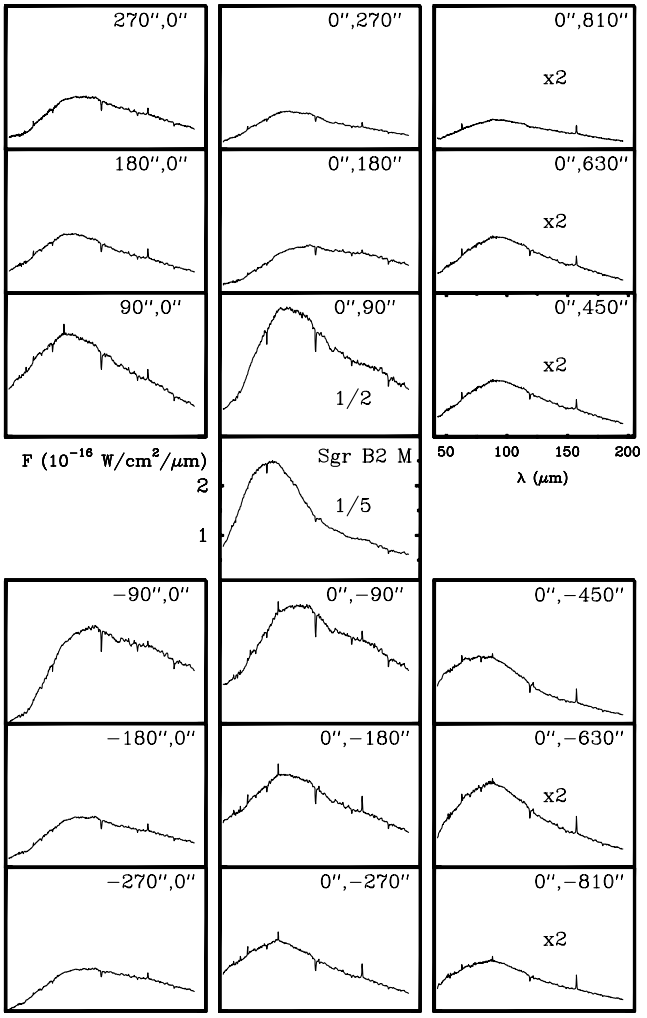

Figure 3. ISO-LWS raster of Sgr B2 complex centered at the M condensation (0",0"). Offsets, in arcseconds, are indicated in each box. A continuum normalized flux spectrum of Sgr B2 M and its adjacent easter position is shown in Fig. 4.

Identifications include: [OI], [CII], [NII], [NIII] and [OIII]. These emission comes from the associated PDR and HII regions of the complex, and may trace different environments from one point to other (see differences between (0",0") and (90",0") positions in Fig. 4).

In the case of Sgr B2 region, the emission from dust can only be observed a wavelengths longer than 50 μm due to the low temperatures of the dust grains. UV photons coming from evolved and newly born massive stars heat the grains and are re–emitted as Far–IR continuum. The different shapes of the dust emission shown in Fig. 3 prove the different H_2 column densities across the map, 10^{23} to 10^{24} cm^{-2} depending of the position, while the dust temperatures are in the range 22–32 K.

5. HIDDEN FAR–IR CO EMISSION

The presence of warm gas in the outer layers of Sgr B2 might be expected to radiate in high–J CO lines. The CO J=14-13

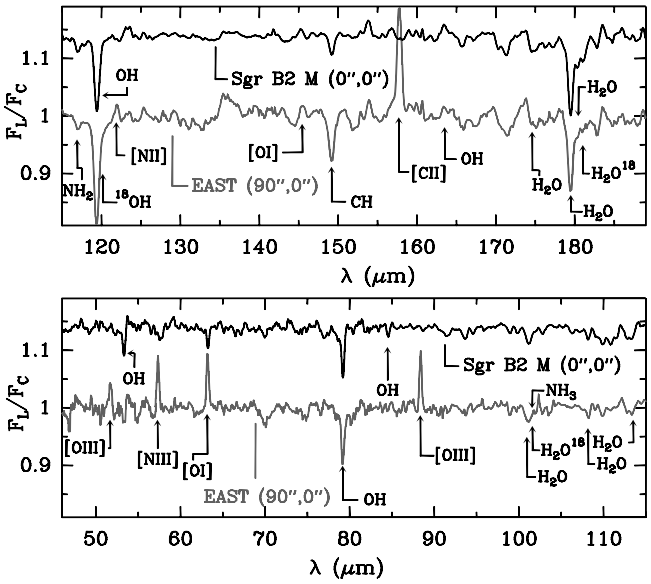

Figure 4. ISO-LWS grating observations of Sgr B2 M (0",0") and (90",0") positions. The intensity scale correspond to the continuum normalized flux. Main features are labelled.

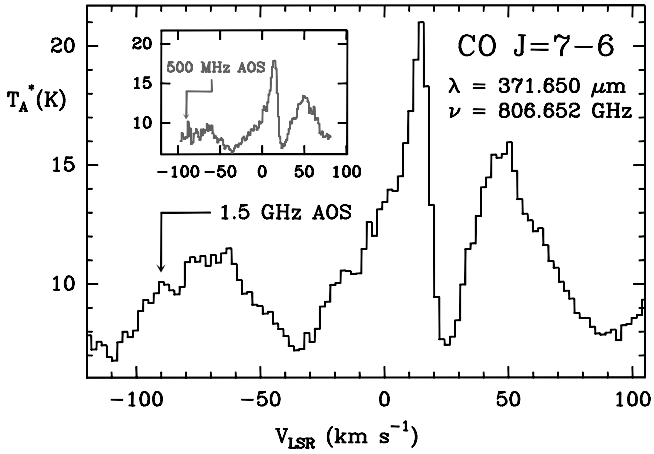

Figure 5. Caltech Submillimeter Observatory (CSO) observations of the CO J=7–6 line at 371.650 μm (806.652 GHz).

line at 185.999 μm is the lowest energy level ($E_l \simeq 500$ K) observable with ISO–LWS detctors. However, we have NOT DETECTED any emission/absorption from CO in the ISO–LWS spectra of Sgr B2 region. We have run several radiative transfer models and derived that densities $< 10^4$ cm^{-3} and kinetic temperatures < 300 K are needed to explain the lack of high–J CO lines.

Nevertheless, the excited CO could be traced with intermediate lines such as the J=7-6 line ($E_l \simeq 150$ K) at 371.650 μm. Fig. 5 shows the J=7-6 CO line observed toward Sgr B2 M with the CSO telescope. The line exhibits a complex profile. The gas related to Sgr B2 shows a strong self–absorption with two emission peaks at $\simeq$+15 and +50 kms^{-1}. The warm gas within 1 kpc of the Galactic Center is present at more negative velocities.

The future far–IR instruments on board next generation telescopes such as the *Herschel Space Observatory* will allow a fast mapping of several rotational lines of different species in galactic and extragalactic sources making light hydrides such as OH or H_2O very useful tools in deriving the physical properties of warm clouds like the external shells of Sgr B2. Understanding clouds like Sgr B2, the prototype of giant molecular clouds in our GC, could help in the analysis of the molecular clouds in starburst galaxies such as Arp 220.

ACKNOWLEDGEMENTS

We thank Spanish DGES and PNIE for funding support under grant ESP98–1351–E and PANAYA2000-1784. JRG acknowledges *UAM* for a pre–doctoral fellowship.

REFERENCES

Baluteau, J.P, Cox., P., Cernicharo, J., et al. 1997, A&A, 322, L33
Ceccarelli, C. et al. 2002, A&A, 383, 603
Cernicharo, J., Lim, T., Cox, P., et al. 1997, A&A, 323, L25
Cernicharo, J., Goicoechea, J.R., & Caux, E. 2000, ApJ, 534, L199
Cernicharo, J., Goicoechea, J.R., & Benilan, Y. 2002, ApJ, submitted
Flower, D.R., Pineau des Forêts & M.C. Walmsley, 1995, 294, 815
Goicoechea, J.R., & Cernicharo, J. 2001a, ApJ, 554, L213
Goicoechea, J.R., & Cernicharo, J. 2001b, The Promise of the Herschel Space Observatory. Eds. G.L. Pilbratt, J. Cernicharo, A.M. Heras, T. Prusti, & R. Harris. ESA-SP 460, p.413
Goicoechea, J.R., & Cernicharo, J. 2002, ApJ, accepted
Lis, D.C, Keene, J., Phillips, T.G., Schilke, P., Werner, M., W. & Zmuidzinas, J. 2001, ApJ, 561, 823
Martín–Pintado, J., Gaume, R.A., Rodíguez–Fernández, N., de Vicente, P., & Wilson, T.L. 1999, ApJ, 519, 667
Neufeld, D.A., Zmuidzinas, J., Schilke, P. & Phillips, T.G. 1997, ApJ, 488, L141.
Polehampton, E. T., Baluteau, J.P., Ceccarelli, C., Swinyard, B. M., Caux, E. 2002 A&A, 388, L44-L47

ISO SPECTROSCOPY OF SHARPLESS 171

Yoko Okada[1], **Takashi Onaka**[1], **Hiroshi Shibai**[2], **and Yasuo Doi**[3]

[1]Department of Astronomy, School of Science, University of Tokyo, Tokyo 113-0033, Japan
[2]Graduate School of Science, Nagoya University, Nagoya 464-8602, Japan
[3]Department of Earth Science and Astronomy, University of Tokyo, Tokyo 153-8902, Japan

ABSTRACT

We report the results of far-infrared observations (3–190 μm) of Sharpless 171 (S171) with the spectrometers on board the Infrared Space Observatory (ISO). Based on the observed intensities of forbidden lines and continuum emission, we derive the physical properties of the observed region, such as the temperature, density, and elemental abundance. The observed line and continuum intensities are in agreement with photodissociation region (PDR) models in most observed positions except for the molecular region, where the [OI] 63 μm to 146 μm ratio is too small (~ 5) compared to the predictions of existing PDR models. We conclude that the absorption by oxygen atoms in foreground cool clouds is the most likely cause. [SiII] 35 μm line emission is quite strong over the observed region and the [SiII] 35 μm to [NII] 122 μm ratio indicates that Si in the gas phase is about 25% of the solar abundance in the diffuse ionized gas. This value is by an order of magnitudes larger than that in typical interstellar diffuse clouds, suggesting the dust destruction occurring in the ionized region.

Key words: Infrared: ISM: lines and bands – HII regions – PDR – ISM: individual objects: Sharpless 171

1. INTRODUCTION

Far-infrared spectroscopy of the interstellar medium (ISM) provides us a great deal of information on the nature of the ISM. In the interface region between the ionized and molecular regions, the intense far-ultraviolet (FUV)(6 eV $< h\nu <$ 13.6 eV) fluxes generally photodissociate molecules and photoionize heavy elements with ionization potentials less than the Lyman limit. Most energy is emitted in the far-infrared lines and continuum emission in the region. This region is called the photodissociation region (PDR) and theoretical models have been investigated for various conditions of PDRs (see Hollenbach & Tielens 1997 for a review). These models take account of chemistry and heat balance and give us cooling line intensities from PDRs.

In this paper, we report part of the results of a spectroscopic investigation of Sharpless 171 (S171) with the Infrared Space Observatory (ISO; Kessler et al. 1996). S171 is a large HII region, where the star cluster Be 59 is located at the central portion of the nebulous region. Be 59 contains one O7 star and several later-type stars, ionizing the gas around it. Yang & Fukui (1992) have mapped the large-scale molecular gas distribution with ^{13}CO (J=1-0) line, suggesting that the ionization front generated by the nearby star cluster drives shocks into the molecular clumps.

2. OBSERVATIONS AND DATA REDUCTION

We made one-dimensional raster scan observations of the S171 region with the Long-Wavelength Spectrometer (LWS; Clegg et al. 1996), the Short-Wavelength Spectrometer (SWS; de Graauw et al. 1996) and PHT Spectrometer (PHT-S; Lemke et al. 1996) on board ISO. The scan started from the position near Be 59 to the region ~ 5 pc from Be 59, which went through the ionized and neutral regions (Fig. 1). The observations were carried out at 24 positions, each of which was separated by $50''$. In this paper we discuss the results of [OI], [NII], and [SiII] lines detected with LWS and SWS. For the LWS observations the full grating scan mode AOT LWS01 was used to cover the wavelength range from 43 to 197 μm with $\lambda/\Delta\lambda \sim 100$–$200$ (Gry et al. 2002). The Off-Line Processing (OLP) version 10.1 data obtained from the ISO Archival Data Center were used. The spectra were further processed by using ISO Spectral Analysis Package (ISAP[1]). The line intensities were obtained by the Gaussian fit routine. The absolute flux calibration uncertainty for extended sources is reported to be 50% (Gry et al. 2002).

For the SWS observations the grating line profile mode AOT SWS02 was used to observe [SiII] 35 μm and H_2 S(3) lines. The OLP 10.1 data were obtained from the ISO Archival Data Center and used in the present study except for the data at the position 4.5 pc from Be 59, for which only the processed data of version 9.1 were available because of the software problem. We used ISAP for further processing and obtained the line intensities by the Gaussian fit routine. The flux calibration accuracy is reported to be 22% for the [SiII] 35 μm line for point-like sources, and the conversion factor for extended sources is estimated to be accurate within 10% (Leech et al. 2002).

3. RESULTS AND DISCUSSION

We detected 7 forbidden lines with LWS, and 2 lines with SWS at almost all the observed 24 positions. The spatial variations of some of the lines are shown in Fig. 2. In the following, we fo-

[1] The ISO Spectral Analysis Package (ISAP) is a joint development by the LWS and SWS Instrument Teams and Data Centers. Contributing institutes are CESR, IAS, IPAC, MPE, RAL and SRON.

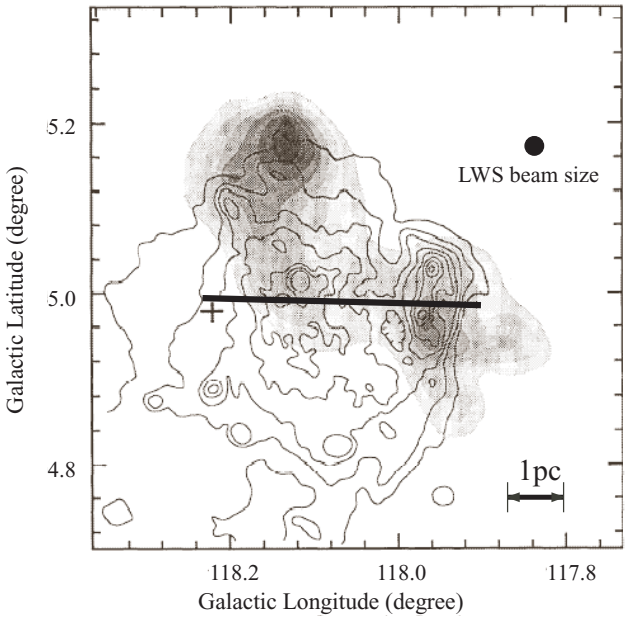

Figure 1. Gray-scale map of ^{13}CO (J=1-0) integrated intensity as well as the 0.61 GHz radio continuum emission in contours (Yang & Fukui 1992). The position of Be 59 is shown by +. The thick solid line indicates the line along which the present observations were carried out.

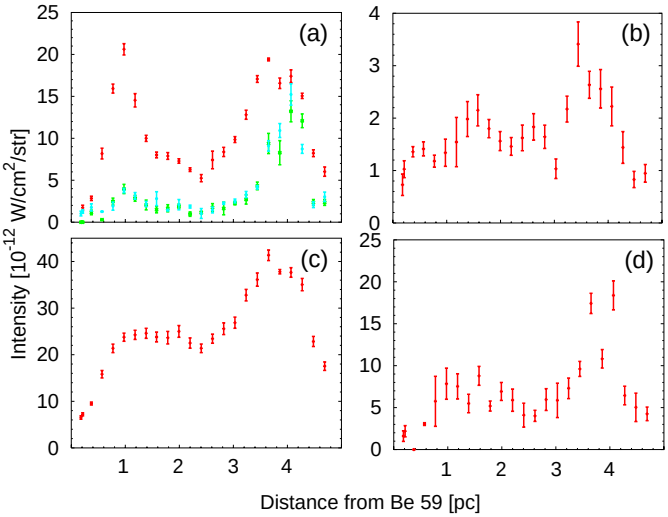

Figure 2. Observed line intensities plotted against the distance from Be 59. **a)** *[O I] 63 μm (red line) and 146 μm(×3) by LW3 (blue line) and by LW4 (green line).* **b)** *[N II] 122 μm.* **c)** *[C II] 158 μm.* **d)** *[Si II] 35 μm.*

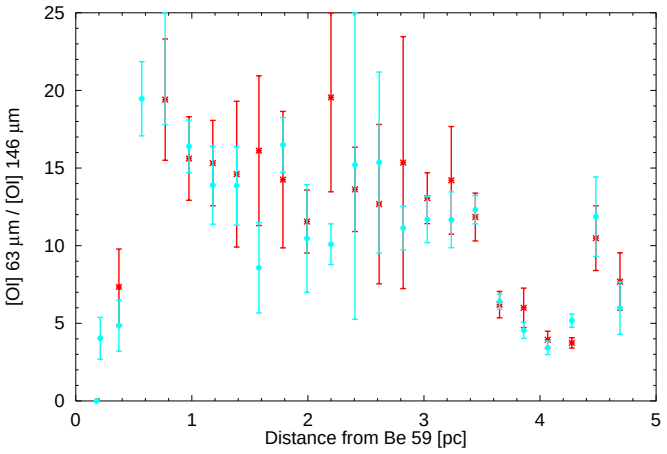

Figure 3. Observed [OI] 63 μm to 146 μm ratio with the 146 μm intensity detected by LW3 (red line) and LW4 (blue line) channels plotted against the distance from Be 59.

cus on two topics, the [OI] 63 μm to 146 μm ratio and the abundance of silicon in the gas phase derived from the line intensities of [OI] 63 μm, 146 μm, [NII] 122 μm, and [SiII] 35 μm. For the full discussion of all the observed lines, refer to Okada et al. (2002).

3.1. The [OI] 63 μm to 146 μm ratio

[OI] 63 μm and 146 μm lines come from neutral oxygen and the ratio is independent of the elemental abundance. The observed ratio ranges 5–20 (Fig. 3) and is particularly low (~ 5) around $d \sim 4$ pc, where d is the distance from Be 59.

The observed line and continuum intensities from the neutral gas are well interpreted by the PDR model of Kaufman et al. (1999), which takes account of the optical depth effect of [OI] 63 μm line (Okada et al. 2002). However, this model predicts the [OI] 63 μm to 146 μm ratio to be 13–20, which is not compatible with the lowest observed ratio of 5.

The PDR model of a one-dimensional semi-infinite slab assumes that the IR line photons escape only from the front surface of the slab. If we observe from the back of the slab, the atoms in the cool cloud between the [OI] lines emitting source and us absorb and weaken only the 63 μm line emission. If the optical depth of the [OI] 63 μm line in the cool cloud τ_{63} is 1.3, the observed ratio becomes 5 when the original ratio is 18 (the ratio expected from the PDR model). τ_{63} becomes 1.3 if only 3% of all oxygen atoms suggested by the ^{12}CO intensity is in the atomic form in the foreground cool cloud. Assuming that C/O ratio is the solar abundance and that all carbon is in CO, the remaining fraction of O atom is about 30%. Recent observations of the [OI] 63 μm absorption line towards massive star forming regions (Poglitsch et al. 1996; Baluteau et al. 1997) and the emission line towards the molecular cloud (Caux et al. 1999) have suggested that most of oxygen is in the atomic form. The [OI] 63 μm to 146 μm ratio is quite low (~ 5) at $d \sim 4$ pc, where ^{12}CO line intensity is the strongest. It is thus quite likely that part of the molecular gas is located between the [OI] 63 μm emitting region and us, and attenuates the line emission. Therefore we conclude that the absorption in the foreground cloud is the most likely cause for the observed low ratio of [OI] 63 μm to 146 μm ratio.

Small values compared to the PDR model prediction have been reported for the [OI] 63 μm to 146 μm ratio also in other objects. Liseau et al. (1999) showed that the ratio becomes $\sim$

1–5 in the ρ Oph cloud. Giannini et al. (2000) reported that NGC 2024 (Orion B, W12) has the [OI] 63 μm to 146 μm ratio of about 5 and suggested that the [OI] 63 μm line is strongly absorbed by the cold foreground gas. [OI] 63 μm in absorption has been directly observed (Poglitsch et al. 1996; Baluteau et al. 1997; Kraemer et al. 1998).

3.2. The abundance of gas phase silicon

We estimate the gas phase silicon abundance from the observed [NII] 122 μm and [SiII] 35 μm line intensities. The N abundance is assumed to be solar with no depletion and the singly ionized ion fraction is assumed to be the same for N and Si. Both lines are also assumed to originate from the same ionized region. Fig. 4 shows the observed intensities and the results of the calculation. The silicon depletion factor is large compared with carbon and oxygen, and the gas phase abundance is about 5% of solar in the cool clouds (Savage & Sembach 1996). The depleted atoms are thought to reside in interstellar grains. S171 shows the strong silicon emission, which requires log(Si/H)$= -5.06$, 25% of solar abundance silicon in the gas phase.

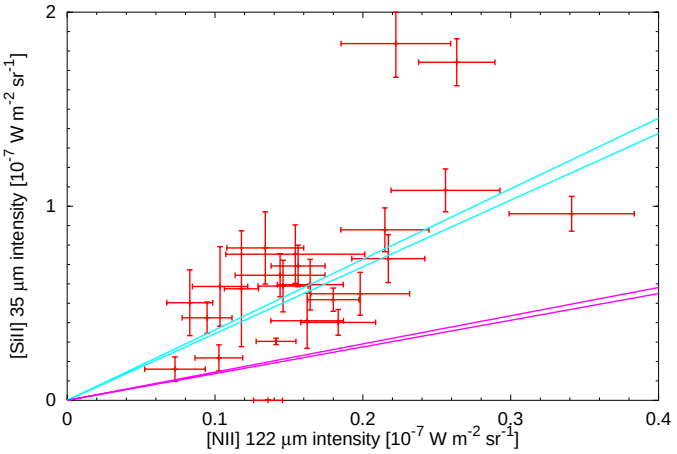

Figure 4. Observed [NII] 122 μm intensity vs. [SiII] 35 μm intensity. Blue lines indicate the calculation with Si abundance of 25% of solar abundance, and upper and lower lines are for $n_e = 50$ cm^{-3} and the low density limit, respectively. Pink lines show the results with Si abundance of 10% of solar abundance, and upper and lower lines are for $n_e = 50$ cm^{-3} and the low density limit. The electron temperature is assumed to be $T_e = 10^4$ K for all cases.

Intense [SiII] emission has been reported in several HII regions (Haas et al. 1991), in the Galactic center region (Stolovy et al. 1995), and in the Carina region (Mizutani et al. 2000). Silicon and carbon are major constituents of interstellar grains (Mathis 1990). The suggested large abundance of gaseous silicon in PDRs or HII regions indicates the efficient grain destruction processes in these regions (cf. Carral et al. 1994). Fitzpatrick (1996, 1997) have indicated that Si returns to the gas phase relatively quickly, while Fe grains seem to be more resistant. The present observations support these observations and indicate that Si in dust grains is relatively easily returned to the gas phase. This is in contrast to the constant gas abundance suggested for oxygen and carbon (Cardelli et al. 1996; Sofia et al. 1997; Cartledge et al. 2001). The recycling as well as the composition of dust grains in interstellar space should be reexamined based on these recent results of the gas abundance in various phases (cf. Tielens 1998; Jones 2000; Onaka 2000).

4. SUMMARY

Based on the mid- to far-infrared observation of S171 with ISO, we derived the following conclusions.

In the molecular region, [OI] 146 μm emission is very strong, and the [OI] 63 μm to 146 μm ratio is too small (~ 5) to be accounted for by PDR models. We conclude that the absorption by oxygen atoms in the foreground cool cloud is the most likely cause. The present results suggest that the interpretation of [OI] 63 μm intensity needs careful examination. [OI] 146 μm should not have this kind of problem, but it is much weaker.

For the lowly-ionized gas, [SiII] 35 μm is found to be quite strong and the observed [SiII] 35 μm to [NII] 122 μm ratio indicates the silicon abundance in the diffuse ionized gas to be about 25% of solar. This value is larger than the typical value of interstellar diffuse clouds ($\sim$ 5% of solar), suggesting the dust destruction occurring in the ionized region. [SiII] 35 μm can be as strong as [CII] 158 μm (Fig. 2), suggesting that it plays a significant role in the cooling for the diffuse ionised gas and that further observations in various ISMs should be interesting in the study of dust processing.

ACKNOWLEDGEMENTS

This work is based on observations with ISO, an ESA project with instruments funded by ESA Member States (especially the PI countries: France, Germany, the Netherlands and the UK) and with the participation of ISAS and NASA. The authors thank all the members of the Japanese ISO group, particularly H. Okuda, K. Kawara, and Y. Satoh for their help during the observations and continous encouragement. This work was supported in part by Grant-in-Aids for Scientific Research from the Japan Society for the Promotion of Science (JSPS).

REFERENCES

Baluteau , J. P., Cox, P., Cernicharo, J., et al. 1997, A&A, 322, L33
Cardelli, J. A., Meyer, D. M., Jura, M., & Savage, B. D. 1996, ApJ, 467, 334
Carral, P., Hollenbach, D. J., Lord, S. D., et al. 1994, ApJ, 423, 223
Cartledge, S. I. B., Meyer, D. M., Lauroesch, J. T., & Sofia, U. J. 2001, ApJ, 562, 394
Caux, E., Ceccarelli, C., Castets, A., et al. 1999, A&A, 347, L1
Clegg, P. E., Ade, P. A. R., Armand, C., et al. 1996, A&A, 315, L38
de Graauw, T., Haser, L. N., Beintema, D. A., et al. 1996, A&A, 315, L49
Fitzpatrick, E. L. 1996, ApJ, 473, L55
Fitzpatrick, E. L. 1997, ApJ, 482, L199
Giannini, T., Nisini, B., Lorenzetti, D., et al. 2000, A&A, 358, 310
Gry, C., Swinyard, B., Harwood, A., et al. 2002, The ISO Handbook, vol. IV: LWS - The Long Wavelength Spectrometer, Version 2.0

Haas, M. R., Hollenbach, D. J., & Erickson, E. F. 1991, ApJ, 374, 555
Hollenbach, D. J., & Tielens, A. G. G. M. 1997, ARA&A, 35, 179
Jones, A. P. 2000, JGR, 105, 10257
Kaufman, M. J., Wolfire, M. G, Hollenbach, D. J., & Luhman, M. L. 1999, ApJ, 527, 795
Kessler, M. F., Steinz, J. A., Anderegg, M. E., et al. 1996, A&A, 315, L27
Kraemer, K. E., Jackson, J. M., & Lane, A. P. 1998, ApJ, 503, 785
Leech, K., de Graauw, T., van den Ancker, M., et al. 2002, The ISO Handbook, vol. VI: SWS - The Short Wavelength Spectrometer, Version 2.0
Lemke, D., Klaas, U., Abolins, J., et al. 1996, A&A, 315, L64
Liseau, R., White, G. J., Larsson, B., et al. 1999, A&A, 344, 342
Mathis, J. S. 1990, ARA&A, 28, 37
Mizutani, M., Onaka, T., & Shibai, H. 2000, ESA-SP, 456, 115
Okada, Y., Onaka, T., Shibai, H., & Doi Y., 2002, in preparation
Onaka, T. 2000, ISAS Report SP-14, 83
Poglitsch, A., Herrmann, F., Genzel, R., et al. 1996, ApJ, 462, L43
Savage, B. D., & Sembach, K. R. 1996, ARA&A, 34, 279
Sofia, U. J., Cardelli, J. A., Guerin, K. P., & Meyer, D. M. 1997, ApJ, 482, L105
Stolovy, S. R., Herter, T., Gull, G. E., Pirger, B., & Vogt, N. P. 1995, in ASP Conf. Vol 73, Airborn Astronomy Symposium on the Galactic Exosystem: From Gas to Stars to Dust, ed. Haas, M., R., Davidson, J. A., & Erickson, E. F., p.469
Tielens, A. G. G. M. 1998, ApJ, 499, 267
Yang, J., & Fukui, Y. 1992, ApJ, 386, 618

AN INFRARED STUDY WITH ISOCAM OF CHAMAELEON II AND III DARK CLOUDS

Paolo Persi[1], **Anna Rosa Marenzi**[1], **and Mercedes Goméz**[2]

[1]Istituto Astrofisica Spaziale e Fisica Cosmica CNR, Via fosso del Cavaliere, 100, 00145 Roma, Italy
[2]Observatorio Astronómico de Córdoba, Laprida 854, 5000 Córdoba, Argentina

ABSTRACT

We present the results of an infrared study including ISOCAM images at 6.75 and 14.3 μm and near-IR DENIS images of large portions of the dark clouds Chamaeleon II ($28' \times 26'$) and Chamaeleon III ($19' \times 18'$). We have found 12 young stellar objects (YSOs) in Cha II, of which 8 are previously identified sources. ISO-ChaII28 identified with IRAS 1255-7651 and located at the center of the cloud is a Class I YSO with an infrared luminosity of $\sim$ 1.5L$\odot$. The new candidate YSO in Cha II, ISO-ChaII13 has a clear mid–IR excess with an infrared luminosity of $\sim$0.02L$\odot$ indicating the probable presence of a young brown dwarf. Finally, no sources with IR excess has been detected in Cha III at our sensitivity limits.

Key words: stars: formation – stars: low-mass, brown dwarfs – stars: pre-main sequence – infrared: stars

1. INTRODUCTION

The Chamaeleon dark-cloud complex is a nearby (D$\approx$140–180 pc) and high galactic latitude (b$\sim$-16°) low-mass star forming region. The complex include three major clouds (Cha I, II and III) probably at a different evolutionary stage as suggested by Prusti et al. (1992) and by the recent X-ray ROSAT pointed observations reported by Alcalá et al. (2000). Of the three main clouds, Cha I has been the most thoroughly studied and contains a great variety of YSOs; from reflection nebulae, to Herbig-Haro objects and a bipolar outflow located in the north part of the region (Mattila et al. 1989; Persi et al. 1999). Star formation is also evident in Cha II cloud as shows the presence of several pre-main-sequence (PMS) stars with H_α emission found by Schwartz (1977) and Hartigan (1993). IRAS data and near-IR photometry allowed Whittet et al. (1991), Prusti et al. (1992) and Larson et al. (1998) to classify most of these objects as classical T Tauri stars. On the other hand, there are no YSOs associated with Cha III.

As part of the ISOCAM (Cesarsky et al. 1996) central program of nearby star forming regions, the three dark clouds were surveyed in the two broad filters LW2 (λ_{eff}=6.75 μm) and LW3 (λ_{eff}=14.3 μm) for a total area of 0.93 sq.deg. The preliminary results of this survey are reported by Nordh et al. (1996), while a detailed analysis of the ISOCAM observations of Cha I is given in Persi et al. (2000).

In this paper, we discuss the results of an infrared study of the Chamaeleon II and III dark clouds based on ground-based near–IR observations obtained with DENIS (Epchtein et al. 1997) and high sensitivity mid-IR images taken with ISOCAM in order to extend the study of the young stellar population within these two clouds.

2. OBSERVATIONS

We have re-processed the ISOCAM raw data taken from the ISO Data Archive of the dark clouds Cha II and III (TDT N.11500619, N.11500620, N.07900117, N.07900118), using the new version of the Cam Interactive Analysis (CIA v5.0) software. The ISOCAM observations were taken in raster mode at LW2(5–8.5 μm) and LW3(12–18 μm). All the frames were observed with a pixel field of view (PFOV) of 6″, intrinsic integration time T_{int}= 2.1 sec and $\sim$15 sec integration time per sky position. We have applied the same procedure as described by Persi et al. (2000) to reduce the images and to obtain the photometry of the detected sources.

Table 1. ISOCAM observations of Cha II and Cha III.

Cloud	$\alpha(2000)$	$\delta(2000)$	Filter	Area	T_{tot}
	h m s	° ′ ″			sec.
Cha II	13 00 47	-77 06 09	LW2	$28' \times 26'$	4472
Cha II	13 00 47	-77 06 09	LW3	$28' \times 26'$	4474
Cha III	12 52 53	-79 38 18	LW2	$19' \times 18'$	2906
Cha III	12 52 53	-79 38 18	LW3	$19' \times 18'$	2909

Table 1 gives the characteristics of the ISOCAM survey of the two clouds including the central position and the area of the observed fields. The last column reports the total integration time per filter. The detection limits for this survey are about 0.8 mJy (1σ) for LW2 and 1.3 mJy (1σ) for LW3.

The DENIS images in the J and Ks filters were provided by Cambrésy (private communication). From a positional comparison between the DENIS and our sources, we have derived a mean astrometric accuracy of about $\pm$ 4–5″in both coordinates for the objects detected by ISOCAM.

Proceedings of the Symposium *"Exploiting the ISO Data Archive - Infrared Astronomy in the Internet Age"*, 24–27 June 2002, Sigüenza, Spain (C. Gry, S. B. Peschke, J. Matagne et al. eds., ESA SP-511)

3. CHAMAELEON II

Fig. 1 shows the ISOCAM images at 6.75 and 14.3 μm of Cha II compared with the optical image taken from the Digital Sky Survey (DSS) plates. We have detected 115 sources at 6.75 μm and 35 sources at 14.3 μm with S/N ratio ≥ 3.

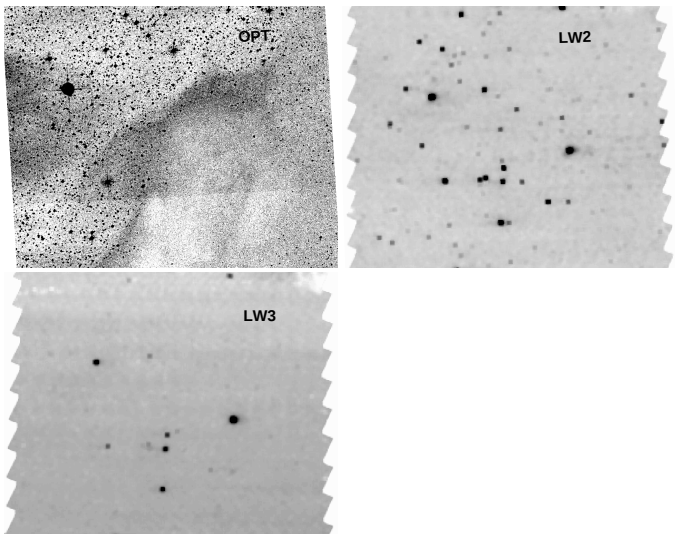

Figure 1. Optical and ISOCAM images at 6.75 and 14.3 μm of Cha II.

Approximately 70% of the sources found at 6.75 μm have been identified with visible stars and have been detected in the near-IR by the DENIS survey. In addition all the previously known members of the cloud lying in our survey region have been detected by ISOCAM. The bright source nearly at the center of the region (ISO-ChaII28) has been identified with the Class I YSO IRAS 1255-7651 which luminosity is $\sim$ 1.5 L$\odot$. To discriminate young objects from field stars, we have used the color-magnitude diagram ($m_{14.3}$ vs. $m_{6.7} - m_{14.3}$)(Fig.2) and the color-color plot ($J - K_s$ vs. $K_s - m_{6.7}$)(Fig.3) for sources detected only at 6.75 μm. Sources with $m_{6.7} - m_{14.3}$ $\sim$ 0 are field stars (open squares) or Class III objects (open circles) for which the mid-IR emission is mainly due to the stellar photosphere. Six objects in Fig.2 show clear mid-IR excess that indicates the presence of circumstellar material. Of these six sources, five were previously identified as PMS stars (filled circles) in Cha II, while one very faint source (ISO-ChaII13) is a new detection (filled square). Its integrated luminosity from 1 to 14.3 μm is $\sim$ 0.02 L$\odot$, assuming a distance of 178 pc. This luminosity corresponds to a young brown dwarf with an age between 1 and 10 Myr.

In addition at least four more sources observed only at LW2 (crosses in Fig.3) and not previously identified are located at the right of the reddening band, showing a clear IR excess (Fig.3). These objects may be new candidate YSOs of Cha II.

Combining the near and mid-IR observations, we have derived the spectral energy distribution (SED) of the YSOs previously identified (Fig.4). In addition, we have computed

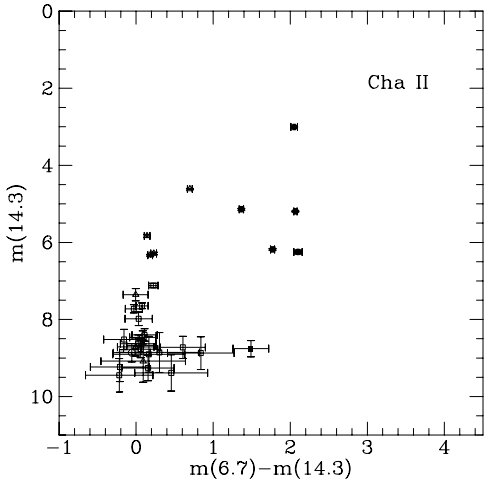

Figure 2. Color–magnitude plot for the ISOCAM sources in Cha II.

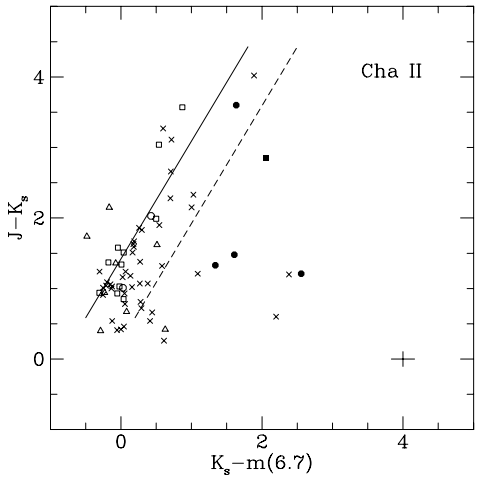

Figure 3. Color–color plot for the ISOCAM sources in Cha II.

the spectral index $\alpha_{2.2-14.3\mu m} = \mathrm{dlog}\lambda F_\lambda / \mathrm{dlog}\lambda$ for these sources, and we have derived their spectral energy distribution class reported in Fig.4. A detailed discussion of this cloud is given by Persi et al. (2002).

4. CHAMAELEON III

We have detected 35 sources at 6.75 μm and only 5 sources at 14.3 μm. All these sources have been identified with the DENIS near-IR sources. In Fig.5, we have compared the mid-IR images of Cha III with the optical image from the DSS plates.

From the analysis of the magnitude–color and color–color plots of Fig.6 obtained using the DENIS near-IR photometry and the mid-IR ISOCAM fluxes, we conclude that no sources with IR excess are present in Cha III. This could indicate that YSOs in Cha III are deeply embedded in the cloud. Our result is in agreement with the idea that Cha III is in an earliest evolu-

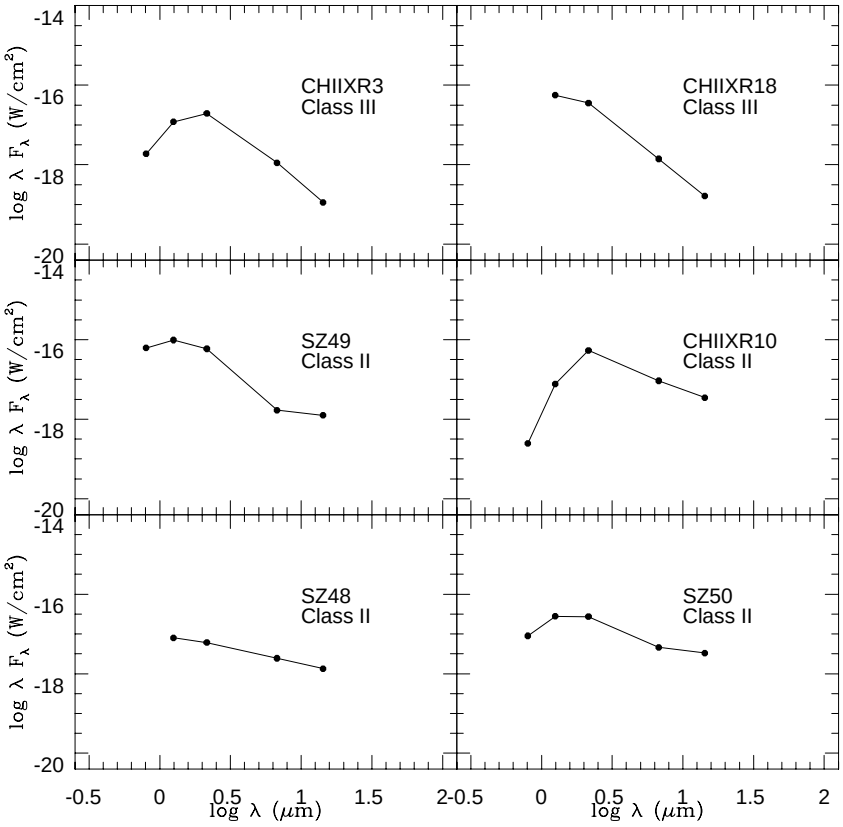

Figure 4. Spectral energy distribution of YSOs previously identified in Cha II.

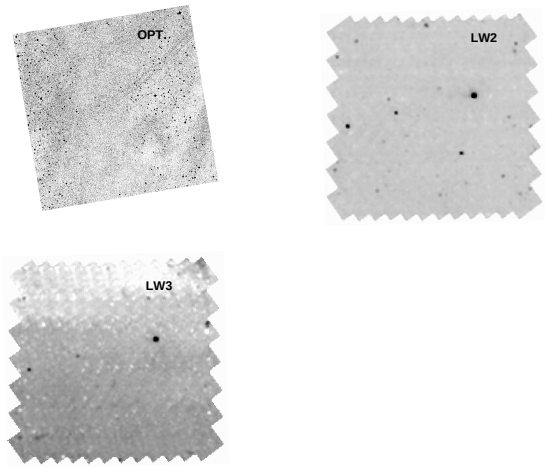

Figure 5. Optical and ISOCAM images at 6.75 and 14.3 μm of Cha III.

tionary phase than Cha I and Cha II, not observable from near and mid infrared.

5. CONCLUSIONS

From the analysis of the ISOCAM and DENIS near-IR observations of Cha II and Cha III dark clouds, the following conclusions can be derived:

1) We have detected in Cha II cloud a total of 115 point-like sources with S/N$\geq$3 at 6.75 μm of which 35 have been found also at 14.3 μm. A small number of these sources show a mid-IR excess and/or 2.2–6.75 μm excess emission. Most of these objects are previously known PMS stars of the cloud. We classified them using the observed infrared spectral index. Only one source (ISO-ChaII13) not previously identified shows a mid-IR excess, indicating a new member of the cloud. From its observed infrared luminosity of $\sim$ 0.02 L$\odot$, we propose ISO-ChaII13 as a candidate young brown dwarf.

2) No sources with IR excess has been observed in the core of Cha III. This suggests that the cloud is probably at an earliest evolutionary stage of the star forming complex.

ACKNOWLEDGEMENTS
We are grateful to L.Cambrésy for providing us with the DENIS data.

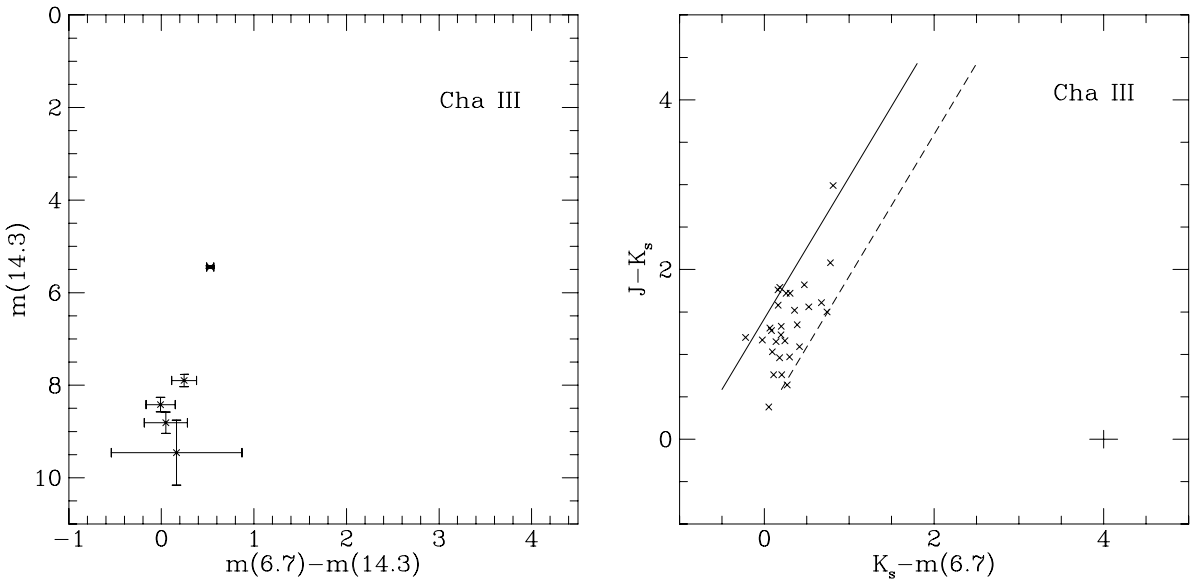

Figure 6. Color–magnitute (left panel), and color–color (right panel) plots for the ISOCAM sources in Cha III.

REFERENCES

Alcalá J.M., Covino, E., Sterzik, M.F., et al., 2000, A&A 355, 629
Cesarsky C.J., Abergel A., Agne'se P., et al. 1996, A&A 315, L32
Epchtein N., et al. 1997, The Messenger, 87, 27
Hartigan P. 1993, AJ 105, 1511
Larson K.A., Whittet D.C.B., Prusti T., Chiar J.E. 1998, A&A 337, 465
Mattila K., Liljeström T., Toriseva M., 1989, in Low Mass Star Formation and Pre-Main Sequence Objects, ed.Reipurth (Garching:ESO), 153
Nordh L., Olofsson G., Abergel A., et al. 1996, A&A 315, L185
Persi P., Marenzi A.R., Kaas A.A., et al., 1999, AJ 117, 445
Persi P., Marenzi A.R.,Olofsson G., et al. 2000, A&A 357, 219
Persi P., Marenzi A.R., Gómez M., Olofsson G., et al. 2002, A&A to be submitted
Prusti T., Whittet D.C,B., Assendorp R., Wesselius P.R. 1992, A&A 260, 151
Schwartz R.D. 1977, ApJS 35, 161
Whittet D.C.B., Assendorp R., Prusti T., et al. 1991, A&A 251, 524

[CII] 158 μM ABSORPTION LINE TOWARDS THE GALACTIC CENTER: CONNECTION WITH BRIGHT IR GALAXIES

Charlotte Vastel[1,4], Edward T. Polehampton[2], Jean-Paul Baluteau[3], Bruce M. Swinyard[2], Emmanuel Caux[4], and Pierre Cox[5]

[1]Caltech 320-47, Pasadena, CA 91125, USA
[2]RAL, Chilton, Didcot, Oxon, UK
[3]LAM, BP 8, F-13004, Marseille, France
[4]CESR, BP 4346, F-31028, Toulouse Cedex 04, France
[5]IAS, F-91405, Orsay Cedex, France

ABSTRACT

Located near the galactic center, Sgr B2 is one of the largest HII/molecular cloud complexes in the Galaxy. The total mass and compactness of Sgr B2 are comparable to those of the W49N star-forming complex (Vastel et al. 2000, Vastel et al. 2001). We present high spectral resolution Fabry-Pérot observations of the [OI] 63.2 and 145.5 μm and [CII] 157.7 μm fine structure lines obtained with ISO-LWS. Observations of the CO isotopes and the HI lines reveal that three different layers containing atomic oxygen can be disentangled as predicted by PDRs models. These layers are characterized by different forms of carbon in the gas phase, i.e. the C^+ external layer, the C^+ to C^0 transition and the CO internal layer. We derive lower limits for the column densities of atomic carbon and oxygen of the order of $\sim 10^{18}$ cm^{-2} and 3×10^{19} cm^{-2}, respectively. An O^0/CO ratio of around 2.5 is computed in the internal cores of the clouds lying along the line of sight, which means that $\sim$ 70% of gaseous oxygen is in the atomic form and not locked into CO. The fact that the [CII] 157.7 μm line is detected in absorption implies that the main cooling line of the interstellar medium can be optically thick especially in the direction of large star-forming complexes or in the nuclei of galaxies. This could partially account for the deficiency in the [CII] 157.7 μm line which has been recently found toward infrared bright galaxies in ISO data.

Key words: ISM, abundances, clouds, infrared, radio lines

1. ISO-LWS OBSERVATIONS

The [OI] 63.2 μm and 145.5 μm and [CII] 157.7 μm lines have been observed toward Sgr B2 with the LWS instrument using the high resolution mode (L03 prime and non prime, and L04 prime). All these observations are presented in details in Vastel et al. (2002). Figure 1 shows the spectrum at 63 μm using L03 prime, L03 non prime and L04 prime observations. In the following we will use the spectrum obtained in the L03 non-prime mode whose systematic and random noise at line center is the lowest.

Due to the large number of velocity components toward Sgr B2, the determination of the location of individual absorbing clouds remains difficult. We adopted the Greaves and Williams (1994) schematic diagram (see Figure 2), except for the 0 km s^{-1} component which could be a blending of all the components along the line of sight.

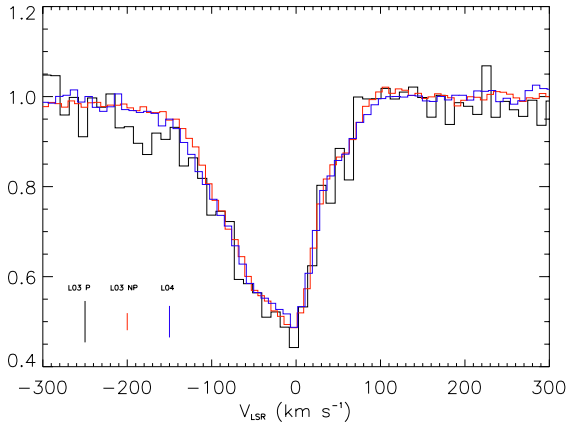

Figure 1. Comparison between the L03 prime (black), L03 non prime (red) and L04 prime data (blue) with their combined systematic and random error at line center. The Y-axis is the line to continuum ratio.

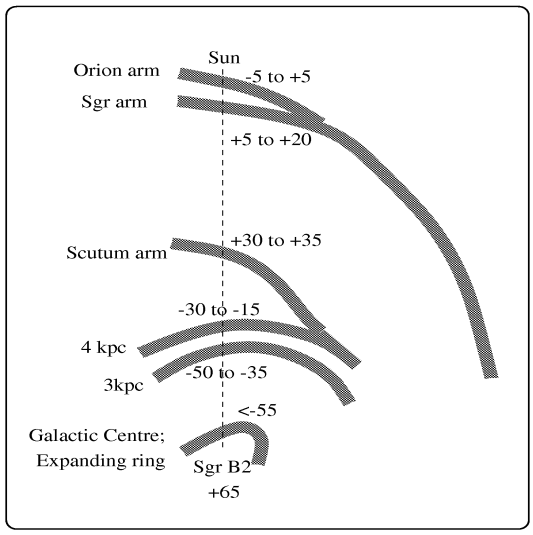

Figure 2. Proposed locations of the foreground clouds with their associated V_{LSR} in km s^{-1}. Not to scale.

Proceedings of the Symposium *"Exploiting the ISO Data Archive - Infrared Astronomy in the Internet Age"*, 24–27 June 2002, Sigüenza, Spain (C. Gry, S. B. Peschke, J. Matagne et al. eds., ESA SP-511)

2. MODELLING

At velocities below 30 km s^{-1}, the [CII] 157.7 μm line is seen in absorption and in emission at larger velocities (see Figure 3). The C^+ absorption features are fitted by Gaussians whose centers and line widths are deduced from the HI 21 cm line parameters (Garwood & Dickey 1989). The optical depth of each absorption features is adjusted in order to reproduce the observed spectrum when combined with the emission at 60 km s^{-1} parameterized by the [OI] 145.5 μm line seen in emission. The final fit is shown in Figure 3 after convolution with the instrumental profile.

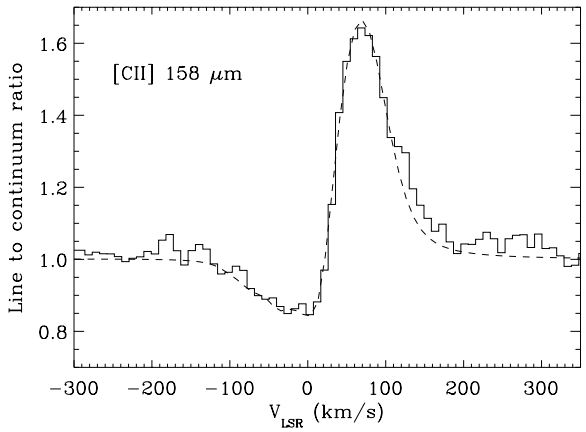

Figure 3. The C^+ line compared to a model profile after convolution with the instrumental profile (dashed line).

Molecular observations of Sgr B2 have been carried out in the ^{13}CO and C^{18}O (1-0) and (2-1) lines at the IRAM-30 meters telescope. The Sgr B2 complex was mapped over the 80″ LWS beam area with a beam size of 21″ at 2.6 mm and 11″ at 1.3 mm. The spectra show a bright emission profile at the velocity of the HII region around 60 km s^{-1}. Many molecular components appear at velocities between -120 km s^{-1} and 35 km s^{-1} in absorption in the central part of the map over a 30″ × 30″ area, and in emission around. The clouds mapped in the LWS beam seem to be homogeneous and uniform as the emission components also have their counterparts in the absorption components. We averaged the spectra surrounding the 30″ × 30″ area and replaced the central spectra by this average. We then convolved the resulting spectra with a gaussian weighting function to degrade the spatial resolution to 80″ (ISO/LWS beam). The constructed spectra are shown in Figure 4. From these ^{13}CO and C^{18}O observations, we derived the physical parameters of eight molecular cloud cores with $V_{LSR} \leq 10$ km s^{-1}, using a standard LVG model.

We combined these molecular observation to HI 21 cm observations (Garwood & Dickey 1989) to disentangle to clouds along the line of sight. **Three different layers can be distinguished according to Photo-Dissociation Regions (PDR) models.** Ionized carbon, atomic hydrogen and atomic oxygen coexist in the warm, mostly neutral, layer that lies at the surface on which the UV impinges. In the next (deeper) layer, where molecular hydrogen is able to resist photo-dissociation, ionized carbon and atomic carbon still coexist. The third layer, which constitutes the cold self-shielded molecular core of the cloud, contains molecular hydrogen, carbon monoxide and atomic oxygen. We present in Table 1 the 8 clouds, where the external layers have been traced by HI and the molecular cores by ^{13}CO and C^{18}O.

Table 1. Compared properties of the eight clouds found between -110 and +10 km s^{-1}.

Cloud label	External layers V_{LSR} (km/s)	Molecular clouds V_{LSR} (km/s)	Galactocentric distance (kpc)
A	-108	-113.6 & -104.8	< 1
B	-92		< 1
C	-77	-76	< 1
D	-60.5	-57.8	< 1
E	-51.9		3
F	-44	-46.2 & -41	3
G	-21.5	-25.8 & -20.5	4
H	-3.5 & 5.5	1.7	?

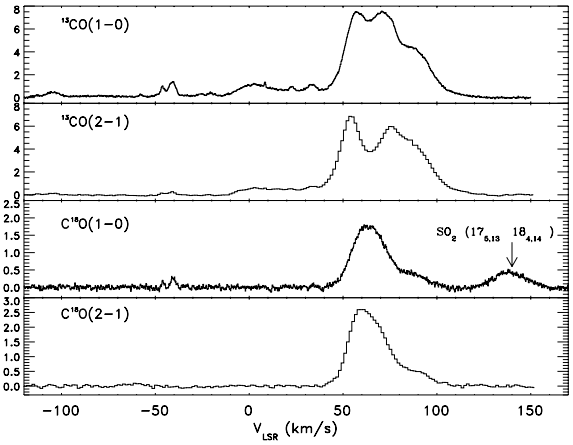

Figure 4. ^{13}CO and C^{18}O (1 - 0) and (2 - 1) line spectra degraded to the 80″ ISO-LWS beam (see text). The y-axis is in main beam temperature.

With the same modelling already used for W49N (Vastel et al. 2000), we combined the absorption due to the diffuse layers traced by atomic hydrogen to the absorption due to molecular layers traced by CO and its isotopes for each of the clouds along the line of sight to Sgr B2. The final fit is presented in Figure 5.

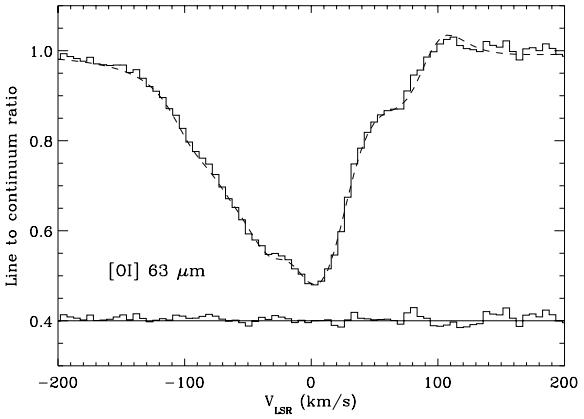

Figure 5. Observed [OI] 63.2 μm absorption profile toward Sgr B2 together with the best fit (dashed line) including both the external layers and the molecular cores contributions. The lower plot shows the residuals, Y-shifted by +0.4 for clarity.

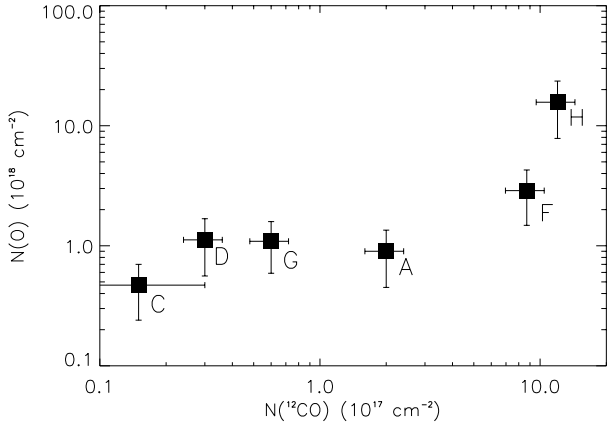

Figure 6. The O^0 column density against the CO column density for the clouds associated with molecular clouds. Cloud labels identify each data point. Note that this is a logarithmic scale: the fit was carried out on a linear scale.

3. Results

3.1. The O^0/CO ratio in the molecular cores

The O^0/CO ratio in the molecular clouds varies between 3 and 37 with a mean value of 18. The O^0 column densities of the 6 clouds exhibiting molecular cores (A, C, D, F, G, H) are plotted versus their CO column densities in Figure 6. There is a clear correlation between N(O) and N(CO), except for cloud H (at 1.7 km s^{-1}) which is believed to result from a blending of clouds with uncertain galactocentric distances. We performed a linear least-square fit and found that the resulting slope is 2.5 $\pm$ 1.8 and the intersection point with the N(O)-axis gives an excess amount of atomic oxygen with an average column density of (5.6 $\pm$ 2.0) $\times$ 10^{17} cm^{-2}. **This atomic oxygen in excess is interpreted as due to an intermediate layer between the C^+ external layer and the CO core where the atomic oxygen coexist with the atomic carbon, as predicted by PDR models.** Our derived O^0/CO ratio implies that $\sim$ 70% of gaseous oxygen is in the atomic form and not locked into CO in the molecular clouds along the Sgr B2 line of sight. The upper (respectively lower) limits of this ratio corresponds to $\sim$ 80% (respectively 40%) of the gaseous oxygen in the atomic form. Considering the calculated uncertainties, we cannot directly determine the exact oxygen budget in these molecular clouds. However, only the lower limit on the O^0/CO ratio is consistent with the prediction of steady states models and though we cannot exclude values as low as this (O^0/CO $\sim$ 1), the probability of larger ratios is much higher. The oxygen chemistry in dense clouds is still not well known as it is very difficult to reproduce the O_2 and H_2O abundances limits measured by **SWAS**. Further observations of the O^0, O_2 and H_2O species will provide important clues to constrain the chemistry in these cold molecular clouds.

3.2. The C^0 layer in the clouds

Using the cosmic O/C ratio of 2.3, we deduce an average N(C) in each cloud along the line of sight of (2.4 $\pm$ 0.9) $\times$ 10^{17} cm^{-2}. This value is well within the range of values derived by Usuda et al. (*in preparation*) from C^0 observations. Their first detection of the [CI] $^3P_1$ - $^3P_0$ absorption lines in the direction of Sgr B2 in the 10.6″ beam of JCMT leads to an estimate of the C^0 column density in five cloud complexes (clouds labelled here A, C, D, F and G) between 1 and 13 $\times$ 10^{17} cm^{-2}.

A summary of previous measurements of the C^0/CO ratio in galactic interstellar clouds is illustrated in Figure 9 of Usuda et al. (*in preparation*) where this ratio is plotted against the cloud visual extinction. The highest values of this ratio (between 2 and 20) are obtained in diffuse interstellar clouds while the lowest values (ranging from 0.03 to 0.3) are found in dense photo-dissociation regions. The general slope of the C^0/CO vs A_V relation indicates that the column density of C^0 is relatively constant in clouds with visual extinction greater than unity. Our derived values of the C^0/CO ratio are consistent with this general relation; clouds C and D could be classified as diffuse clouds where C^0/CO = [16.2, 8.1], clouds A and G as translucent clouds where C^0/CO = [1.2, 4.0] and cloud F as a dense cloud where C^0/CO = 0.3.

Values for the C^+/C^0 ratio in the six clouds associated with a molecular core can be derived from this study. While clouds close to the galactic center (labelled A, C and D) yield a C^+/C^0 ratio less than 0.7, those at the galactocentric distance of 3-4 kpc (F and G) have ratios close to 2.5. For $G_0/n \leq 3 \times 10^{-3}$ cm^3, the C^+/C/CO transition is drawn to the cloud surface (Kaufman et al. 1999) which could explain the low C^+/C^0 ratio (< 1) found near the galactic center.

3.3. Optical thickness of the C^+ line

The [CII] fine structure transition at 157.741 μm is the major coolant of the warm interstellar medium. Carbon is the fourth most abundant element and has a lower ionization potential (11.26 eV) than hydrogen. Therefore, carbon is in the form of C^+ on the surface of far UV illuminated neutral gas clouds. In addition, the C^+ line is relatively easy to excite, so that the line can efficiently cool the warm neutral gas. Depending on the density in this layer, the line may be self-absorbed. The first observational evidence of an absorption feature in the C^+ spectrum has been carried out by the Kuiper Astronomical Observatory toward the W51 HII region (Zmuidzinas, 1987). The absorption feature in its profile was attributed to a separate "cooler" low density foreground cloud. Recently, studies of many bright galaxies showed that **the [CII] 157.7 μm line is deficient compared to the total FIR luminosity**. Non detection or weak detection have been highlighted toward FIR bright galaxies (Malhotra et al. 1997; Luhman et al. 1998). These observations were carried out at a much lower resolution than that used in our study of Sgr B2. Our results indicate that if these galaxies were viewed at high spectral resolution, the spectra could reveal both emission and absorption components present in the C^+ profile. This strengthens the idea that under certain conditions **the C^+ line could be optically thick in the direction of large star-forming complexes or in the nuclei of galaxies**.

4. Conclusion

Using [CII] 157.7 μm, [OI] 63.2 and 145.5 μm line observations, we were able to distinguish between the contributions of the different layers within the galactic clouds along the line of sight to Sgr B2. We separate the layers of the atomic diffuse surface and of the molecular core of these clouds. We were able to associate atomic oxygen with three layers through the clouds characterized by different forms of carbon in the gas phase, as predicted by standard PDR models: i.e. the major form of carbon changing from C^+ to C^0 and finally to CO.

From the line shape modelling presented here, a total column density of atomic oxygen in the line of sight to Sgr B2 of about 3.1×10^{19} cm^{-2} is derived within the clouds with velocities between -120 km s^{-1} and +10 km s^{-1}. Less than 30% of this total O^0 column density is found to be due to the external layers of the clouds (where C^+ is the major form of carbon).

The method used in this study leads to an estimate of the oxygen content in the intermediate layer where C^0 is the dominant form of carbon. The atomic carbon column densities derived here for the galactic clouds, with a mean value about 2.4×10^{17} cm^{-2}, are in good agreement with recent observations of the [CI] 492 GHz line. The derived C^0/CO ratios are indicative of clouds, ranging from diffuse to dense, along the line of sight of the Sgr B2 complex which have been fragmented and illuminated by the galactic interstellar radiation field. C^+/C^0 ratios close to 2.5 are derived for the clouds at galactocentric distances of 3 - 4 kpc, and ratios less than 0.7 for clouds in the galactic center region.

The method used to disentangle the different layers of the clouds in the line of sight leads to the accurate computation of the O^0/CO ratio ($\sim$ 2.5) in the internal layers. Therefore, about 70% of gaseous oxygen is in the atomic form and not locked into CO in the molecular clouds along the Sgr B2 line of sight. Future instrumentation will enable the present analysis to be improved. The **Herschel** project, with its high spectral resolution (**HIFI**) capability, will allow to better characterize the physical conditions of these clouds along the line of sight to Sgr B2 (and maybe on other lines of sight in direction of the galactic center as well), in particular from the C^+ and C^0 lines and from high J transitions of CO. **SMA** and **ALMA** will provide high spatial resolution C^0 observations of these clouds necessary to separate each of them. **At high spectral resolution, the fundamental transitions of atomic oxygen will only be accessible to the second instrument generation on board the SOFIA observatory**.

REFERENCES

Garwood, R., & Dickey, J., 1989, ApJ 338, 841

Greaves, J.S. & Williams, P.G., 1994, A&A 290, 259

Kaufman, M., Wolfire, M., Hollenbach, D., Luhman, D., 1999, ApJ 527, 795

Luhman, M., Satyapal, S., Fischer, J., Wolfire, M., et al., 1998, ApJ 504, L11

Malhotra, S., Helou, G., Stacey, G., Hollenbach, D., et al., 1997, ApJ 491, L27

Usuda, K., Hasegawa, T. and White, G., *in preparation*

Vastel, C., Caux, Ceccarelli, C., et al., 2000, A&A 357, 994

Vastel, C., Spaans, M., Ceccarelli, C., Tielens, X., Caux, E., 2001, A&A 376, 1064

Vastel, C., Polehampton, E., Baluteau, J.P., et al., to be published in ApJ in december 2002

Zmuidzinas, J., 1987, PhD Thesis